

2005

MicroPIV measurement of turbulent and transitional flow characteristics in microchannels

Hao Li

Iowa State University

Follow this and additional works at: <https://lib.dr.iastate.edu/rtd>

 Part of the [Fluid Dynamics Commons](#), [Mechanical Engineering Commons](#), and the [Plasma and Beam Physics Commons](#)

Recommended Citation

Li, Hao, "MicroPIV measurement of turbulent and transitional flow characteristics in microchannels " (2005). *Retrospective Theses and Dissertations*. 1752.

<https://lib.dr.iastate.edu/rtd/1752>

This Dissertation is brought to you for free and open access by the Iowa State University Capstones, Theses and Dissertations at Iowa State University Digital Repository. It has been accepted for inclusion in Retrospective Theses and Dissertations by an authorized administrator of Iowa State University Digital Repository. For more information, please contact digirep@iastate.edu.

MicroPIV measurement of turbulent and transitional flow characteristics in
microchannels

by

Hao Li

A dissertation submitted to the graduate faculty
in partial fulfillment of the requirements for the degree of
DOCTOR OF PHILOSOPHY

Major: Mechanical Engineering

Program of Study Committee:
Michael G. Olsen, Major Professor
Francine Battaglia
Palaniappa Molian
Hui Hu
Michael Pate

Iowa State University

Ames, Iowa

2005

Copyright © Hao Li, 2005. All rights reserved.

UMI Number: 3200439

INFORMATION TO USERS

The quality of this reproduction is dependent upon the quality of the copy submitted. Broken or indistinct print, colored or poor quality illustrations and photographs, print bleed-through, substandard margins, and improper alignment can adversely affect reproduction.

In the unlikely event that the author did not send a complete manuscript and there are missing pages, these will be noted. Also, if unauthorized copyright material had to be removed, a note will indicate the deletion.

UMI[®]

UMI Microform 3200439

Copyright 2006 by ProQuest Information and Learning Company.

All rights reserved. This microform edition is protected against unauthorized copying under Title 17, United States Code.

ProQuest Information and Learning Company
300 North Zeeb Road
P.O. Box 1346
Ann Arbor, MI 48106-1346

Graduate College
Iowa State University

This is to certify that the doctoral dissertation of
Hao Li
has met the dissertation requirements of Iowa State University

Signature was redacted for privacy.

Committee Member

Signature was redacted for privacy.

Major Professor

Signature was redacted for privacy.

For the Major Program

DEDICATION

This dissertation is dedicated to four people who shared with me the risks and sacrifices required to complete it. The first two of these are my parents, Youwei Li and Xiaocai Gu, who made all of this possible with their endless encouragement and patience. The third is my wife, Hua Shao, who brought me a lovely daughter and who shared equally with me all the emotional and financial burdens involved. The fourth is my daughter, Tina Li, who seems to be growing into a wonderful human being, in spite of the fact that her father was less available than he should have been during the first year of her life.

TABLE OF CONTENTS

LIST OF TABLES	viii
LIST OF FIGURES	ix
ABSTRACT	xiii
CHAPTER 1 INTRODUCTION	1
Statement of General Purposes	1
Microfluidic Flow in Smooth Microchannels	1
Microfluidic Flow in Roughened Microchannels with Single Microstructure	4
Dissertation Contents and Contributions	5
CHAPTER 2 EXPERIMENTAL TECHNIQUE AND SETUP	8
Microchannel Fabrication	8
Mold Master	8
Casting PDMS	9
Microchannel Assembly	10
Resulting Device	10
Experimental Apparatus and Methodology	11
Experimental Setup and Method	11
Experimental Uncertainty	14
CHAPTER 3 MICROPIV MEASUREMENT OF TURBULENT FLOW IN SQUARE MICROCHANNELS WITH VARYING HYDRAULIC DIAMETERS	19

Abstract	19
Introduction	20
Microchannel Fabrication	24
Experimental Apparatus and Methodology	25
Results and Discussion	28
Summary and Conclusions	32
 CHAPTER 4 MICROPIV MEASUREMENT OF TURBULENT FLOW	
IN RECTANGULAR MICROCHANNELS WITH VARYING AS-	
PECT RATIOS	42
Abstract	42
Introduction	43
Microchannel Fabrication	47
Experimental Methodology	48
Experimental Setup	48
Measurement Error	50
Results and Discussion	52
Summary and Conclusions	57
 CHAPTER 5 EXAMINATION OF LARGE-SCALE STRUCTURES	
IN TURBULENT MICROCHANNELC FLOW USING MICROPIV.	
Abstract	67
Introduction	68
Experimental Techniques	71
Microchannel Fabrication	71
Experimental Setup	72
Measurement Error	73
Results and Discussion	74

Visualization of Turbulent Structures	74
Spatial Correlations and Integral Lengths along Channel Centerlines	75
Spatial Correlations and Length Scales at Various Distance from the Wall	79
Summary and Conclusions	80
CHAPTER 6 MICROFLUIDIC FLOW AROUND A SINGLE MICROSTRUCTURE IN A MICROCHANNEL	93
Abstract	93
Introduction	94
Microchannel Fabrication	96
Mold Fabrication	97
Microchannel Fabrication and Geometry	97
Experimental Methodology	98
Computational Methodology	101
Results and Discussion	102
Summary and Conclusion	106
CHAPTER 7 VELOCITY MEASUREMENTS OF LAMINAR AND TURBULENT FLOW IN RECTANGULAR MICROCHANNELS CONTAINING CUBIC MICROSTRUCTURES	118
Abstract	118
Introduction	118
Microchannel Fabrication and Experimental Procedure	121
Microchannel Fabrication	121
Experimental Setup and Procedure	122
Results and Discussion	125
Microchannel Containing the $20\ \mu\text{m} \times 20\ \mu\text{m} \times 20\ \mu\text{m}$ Microstructure	125
Microchannel Containing the $40\ \mu\text{m} \times 40\ \mu\text{m} \times 40\ \mu\text{m}$ Microstructure	129

Microchannel Containing the $50\ \mu\text{m} \times 50\ \mu\text{m} \times 50\ \mu\text{m}$ Microstructure . . .	131
Velocity Deficit Results	133
Summary and Conclusions	134
CHAPTER 8 CONCLUSIONS AND FUTURE DIRECTIONS . . .	151
Validation of MicroPIV in the Microfluidics Research	151
Hydraulic Diameter Effect in Microfluidic Flow	151
Aspect Ratio Effect in Microfluidic Flow	152
CFD Validation on Microfluidic Flow in Roughened Microchannels	153
Turbulence Enhancement Study on Microfluidic Flow in Roughened Microchan-	
nels	153
Future Directions	154
BIBLIOGRAPHY	156
ACKNOWLEDGEMENTS	166

LIST OF TABLES

Table 3.1	Geometric parameters of test microchannels with varying hydraulic diameters	34
Table 4.1	Geometric parameters of test microchannels with varying aspect ratios	59
Table 5.1	Geometric parameters of test microchannels	83
Table 5.2	Comparison of normalized turbulent length defined at the length where $R = 0.5$	84
Table 5.3	Wall effect on normalized turbulent length	85
Table 7.1	Geometric parameters of test microchannels and microstructures	137
Table 7.2	Summary of normalized centerline velocity fluctuations u'/u_{max} .	138

LIST OF FIGURES

Figure 2.1	Summary of the microchannel fabrication technique	17
Figure 2.2	Schematic of experimental setup	18
Figure 3.1	Summary of the microchannel fabrication technique	35
Figure 3.2	Schematic of experimental setup	36
Figure 3.3	Mean streamwise velocity profiles	37
Figure 3.4	Normalized mean streamwise velocity profiles	38
Figure 3.5	Streamwise velocity fluctuations	39
Figure 3.6	Transverse velocity fluctuations	40
Figure 3.7	Reynolds shear stress	41
Figure 4.1	Summary of the microchannel fabrication technique	60
Figure 4.2	Schematic of experimental setup	61
Figure 4.3	Mean streamwise velocity profiles for five different aspect ratios as measured by microPIV	62
Figure 4.4	Normalized streamwise velocity profiles for five different aspect ratios as measured by microPIV	63
Figure 4.5	Streamwise velocity fluctuation profiles for five different aspect ratios as measured by microPIV	64
Figure 4.6	Transverse velocity fluctuation profiles for five different aspect ratios as measured by microPIV	65

Figure 4.7	Reynolds shear stress profiles for five different aspect ratios as measured by microPIV	66
Figure 5.1	Schematic of experimental setup	86
Figure 5.2	Example velocity fields indicating the presence of turbulent structures	87
Figure 5.3	Spatial correlations at microchannel centerlines	88
Figure 5.4	Wall effect on spatial correlation functions Rx_{uu}	89
Figure 5.5	Wall effect on spatial correlation functions Rx_{vv}	91
Figure 6.1	Mold and microchannel fabrication processes using PDMS. View is a cross-section of the $50 \mu\text{m}$ half, cut through the microstructure.	108
Figure 6.2	Overhead view of the microstructure in the microchannel.	109
Figure 6.3	Schematic of the microPIV system	110
Figure 6.4	Locations of the velocity measurement planes in the microchannel	111
Figure 6.5	Velocity fields as measured by microPIV for at channel heights (every other vector shown)	112
Figure 6.6	Normalized streamwise velocity profiles for the microchannel at various depths for $Re_{D_h} = 108$ (Experiments - symbols; simulations - lines)	113
Figure 6.7	Normalized streamwise velocity profiles for the microchannel at various depths for $Re_{D_h} = 216$ (Experiments - symbols; simulations - lines)	114
Figure 6.8	Normalized streamwise velocity profiles for the microchannel at various depths for $Re_{D_h} = 431$ (Experiments - symbols; simulations - lines)	115

Figure 6.9	Normalized streamwise velocity profiles for the microchannel at various depths for $Re_{D_h} = 1078$ (Experiments - symbols; simulations - lines)	116
Figure 6.10	Planes of streamwise velocity contours for $Re_{D_h} = 216$	117
Figure 7.1	Fabrication of the microchannels with microstructure	139
Figure 7.2	Top view and side view of the microchannel with microstructure	140
Figure 7.3	Streamwise velocity and fluctuation profiles in the microchannel containing the $20 \mu\text{m} \times 20 \mu\text{m} \times 20 \mu\text{m}$ microstructure at $Re = 500$	141
Figure 7.4	Streamwise velocity and fluctuation profiles in the microchannel containing the $20 \mu\text{m} \times 20 \mu\text{m} \times 20 \mu\text{m}$ microstructure at $Re = 1500$	142
Figure 7.5	Streamwise velocity and fluctuation profiles in the microchannel containing the $20 \mu\text{m} \times 20 \mu\text{m} \times 20 \mu\text{m}$ microstructure at $Re = 2500$	143
Figure 7.6	Streamwise velocity and fluctuation profiles in the microchannel containing the $40 \mu\text{m} \times 40 \mu\text{m} \times 40 \mu\text{m}$ microstructure at $Re = 500$	144
Figure 7.7	Streamwise velocity and fluctuation profiles in the microchannel containing the $40 \mu\text{m} \times 40 \mu\text{m} \times 40 \mu\text{m}$ microstructure at $Re = 1500$	145
Figure 7.8	Streamwise velocity and fluctuation profiles in the microchannel containing the $40 \mu\text{m} \times 40 \mu\text{m} \times 40 \mu\text{m}$ microstructure at $Re = 2500$	146
Figure 7.9	Streamwise velocity and fluctuation profiles in the microchannel containing the $50 \mu\text{m} \times 50 \mu\text{m} \times 50 \mu\text{m}$ microstructure at $Re = 500$	147

Figure 7.10	Streamwise velocity and fluctuation profiles in the microchannel containing the $50 \mu\text{m} \times 50 \mu\text{m} \times 50 \mu\text{m}$ microstructure at $Re = 1500$	148
Figure 7.11	Streamwise velocity and fluctuation profiles in the microchannel containing the $50 \mu\text{m} \times 50 \mu\text{m} \times 50 \mu\text{m}$ microstructure at $Re = 2500$	149
Figure 7.12	Streamwise velocity deficit along the microchannel centerline for the various microstructures and Reynolds numbers	150
Figure 8.1	Top view and side view of the roughened microchannel with multiple microstructures	155

ABSTRACT

Microscopic particle image velocimetry (microPIV) experiments were performed on smooth and roughened microchannels. These measurements represent the first instantaneous velocity field measurements in a turbulent microscale flow.

The effect of hydraulic diameter on flow through smooth square polydimethylsiloxane (PDMS) microchannels was investigated by varying the hydraulic diameter from 200 μm to 640 μm for Reynolds numbers ranging from 200 through 3971. The data was analyzed to yield mean velocity profiles u , velocity fluctuations $\langle u' \rangle$ and $\langle v' \rangle$, and Reynolds stresses $-\langle u'v' \rangle$ and these were compared to experimental data of macroscale channel flow. The microscale and macroscale results agreed quite well, indicating there are no significant differences between microscale and macroscale channel flow.

Next, the effect of aspect ratio on flow through smooth rectangular microchannels was investigated by varying the aspect ratio from 0.97 to 5.69 for Reynolds numbers ranging from 200 through 3267. By analyzing mean velocity profiles u , velocity fluctuations $\langle u' \rangle$ and $\langle v' \rangle$, and Reynolds stresses $-\langle u'v' \rangle$ and comparing these experimental data with macroscale results, the data were used to clarify the discrepancies on transition in microfluidic flow due to the aspect ratio effect that was observed by previous researchers.

The statistical analysis of spatial correlation coefficients of velocity fluctuations to characterize large scale turbulent structures in these two experiments indicated that the large scale turbulent structures observed in microchannels are similar to their macroscale counterparts.

Flow within roughened microchannels of dimensions 600 μm x 400 μm with one

single microstructure measuring $120\ \mu\text{m} \times 120\ \mu\text{m} \times 43\ \mu\text{m}$ was studied by analyzing the velocity profiles in the wakes of microstructures. The data were obtained for comparison of the experimental velocities with CFD results at varying downstream locations and depths to provide for the validation of CFD in microfluidic flow study.

Finally, the experiments were performed in the roughened microchannels $600\ \mu\text{m} \times 400\ \mu\text{m}$ with one single cubic microstructure dimensioning at $20\ \mu\text{m}$, $40\ \mu\text{m}$, and $50\ \mu\text{m}$ for Reynolds number ranging from laminar to turbulent. The data obtained at upstream and various downstream locations and various depths indicated significant turbulence enhancement by introducing man-made surface roughness in microchannels.

CHAPTER 1 INTRODUCTION

Statement of General Purposes

Microfluidic Flow in Smooth Microchannels

Over the past two decades, microelectromechanical systems (MEMS) have become a rapidly developing technology, finding applications in many areas of engineering and science. Microfluidic MEMS devices involve the flow of liquid or gas to accomplish their design purpose. While many microfluidic MEMS devices, including such microscale analysis systems as gas chromatographs and blood and DNA analyzers, are characterized by low Reynolds number flow, there are some application areas where the Reynolds numbers can be much higher. Examples of these applications include the development of microscale heat exchangers for heat sinking applications, such as microelectronics cooling [Tuckerman and Pease (1981)], micro delivery systems [Henning (1998)], and microcontrol [Lipman (1999)]. Because of its importance in this crucial area, the characteristics of fluid flow in microchannels in both the laminar and turbulent regimes have attracted a great deal of attention from researchers. However, despite the efforts of many researchers in this area, there exist puzzling discrepancies in the results of previous studies. One often reported discrepancy is transition to turbulence at Reynolds numbers significantly lower than those observed at the macroscale. Early transition and/or higher friction factors were first observed and reported by Wu and Little (1983) whose experimental results showed transition from laminar to turbulent flow occurs at $Re = 350$ with 10% – 30%

higher friction factors. Besides from their work, Peng et al. (1994a,b); Peng and Peterson (1996a,b), Harms et al. (1999), Pfund et al. (2000), Mo et al. (2004), and numerous other researchers worked on microfluidic flow with different working fluid and different geometries of microchannels, the early transition behavior was reported occurring at lower Reynolds numbers than macroscale fluid flow. For example, Peng et al. (1994a,b) and Peng and Peterson (1996a,b) measured the friction factor of water flow through rectangular stainless steel microchannels with hydraulic diameters of 0.133 – 0.367 mm and aspect ratios of 0.333 – 1. The transition was reported occurring at $Re = 200 - 700$ and fully turbulent flow also occurring at lower Reynolds numbers than macroscale channels. Mala and Li (1999) investigated water flow through fused silica and stainless steel microtubes with diameters ranging from 50 to 254 μm , and based on observations of the nonlinear relationship between pressure gradient and the volumetric flow rate at $300 - 500 \leq Re \leq 1000 - 1500$ concluded that early transition was occurring. Gui and Scaringe (1995) investigated flow in microchannels with hydraulic diameters up to 388 μm and found transition at $Re = 1400$. One common point in many of these studies is that researchers who found early laminar-turbulent transition concluded that the relatively high surface roughness was one of the major reasons [Qu et al. (2000); Guo and Li (2003a,b); Sabry (2000); Toh et al. (2002)]. Furthermore, the transitional Reynolds number was reported varying with different hydraulic diameters and different aspect ratios [Pfund et al. (2000); Mo et al. (2004)]. However, not all researcher have observed the discrepancy. Good agreement of transitional Reynolds number, friction factor f , and Nussult number Nu between microfluidic flow and mascroscele results was observed in other studies [Celata et al. (2004); Hegab et al. (2002); Wu and Cheng (2003); Judy et al. (2002)]. For example, Qu and Mudawar (2002) studied the fluid flow characteristics of a microchannel heat sink with dimensions of 231 μm x 713 μm for Reynolds numbers between 39 and 1672. They found no evidence of early transition. Judy et al. (2002) measured frictional pressure drop of fluid flow in microtubes with hydraulic diameters

between 15 μm and 150 μm for three different fluids (water, methanol, isopropanol), two different tube materials (fused silica, stainless steel), and two different tube cross-section geometries (circular, square) and found no “distinguishable” deviation from macroscale viscous flow theory. Chung et al. (2002) performed experiments on single-phase flow in a 100 μm capillary tube. Good agreement was observed when the measured friction factor was compared with the conventional theory for deionized water flow, although surface roughness was not considered. Kohl et al. (2005) conducted experiments on the compressible flow ($6.8 < Re < 18814$) and incompressible flow ($4.9 < Re < 2068$) through straight channel with hydraulic diameters ranging from 25 to 100 μm . The friction factors were found to be determined accurately by data for macroscale channels. No evidence of early transition was observed within the test range. (The more detailed literature review would be included in each chapter for different research aspects.)

The previously mentioned experiments applied pressure drop measurements and temperature measurements in their investigations of microfluidic flow. The intrusive measurement with pressure transducer or temperature probe, whose dimension is not negligible compared to the microchannel dimensions, will unavoidably introduce more turbulence in the flow. Furthermore, the bulk fluid measurements are unable to supply information on velocity or temperature gradients which is necessary for the calculation of shearing stresses or heat transfer coefficients. In order to eliminate the effect of intrusive measurement used in the previous research, a recently developed non-intrusive, pointwise velocity measurement technique — microscale particle image velocimetry (microPIV) has been applied to study microchannel flow transition [Santiago et al. (1998); Meinhart et al. (1999); Olsen and Adrian (2000a); Devasenathipathy et al. (2003)]. Different criteria have been used to determine the onset of the transitional flow within microchannels. For example, Zeighami et al. (2000) observed the transition based on the repeatability of velocity data and the motion of particles normal to the measurement plane, while Lee et al. (2002) discovered the transition by the occurring of deviation of

velocity profiles and a broadening of cross correlation signal peak with turbulence intensity. Sharp and Adrian (2004) mentioned a quantitative way to define the onset of transition — the unsteady fluctuation of the centerline velocity. With this criteria, the onset of the transition was found occurring at Reynolds number 1800 – 2000 in glass microtubes with diameter from 50 to 247 μm .

In the dissertation that follows, microPIV has been used as an effective technique to study transitional and turbulent microchannel flow in an effort to clarify the previously reported results that generated often confusing and discrepant conclusions. The present study consists of two sub-series, these are 1) experiments to determine the effect of the hydraulic diameter on turbulent microchannel flow and 2) experiments to determine the effect of the aspect ratio on the turbulent microchannel flow. The hydraulic diameter experiments consist of measurements in microchannels with varying hydraulic diameters and a constant aspect ratio, while the aspect ratio experiments consist of measurements in microchannels with approximately constant hydraulic diameter and varying aspect ratios. Moreover, the characteristics of the large scale turbulent structures were determined from instantaneous velocity field data. The analysis of the large scale turbulent structures using velocity correlations of velocity fluctuations was performed to compare with previous macroscale experimental results.

Microfluidic Flow in Roughened Microchannels with Single Microstructure

A second component of the research in this dissertation consists of experiments on microchannels containing single microstructure. The study on microfluidic flow is necessary for the development of compact microscale heat exchangers which can transfer heat efficiently due to the high surface-area-to-volume ratio. The idea of adding of fins on heat exchanger tubes to increase the heat exchange efficiency in macroscale can be borrowed in microscale [Hopkins et al. (1999); Khrustalev and Faghri (1999)] without

inducing much friction loss along the microtubes. However, the design optimization of different sizes and shapes of microfins to obtain maximal heat transfer efficiency and minimal friction loss is a time-consuming and expensive process for experimental study.

Computational fluid dynamics (CFD) has proven to be an effective way for the design and optimization in macroscale. The flow field in CFD, along with initial conditions, boundary conditions, and geometries of fluidic channel can be easily modified compared to the time-consuming and expensive fabrication process in experiments. In order to broaden the application of CFD technique into microfluidic flow, the comparison between experimental data and CFD results needs to be accomplished to verify the accurate prediction of CFD in microfluidic flow behavior with complicated channel design.

In the dissertation that follows, microchannels were fabricated with a single microstructure attached along the the bottom wall centerline. With this man-made surface roughness which is large enough to make the channel wall surface roughness negligible, the research on the effect of roughness on microchannel flow becomes possible. At low Reynolds numbers, experimental data were collected using microPIV technique. Meanwhile, CFD results were calculated by a CFD group. The comparison between experimental data and CFD results within the wake length of the microfin shows primary validation of CFD results. The experiments at high Reynolds numbers which belonged to the transitional or turbulent flow were performed to study the turbulence enhancement by the single microstructure. Different dimensions of microstructure were chosen to study the effect of microstructure on turbulence enhancement.

Dissertation Contents and Contributions

The major contributions of the work presented in this dissertation include:

1. This work represents the *first measurements* of microPIV in turbulent microchannel flow (or any microscale flow, for that matter) with sufficient spatial resolution

such that the mean velocities, velocity fluctuations, *and* Reynolds stress could be obtained and reported. Previously, microPIV studies of turbulent microflows consisted only of mean velocities and centerline velocity fluctuations. Also, because of the unique spatial resolution of this measurement, large scale turbulent structures have been visualized and investigated for the *first time*. Indeed, before this work was performed, many researchers believed such measurement to be impossible.

2. The effect of hydraulic diameter on microchannel flow was studied by performing microPIV experiments from laminar to turbulent flow condition within square microchannels with different hydraulic diameters. The aspect ratios of these microchannels were designed 1.0. The experimental data of streamwise mean velocity $\langle u \rangle$, velocity fluctuations $\langle u' \rangle$ and $\langle v' \rangle$, and Reynolds stresses $\langle u'v' \rangle$ across the microchannels widths were reported as Reynolds number varies and were compared with previous study of macroscale fluidic flow. The onset of the transition was located by using the same criteria of Sharp and Adrian (2004). The experimental data would be helpful to clarify the discrepancy of the previous study on the transitional Reynolds number in microfluidics.

3. The effect of aspect ratio on microchannel flow was studied by performing experiments within rectangular microchannels with a constant hydraulic diameter and different aspect ratios. The experimental data of streamwise mean velocity $\langle u \rangle$, velocity fluctuations $\langle u' \rangle$ and $\langle v' \rangle$, and Reynolds stresses $\langle u'v' \rangle$ across the microchannels widths show the laminar, transitional, and turbulent behavior as Reynolds number varies. The criteria of Sharp and Adrian (2004) was used to define the onset of transitional flow. The comparison of the experimental data with previous macroscale results shows the aspect ratio effect of microchannels. The experimental data would be helpful to clarify the discrepancy of the previous study on the transitional Reynolds number in microfluidics.

4. Based on the above micorPIV experiments of the hydraulic diameter effect and aspect ratio effect, further study was performed to calculate the spatial correlation coefficient R and dimension of large scale turbulent structures L in the smooth microchannels. These statistical variables were then compared with previous macroscale turbulent flow experimental data using laser Doppler velocimetry (LDV) and Hot Wire Anemometry (HWA). It would be the *first time* to report the large scale turbulent structures and the spatial correlation coefficients in microchannel flow.
5. Microfluidic flow through roughened microchannels with microfins was studied to measure velocity profiles in the wake of microfins. The Reynolds numbers were not high enough to reach transitional or turbulent flow. The velocity data were captured at different downstream locations of the microfin and different depths normal to the bottom wall of the microchannels. The mean velocities in the wake of the microfin was compared with CFD results at various depths, downstream locations, and Reynolds numbers. Three-dimensional velocity contour slices were realized by combining the mean velocity data at various depths. By doing this, it is possible to prove the validation of CFD models in microfluidics.
6. The study of microfluidic flow within roughened microchannels at laminar, transitional, and turbulent flow condition is helpful in optimizing the design of the roughened microchannel surface for the turbulence enhancement. The experiment was performed within a rectangular microchannel with a single microstructure at the centerline of the bottom wall of microchannels. Three dimensions of cubic microstructures were selected. The velocity data were obtained at upstream and various downstream locations of the microstructure and various depths normal to the bottom wall of the microchannel. The work is supposed to supply a support for the man-made roughness in microchannel design.

CHAPTER 2 EXPERIMENTAL TECHNIQUE AND SETUP

Microchannel Fabrication

The microchannels used in the presented experiments were fabricated using PDMS replica molding [Son et al. (2002); McDonald et al. (2000); Jo et al. (2000); Folch et al. (1999)]. In this technique, the microchannel is made from polydimethylsiloxane (PDMS) that has been cast onto a mold master made of patterned photoresist on a silicon wafer. Two pieces of cast PDMS are brought together to assemble the final device. Devices fabricated using this technique are well suited for optical-based studies because the material is transparent between the wavelengths of 230 – 700 nm, giving nearly unlimited optical access to the interior of the microchannel at these wavelengths. Figure 2.1 summarizes the fabrication procedure.

Mold Master

The mold was made from patterned negative photoresist (SU-8 2100, MicroChem Corp., Newton, MA) on a silicon wafer (100 mm diameter, Montco Silicon Technologies, Inc, Spring City, PA). A puddle (around 50 mm wide) of photoresist was dispensed onto the substrate at static conditions. Spin-coating was then performed by rotating the substrate at 500 rpm for 10 sec, accelerating at 300 rpm/s, reaching highest spinning speed and holding for 30 sec. The viscosity of SU-8 2100 made it extremely difficult to deposit the resist without introducing bubbles. A soft bake was performed in a

convection oven at 65 °C for 45 min, then ramped to 95 °C and held for 2 hr. After soft baking, the selected region of the resist was exposed to UV light through a high-resolution transparency film acting as a photomask. A post-expose bake was performed to cross-link the resist, and the mold was then developed using 1-methoxy-2-propanol acetate (PMA) to remove the unexposed resist, leaving a mold in high relief for the channel.

Different mold fabrication parameters were used to meet the experimental requirements on different dimensions of microchannels. The different widths of the molds were controlled by varying the design drawings of transparencies, and the different depths were controlled by adjusting the amount of photoresist deposited on the wafer, the spinning speed of spin coater, the baking time, and the exposure time to UV light. Accurate determination of dimensions was essential to obtain reliable data. The optical measurement of the dimensions at various positions along the microchannels, accurate to within $\pm 10 \mu\text{m}$, indicated variations between 1.6% to 5%. The final length-averaged dimensions of the microchannel geometries were confirmed with a microscope and listed in detail in the following chapters as the characteristic geometries.

Casting PDMS

Polydimethylsiloxane (PDMS) elastomer (Sylgard(R) 184 Silicone Elastomer Kit, Dow Corning, Midland, MI) was used as the bulk material of the channel. The PDMS prepolymer was mixed with the curing agent in a 10:1 ratio and exposed to low pressure in a desiccator to remove bubbles formed during mixing. The prepolymer mixture was poured over the mold and again placed in the desiccator to remove bubbles. The PDMS casting was then cured in a convection oven at 60 °C for a minimum of 1 hr.

Microchannel Assembly

The final product consisted of two PDMS pieces: a top portion that was cast against the photoresist mold containing three walls of the channel and a bottom portion that had been cast against a blank silicon wafer. Assembly of the channel began with the removal of PDMS from the mold. The PDMS was then trimmed, and access holes were punched through the top portion of PDMS. The two halves were placed in an ethanol bath in an ultrasonic cleaner for 5 min to clean the surfaces, and subsequently dehydrated in a convection oven at 60 °C for 10 min. The two halves were then exposed to oxygen plasma (25 W, 1 Torr, 1 min) and immediately brought into conformal contact. The channel was kept in a convection oven at 60 °C for over 30 min to ensure complete adhesion at the PDMS/PDMS interface. Flexible tubing was coated with RTV sealant (732, Dow Corning, Midland, MI) and inserted into the access holes in the PDMS. Additional sealant was applied to ensure a complete seal. The sealant was allowed to cure for 2 days. This method for bonding the connecting tubing to the PDMS was strong enough to withstand even the highest flowrates studied in the microPIV experiments. Alternative methods of connecting tubing to the channel resulted in failure at the tubing/PDMS interface for high flow rates.

Resulting Device

The resulting microchannel was 5 cm long. Surface roughness inside the channel was measured with a Dektak IIA surface profile measuring system (Veeco Instruments Inc., Santa Barbara, CA). Linear surface profiles were taken of the cast PDMS. These measurements were limited, as the profilometer stylus could only be used on the top and bottom surfaces of the channel. For example, for the 320 μm microchannel, the arithmetic average roughness was calculated by the Dektak IIA software and was determined to be approximately 24 nm. This results in a relative roughness $\epsilon_s/D \approx 0.000074$.

Experimental Apparatus and Methodology

Experimental Setup and Method

The experimental apparatus, schematically shown in Fig. 2.2, consisted of two parts: (i) the flow delivery system; and (ii) the microPIV system. The working fluid, deionized water mixed with fluorescent particles, was driven by a microgear pump and pump head (115 VAC console digital dispensing drive and 0.084 ml/rev suction shoe gear pump head, Cole-Parmer Instrument Co., Vernon Hills, IL). This system was chosen over the more commonly used syringe pump for a number of reasons. First, the microgear pump was found to provide very steady flowrates with an accuracy of around 0.3%. Furthermore, collecting the large ensembles of microPIV images used in the present study required a far longer run time than the syringe pump could provide. Using the microgear pump allowed the system to be run at essentially steady-state, allowing large numbers of microPIV images to be taken during each run. Flow rate and temperature were monitored using a digital flowmeter (0 – 100 ml/min volumetric water flow meter, Cole Parmer Instrument Co., Vernon Hills, IL) with an accuracy of $\pm 2\%$ full scale. The temperature was carefully monitored during each run, as viscous dissipation could potentially increase the temperature and thus vary the fluid viscosity. A fluid reservoir was also added to the system to increase the thermal mass of fluid, and thus allow for longer run times before any viscous heating was discernable. The microchannel was connected to the flow delivery system with flexible tubing.

The microPIV system is shown in the lower portion of Fig. 2.2. The microchannel is placed on the stage of an inverted biological microscope [Nikon model T-300 Inverted Microscope], and fluid containing fluorescent microspheres is allowed to flow through the microchannel. A double pulsed Nd:YAG laser beam (Continuum, Santa Clara, CA) with wavelength of 532 nm is expanded before entering the microscope through an aperture in the back. The laser light is then directed toward the microchannel by a dichroic mirror

and passes through a microscope objective, illuminating the seed particles. The laser is capable of producing up to 120 mJ per laser pulse, but only a small fraction of this light is necessary for the microPIV experiments. An optical attenuator is therefore used to reduce the laser energy to approximately 3 mJ/pulse.

The 820 nm diameter fluorescent seed particles (Duke Scientific Co., Palo Alto, CA) are excited by the laser light and emit light at a peak excitation wavelength of 612 nm. A beamsplitter removes the illuminating and background light such that only the emitted light from the particles reaches the CCD camera. Two images are captured per realization, and the two images are analyzed using a cross-correlation technique to yield the instantaneous velocity vector field. The PIV system and software include a LaVision Flowmaster 3 camera and DaVis analysis software (LaVision Inc., Ypsilanti, MI).

One of the difficulties that had to be overcome in performing these experiments was seeding the flow sufficiently to allow instantaneous velocity vector fields to be obtained. Because obtaining high seed particle density can be difficult in microPIV, a common analysis technique is to ensemble-average many cross-correlation fields for an individual interrogation region, yielding an average velocity field with high spatial resolution. Indeed, using this technique, microPIV results have been reported with spatial resolutions as small as 1 μm [Meinhart et al. (1999)]. However, such measurements are of limited usefulness for turbulent flowfields, as they provide no information about instantaneous velocity fields. Therefore, in the present experiments, the authors chose to sacrifice some spatial resolution in order to achieve a high enough seed density to obtain accurate instantaneous velocity fields.

The concentration of the fluorescent particle solution was prepared to ensure at least 5 – 10 seed particles in each interrogation volume, resulting in a minimal amount of bad velocity vectors in each vector field [Keane and Adrian (1990)]. The necessary minimum seed density was estimated using the equation

$$N = CA(2Z_{corr}) \quad (2.1)$$

where, N is the desired minimum number of particles in each interrogation volume; C is the volumetric concentration of the fluorescent particle solution; A is the area of each interrogation window; and $2Z_{corr}$ is the depth of correlation [Olsen and Adrian (2000b); Bourdon et al. (2004)] which can be estimated by

$$Z_{corr} = \left[\frac{(1 - \sqrt{\epsilon})}{\sqrt{\epsilon}} \left(f^{\#2} d_p^2 \frac{5.95(M + 1)^2 \lambda^2 f^{\#4}}{M^2} \right) \right]^{1/2} \quad (2.2)$$

where $\lambda = 0.01$; $f^{\#}$ is the focal number of the lens; d_p is the particle diameter; M is the magnification, and k is the wavelength of light emitted by the particle. Eqn. 2.2 also provides an estimation of the measurement volume depth for the results reported here (note that an alternative equation for the depth of correlation derived by Meinhart et al. (2000) yields a similar result for the depth of correlation). In the present experiments, a 20X 0.45 NA objective was used, yielding a depth of correlation of $8.3 \mu\text{m}$. The interrogation windows in these experiments measure $28 \mu\text{m}$ square. Adjacent interrogation windows were overlapped by 50%, yielding a spatial resolution of $14 \mu\text{m}$. This spatial resolution allowed for 22 vectors to be measured across the width of the microchannel. Achieving this spatial resolution required a volumetric particle concentration of approximately 0.0567%. This volume fraction of seed particles is small enough that any two-phase effects are negligible, and the working fluid can be considered a single-phase fluid.

The timing between laser pulses was set such that the particles moved approximately 1/4th of an interrogation window between pulses. The interrogation windows measured 32 camera pixels square, thus the particles moved approximately 8 pixels between laser pulses. Assuming that the measured velocity is accurate to within 1/5th of a pixel [Prasad et al. (1992)] results in an experimental uncertainty of less than $\pm 2.5\%$.

In the microPIV experiments, deionized water was used as the working fluid. In order to prevent the buildup of contaminants in the system, air was pumped through the microchannel first to expel stagnant water and other contaminants. The fluorescent-particle-containing deionized water solution was then pumped through the microchannel at a specified volumetric flowrate. Although the flowrate was displayed by the digital gear pump, this reading was also confirmed by the serially connected flow meter in the microPIV system to ensure the accuracy of the reported Reynolds numbers.

The experiments were performed at various flow rates ranging from laminar to turbulent flow condition. For each set of experiments, sufficient time was allowed to pass after starting the micro gear pump to allow the flow to reach steady-state. For smaller flow rates, it took a longer time to reach a steady-state compared to higher flow rates. For all flow rates, a multipass interrogation scheme with decreasing smaller window sizes was used in the computation of the vector fields from 64 x 64 interrogation window to the final 32 x 32 interrogation window and adjacent interrogation windows were overlapped by 50%. The only post-processing performed on the vector fields was the removal of bad vectors. No smoothing of vector fields was performed. The number of velocity fields collected for each Reynolds number ranged from 600 for the lowest, laminar Reynolds numbers to 2000 for the transitional and turbulent Reynolds numbers.

Experimental Uncertainty

There are two sources of measurement errors in the microPIV experiments: errors introduced by random motion of the seed particles due to Brownian motion, and errors implicit in the interrogation of the PIV images. The significance of Brownian motion in the microPIV measurements can be determined by calculating the Brownian motion parameter [Olsen and Adrian (2000a)], defined as

$$\frac{d_e^2}{d_e^2 + 8M^2\beta^2 D\Delta t} \quad (2.3)$$

where the diffusion coefficient $D = kT/(6\pi\mu d_p)$, β^2 is a constant equal to 3.67, and d_e is the image diameter for a particle in the object plane [Adrian and Yao (1983)].

$$d_e = \sqrt{M^2 d_p^2 + d_s^2} \quad (2.4)$$

where $d_s = 2.44(M + 1)\lambda f^\#$ is the diameter of the diffraction-limited point spread function in the image plane; M is the magnification of the microscopic objective, = 20; d_p is the particle diameter, = 820 nm; λ is emitted light wavelength from particles, = 612 nm; $f^\#$ is focal number of objective, = $1/(2NA) = 1.11$.

For values of the Brownian motion parameter close to unity, Brownian motion has a negligible effect on the measured velocity. The analysis in the following chapters shows very small Brownian motion effects. Note that the fact that Brownian motion is negligible is not surprising, given the short Δt required for each of the measurements (on the order of 1 microsecond).

The relative unimportance of the error due to Brownian motion can also be demonstrated by comparing the particle displacement due to particle diffusion with the uncertainty in determining particle displacement. The distance that a particle is expected to diffuse due to Brownian motion can be found using [Santiago et al. (1998)]

$$s = \sqrt{2D\Delta t} \quad (2.5)$$

For values of the diffusion distance close to 0.0% relative to the experimental error, the effect of Brownian motion can be safely neglected. For example, in one case of my experiments at $Re = 2500$, the rms particle displacement due to Brownian motion is $0.001 \mu\text{m}$, which is only 0.5% of the experimental error. It would be safe to neglect the effects of Brownian motion.

The experimental error due to interrogation of the PIV images can be estimated by assuming that measured particle displacements are accurate to within approximately 1/10th of a seed particle image diameter [Prasad et al. (1992)]. Recall Eqn. 2.4, $d_e = 38 \mu\text{m}$ and yields the effective particle diameter when projected back into flow coordinates at $1.9 \mu\text{m}$, meaning that the measured particle displacement in the microPIV experiments should be accurate to within $0.19 \mu\text{m}$. For the present experiments, the particles moved approximately $8 \mu\text{m}$ between laser pulses, resulting in an experimental uncertainty of 2.3%.

The data were taken at locations far enough downstream of the microchannel entrance to ensure fully developed flow and avoid any entrance length effects [Lee et al. (2002)]. This was verified by taking measurements at different downstream locations and comparing the mean velocity profiles. In all cases, velocity fields were measured along the microchannel midplane by finding the maximal velocity peaks at laminar flow.

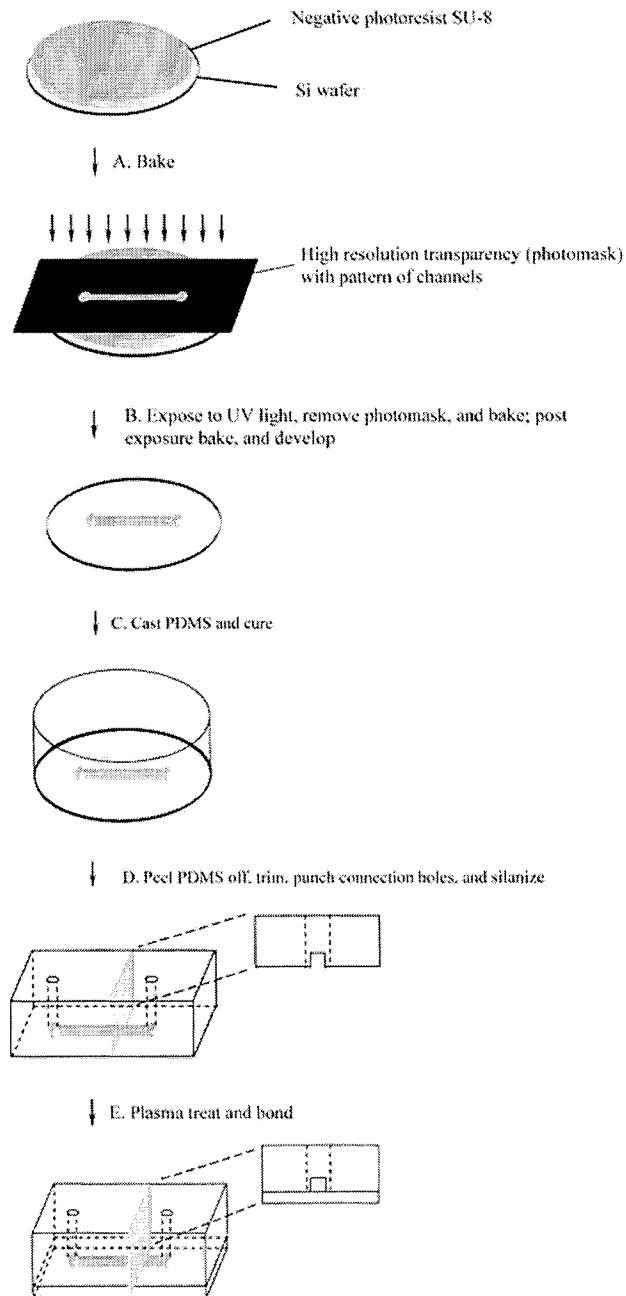


Figure 2.1 Summary of the microchannel fabrication technique

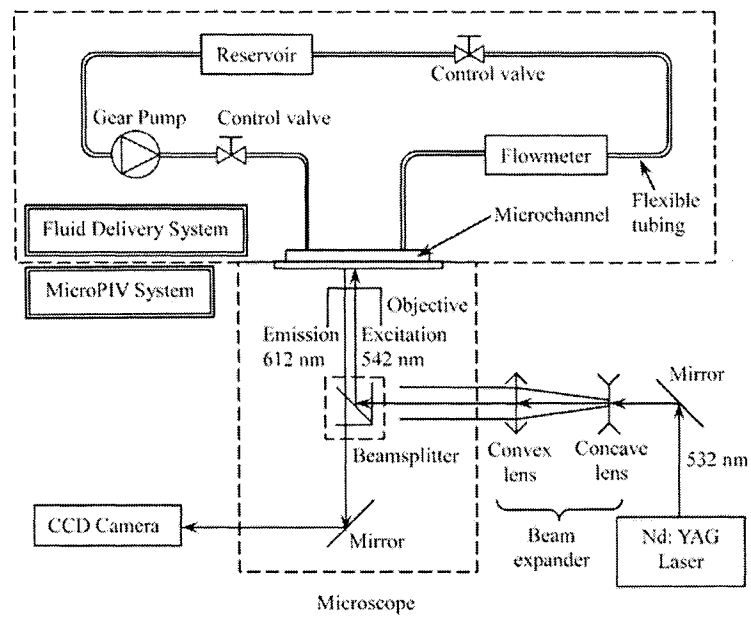


Figure 2.2 Schematic of experimental setup

CHAPTER 3 MICROPIV MEASUREMENT OF TURBULENT FLOW IN SQUARE MICROCHANNELS WITH VARYING HYDRAULIC DIAMETERS

A paper accepted by *International Journal of Heat and Fluid Flow*

H. Li and M. G. Olsen

Abstract

Microscopic particle image velocimetry (microPIV) experiments were performed on square polydimethylsiloxane (PDMS) microchannels with hydraulic diameters ranging from 200 μm to 640 μm and for Reynolds numbers ranging from 200 through 3971. Deionized water mixed with fluorescent seed particles was used as the working fluid. There was no evidence of early transition to turbulence, with transition observed at Reynolds numbers between 1718 and 1885 for the different sized microchannels. The 200 μm microchannel structurally failed before fully turbulent flow was reached, but for the other microchannel geometries studied, the flow was found to become fully turbulent at Reynolds numbers ranging from 2600 to 2900. The measured fully turbulent $\langle u' \rangle / u_{max}$ velocity fluctuations agreed well with results for turbulent duct flow for the 320 μm , 480 μm and 640 μm microchannels. The measured fully turbulent $\langle v' \rangle / u_{max}$ fluctuations agreed well with turbulent duct flow results for the 480 μm and 640 μm microchannels, but were 20 – 40% lower than turbulent duct flow results for the 320 μm microchannel. Similar results were observed in the measured Reynolds shear stresses.

Spatial correlations of velocity fluctuations were also measured in the transverse direction, and in the Ru0u0 spatial correlation results, the 480 μm and 640 μm microchannel results agreed very well with turbulent pipe flow results, but the 320 μm results showed significant differences.

Introduction

The rapid development of microfluidic microelectromechanical systems (MEMS) has resulted in great interest in the understanding of flow behavior in microchannels due to their importance in such applications as microelectronics cooling [Tuckerman and Pease (1981)], drug delivery, biotechnical analysis, and telecommunication technologies [Henning (1998); Lipman (1999)]. The fluid flow characteristics of microchannels are important to the design of microfluidic devices, and thus this topic is of significant importance to the further development of microfluidic MEMS devices. Because of this importance, researchers have been working in this area since the 1980s, and many interesting, yet often times conflicting, results have been reported.

In many previous studies, researchers measured the friction factor or Nusselt number in microchannel flow and compared the results with conventional theory. For example, Wu and Little (1983) measured the friction factors of gas flow (nitrogen, hydrogen, and argon) through etched glass and silicon microchannels with hydraulic diameters ranging from 45.46 μm to 83.08 μm . Their results suggested an early onset of transition around $Re = 350$, far from the conventional macroscale transitional Reynolds number of 1800 – 2300. They also measured abnormally high values of friction factor and attributed this to the large relative roughness of the etched channels. Peng et al. (1994a) and Peng and Peterson (1996a) measured the friction factor of water flow through rectangular stainless steel microchannels with hydraulic diameters of 0.133 – 0.367 mm and aspect ratios of 0.333 – 1. Their results showed transition occurring at $Re = 200 - 700$ and

fully turbulent flow also occurring at lower Reynolds numbers than macroscale channels. Mala and Li (1999) investigated water flow through fused silica and stainless steel microtubes with diameters ranging from 50 to 254 μm , and based on observations of the nonlinear relationship between pressure gradient and the volumetric flow rate at $300 - 500 \leq Re \leq 1000 - 1500$ concluded that early transition was occurring. They also found rough agreement between the friction factor of experimental data and conventional theory at low Reynolds numbers, but, as Reynolds number was increased, the experimental friction factor showed a significant increase from macroscale results [Qu et al. (2000)], a phenomenon they attributed to surface roughness. Pfund et al. (2000) detected the turbulent transition by friction factor and flow visualization. Their test channels had high aspect ratios and depths ranging from 128 μm to 521 μm . The Reynolds numbers investigated were from 60 to 3450. Slightly early "sudden, but not discontinuous" transition was observed and friction factor values significantly greater than those predicted by macroscale correlations were measured. Other researchers claimed to observe early transition, but measured friction factors that agreed well with macroscale correlations. For example, Gui and Scaringe (1995) investigated flow in microchannels with hydraulic diameters up to 388 μm and found transition at $Re = 1400$, but found friction factors that agreed well with the conventional theory. Wu and Cheng (2003) found the onset of transition at $Re = 1500$ for water flow in smooth, trapezoidal silicon microchannels with hydraulic diameters in the range of 25.9 – 291.0 μm , but the experimental data matched well with the analytical solution for incompressible, fully developed, laminar flow under a no-slip boundary condition. One common point in many of these studies is that researchers who found early laminar-turbulent transition concluded that the relatively high surface roughness was one of the major reasons [Qu et al. (2000); Guo and Li (2003a,b); Sabry (2000); Toh et al. (2002)].

However, there are also researchers whose results on transition agreed well with conventional predictions even with the same magnitude of channel surface roughness (1 –

2%) as researchers mentioned before. For instance, Hegab et al. (2001, 2002) performed experiments on single-phase flow in microchannels with hydraulic diameters ranging from $112\ \mu\text{m}$ to $210\ \mu\text{m}$ and aspect ratios from 1.0 to 1.5. They reported transition between $Re = 2000 - 4000$ and friction factor results that were slightly lower than the conventional predictions. Qu and Mudawar (2002) studied the fluid flow characteristics of a microchannel heat sink with dimensions of $231\ \mu\text{m} \times 713\ \mu\text{m}$ for Reynolds numbers between 39 and 1672. They found no evidence of early transition, and the measured pressure drop showed good agreement with corresponding numerical predictions. Judy et al. (2002) measured frictional pressure drop of fluid flow in microtubes with hydraulic diameters between $15\ \mu\text{m}$ and $150\ \mu\text{m}$ for three different fluids (water, methanol, isopropanol), two different tube materials (fused silica, stainless steel), and two different tube cross section geometries (circular, square) and found no "distinguishable" deviation from macroscale viscous flow theory. Chung et al. (2002) performed experiments on single-phase flow in a $100\ \mu\text{m}$ capillary tube. Good agreement was observed when the measured friction factor was compared with the conventional theory for deionized water flow, although surface roughness was not considered. The measured velocity also matched the theoretical profile for laminar flow in a circular microchannel. For gas flows, the compressibility effect was found to be important to match the experimental data with theory.

The previously mentioned experiments applied pressure drop measurements in their investigations of microfluidic flow. However, since discrepancies exist in the existing literature on microfluidic flow transitional behavior [Celata et al. (2004)], some researchers have attempted to clarify it using a relatively new experimental technique, microscopic particle image velocimetry (microPIV) [Santiago et al. (1998); Meinhart et al. (1999); Olsen and Adrian (2000b); Devasenathipathy et al. (2003)]. Because of its advantage as a non-invasive measurement technique in microscale flow systems, microPIV has been widely used in researching many different microscale flows [Stone et al. (2002); Klank

et al. (2002); Kim et al. (2002)]. Using microPIV, Zeighami et al. (2000) performed an experimental investigation on transition in a silicon microchannel with dimensions $150 \mu\text{m} \times 100 \mu\text{m} \times 1 \text{ cm}$. The repeatability of the velocity data and the motion of seed particles perpendicular to the measurement plane were taken as the criteria to distinguish laminar and turbulent flow. Using this criteria, early transition at $Re = 1200 - 1600$ was observed. However, in this study, the particle seed density was not sufficient for Reynolds stresses to be measured or for turbulent flow structures to be observed. Lee et al. (2002) studied flow up to $Re = 2900$ in a rectangular microchannel of aspect ratio 2.65 and hydraulic diameter $380 \mu\text{m}$. In their work, the deviation of velocity profiles and a broadening of the microPIV cross-correlation signal peak with turbulence intensity was used to define transition at $Re = 2900$. Sharp and Adrian (2004) performed a detailed set of pressure drop and microPIV experiments on transitional flow in microtubes. Round glass microtubes with diameters between 50 and $247 \mu\text{m}$ were used along with working fluids of different polarities. In their microPIV experiments, fluctuations of the centerline velocity were taken as indicators of the transition to turbulence. In the laminar regime, centerline velocity fluctuations of around 1% (due to experimental noise) were observed. However, at higher Reynolds numbers, the centerline velocity fluctuations increased, and the first abrupt increase of the rms value of centerline velocity was taken as the onset of transitional flow. Using this definition, transition was observed between $1800 < Re < 2200$, and thus they concluded that anomalous transition did not occur.

The present work uses microPIV to obtain instantaneous velocity field data for flow through square microchannels with hydraulic diameters ranging from $200 \mu\text{m}$ to $640 \mu\text{m}$ and aspect ratios close to 1. The particle seeding was dense enough that Reynolds stresses could be measured throughout the microchannel. The measured Reynolds stresses are then compared with classical results for macroscale ducts. Finally, spatial correlations of velocity fluctuations are calculated and reported.

Microchannel Fabrication

The straight microchannels used in the present experiments were fabricated using PDMS replica molding [Anderson et al. (2000); Jo et al. (2000)]. A brief summary of the fabrication process follows (greater detail of the fabrication process can be found in [Li et al. (2005)]). Figure 3.1 summarizes the fabrication procedure graphically. The channel molds were made from patterned negative photoresist (SU-8 2100, MicroChem Corp., Newton, MA) on a silicon wafer (100 mm diameter, Montco Silicon Technologies, Inc, Spring City, PA). A coating of the photoresist was spun on the silicon wafer, and select regions of the coated wafer were exposed through a transparency film to ultraviolet light. The photoresist was then developed resulting in a mold of the microchannel geometry in relief. Polydimethylsiloxane (PDMS) elastomer (Sylgard(R) 184 Silicone Elastomer Kit, Dow Corning, Midland, MI) was then cast on the mold and baked. Finally, the two halves of the microchannel are plasma treated and bonded to form the finished microchannel.

Microchannels were fabricated with four different hydraulic diameters and with aspect ratios very close to 1. The different widths were controlled by varying the design drawings of transparencies, and the different depths were controlled by adjusting the amount of photoresist deposited on the wafer, the spinning speed of spin coater, the baking time, and the exposure time to UV light. Accurate determination of dimensions was essential to obtain reliable data. The optical measurement of the dimensions at various positions along the microchannels, accurate to within $\pm 10 \mu\text{m}$, indicate variations between 1.6% and 5%. The final length-averaged dimensions of the four different microchannel geometries were confirmed with a microscope and are listed in Table 3.1.

The resulting microchannels were then tested for inner surface roughness using Dek-tak IIA surface profile measuring system (Veeco Instruments Inc., Santa Barbara, CA). Liner surface profiles were taken of the cast PDMS. These measurements were limited,

as the profilometer stylus could only be used on the top and bottom surfaces of the channel. For example, for the 320 μm microchannel, the arithmetic average roughness was calculated by the Dektak IIA software to be approximately 24 nm. This results in a relative roughness $\epsilon_s/D \approx 0.000074$.

Experimental Apparatus and Methodology

The experimental system, schematically shown in Fig. 3.2, consisted of two sub-systems: (i) the flow delivery system; and (ii) the microPIV system. The flow was driven by a micro gear pump and pump head (115 VAC console digital dispensing drive and 0.084 mL/rev suction shoe gear pump head, Cole-Parmer Instrument Co., Vernon Hills, IL) that provided constant flow rates accurate to within $\pm 0.3\%$. The working fluid was deionized water. Flow from the gear pump passed through the microchannel, then through a digital flowmeter (0 – 100 mL/min volumetric water flow meter, Cole-Parmer Instrument Co., Vernon Hills, IL), and finally through a fluid reservoir before returning to the gear pump to begin a second cycle. The flowmeter contained a thermocouple so fluid temperature could be carefully monitored during each run. The purpose of the fluid reservoir was to increase the thermal mass of the fluid in the system, so that viscous dissipation did not result in any temperature change of the working fluid (and hence a change in fluid viscosity) during the experimental runs.

The microPIV system is shown in the lower portion of Fig. 3.2. A double pulsed Nd:YAG laser beam (Continuum, Santa Clara, CA), attenuated to 3 mJ/pulse with a wavelength of 532 nm, was expanded and directed into an aperture in the rear of the microscope. Nine-hundred nanometers diameter fluorescent seed particles (Duke Scientific Co., Palo Alto, CA) were excited by the laser light and emitted light at a peak excitation wavelength of 612 nm. The excited light, filtered by a beamsplitter to remove illuminating and background light, was then imaged through the inverted

biological microscope [Nikon model T-300 Inverted Microscope] and an objective lens with a magnification of 20x and a numerical aperture of 0.45. A LaVision Flowmaster 3 camera (LaVision Inc., Ypsilanti, MI) was used to capture the PIV image pairs for cross-correlation analysis.

The concentration of the fluorescent particle solution was prepared such that a sufficient number of seed particles fell within depth of correlation [Olsen and Adrian (2000b); Bourdon et al. (2004)] of each interrogation region that erroneous vector measurements were minimized. In the present experiments, the 20x 0.45 NA objective yields a depth of correlation of $8.3 \mu\text{m}$ (an alternate definition of depth of correlation by Meinhart et al. (1999) yields a similar result for depth of correlation). Using interrogation windows measuring $28 \mu\text{m}$ square (for the $200 \mu\text{m}$, $320 \mu\text{m}$, and $480 \mu\text{m}$ microchannels) and $56 \mu\text{m}$ square (for the $640 \mu\text{m}$ microchannel) and overlapping each interrogation region by 50% yielded spatial resolutions of $14 \mu\text{m}$ and $28 \mu\text{m}$, respectively. Achieving this spatial resolution required a volumetric particle concentration of approximately 0.057%. This volume fraction of seed particles was small enough that any two-phase effects were negligible, and the working fluid could be considered a single-phase fluid.

The experiments were performed at various flow rates corresponding to Reynolds numbers ranging from 200 up to 3971. For each set of experiments, sufficient time was allowed to pass after starting the micro gear pump to allow the flow to reach steady state. For smaller flow rates, it took a longer time to reach a steady state compared to higher flow rates. A multi-pass interrogation scheme with decreasingly smaller window sizes was used in the computation of the vector fields to reach the final 32×32 pixels (for the $200 \mu\text{m}$, $320 \mu\text{m}$, and $480 \mu\text{m}$ microchannels) and 64×64 pixels (for the $640 \mu\text{m}$ microchannel) interrogation windows. The only postprocessing performed on the vector fields was the removal of bad vectors. No smoothing of vector fields was performed. The number of velocity fields collected for each Reynolds number ranged from 600 for the lowest, laminar Reynolds numbers to 2000 for the transitional and turbulent Reynolds

numbers.

There are two sources of measurement error in the microPIV experiments: errors introduced by random motion of the seed particles due to Brownian motion, and errors implicit in the interrogation of the PIV images. The significance of Brownian motion in the microPIV measurements can be determined by calculating the *Brownian motion coefficient* [Olsen and Adrian (2000a)], defined as

$$\frac{d_e^2}{d_e^2 + 8M^2\beta^2 D\Delta t} \quad (3.1)$$

where $D = KT/(6\pi\mu d_p)$ and β^2 is a constant equal to 3.67. For values of the Brownian motion coefficient close to unity, Brownian motion has a negligible effect on the measured velocity. For the 640 μm microchannel at $Re = 1500$, the Brownian motion coefficient is equal to 0.9988, indicating that Brownian motion effects are small. For the smaller microchannels, or at higher Reynolds numbers in the 640 μm microchannel, the Brownian motion effect is even smaller, due to the smaller Δt required for these measurements. Note that the fact that Brownian motion is negligible is not surprising, given the short Δt required for each of the measurements (on the order of 1 μs).

The experimental error due to interrogation of the PIV images can be estimated by assuming that measured particle displacements are accurate to within approximately 1/10th of a seed particle image diameter [Prasad et al. (1992)]. For the microPIV experiments, the image diameter for a particle in the object plane can be approximated as [Adrian and Yao (1983)]

$$d_e = \sqrt{M^2 d_p^2 + d_s^2} \quad (3.2)$$

For the present experiments, $d_e = 1.9 \mu\text{m}$ projected back into flow coordinates, meaning that the measured particle displacement in the microPIV experiments should be accurate to within 0.19 μm . For the 200 μm , 320 μm , and 480 μm microchannels ex-

periments, the maximum particle displacement was approximately $7 \mu\text{m}$ between laser pulses, resulting in an experimental uncertainty of 2.7%, and for the 640 μm microchannel experiments, the particles moved approximately $14 \mu\text{m}$, resulting in an experimental uncertainty of around 1.4%. Note that these errors are representative of the high velocity regions in the microchannel since these regions have the largest particle displacements. The experimental error will be higher in the near-wall regions where velocities are lower, as the seed particles in these regions will exhibit smaller displacements between laser pulses. For example, the experimental error at a location where the local mean velocity is one-half the maximum mean velocity will be twice the earlier reported experimental errors.

The data were taken at locations far enough downstream of the microchannel entrance to ensure fully developed flow and avoid any entrance length effects [Lee et al. (2002)]. This was verified by taking measurements at different downstream locations and comparing the mean velocity profiles. In all cases, velocity fields were measured along the microchannel midplane by finding the maximal velocity peaks at laminar flow.

Results and Discussion

The ensemble-averaged streamwise velocity profiles for various Reynolds numbers are presented in Fig. 3.3, together with the corresponding fully developed laminar analytical solutions for a rectangular pipe [White (1991)]. The transverse positions have been normalized by $1/2$ of the width of the microchannel, with 0 corresponding to the microchannel centerline and 1 corresponding to the microchannel wall. For the $200 \mu\text{m}$ microchannel, the comparison shows good agreement between the measured velocity and the laminar solution until $Re = 1708$, with deviations from the laminar solution over most of the profile of less than 1%. The deviation from the laminar profile becomes apparent at $Re = 1792$ where the experimental data become less parabolic with a lower

peak value at centerline and higher velocity close the wall, a typical phenomenon of transitional or turbulent flow. Efforts were made to reach higher Reynolds numbers and fully turbulent flow, but unfortunately this size channel kept catastrophically failing due to the high pressure at higher Reynolds numbers. The same measurements were repeated for the 320 μm , 480 μm , and 640 μm microchannels, and the data are shown in Fig. 3.3(b), 3.3(c), and 3.3(d), respectively. It is interesting to note that in all of the cases investigated, deviation from the analytical laminar solution occurs before any evidence of transition to turbulence is observed in the plots of velocity fluctuations (Figs. 3.5 and 3.6). This behavior is consistent with previous studies of channel and pipe flow at both the macroscale [Wyganski and Champagne (1973)] and the microscale [Sharp and Adrian (2004)]. As Reynolds number is further increased, the measured velocity near the channel centerline deviates further from the laminar prediction and becomes smaller, while the velocity near the channel walls becomes greater, and the measured velocity profiles begin to resemble fully turbulent flow. The changing shape of the mean velocity profiles with increasing Reynolds number is more distinctive in Fig. 3.4, where the velocity profiles are normalized by the centerline velocity. Fig. 3.4 also shows the difference between the experimental data and fully turbulent duct flow. At lower Reynolds numbers, the velocity profiles are grouped together near the analytical laminar solution. As Reynolds number increases, the velocity profiles first deviate from the laminar solution, and then become grouped together again with only small differences between them (even if there is significant increase of Reynolds number), indicating the onset of fully turbulent duct flow. At the highest Reynolds numbers studied, good agreement is observed between the measured velocity profiles and the velocity profile for fully turbulent macroscale channel flow [Schlichting (1987)] for a smooth channel with maximum velocity 100 cm/s and Reynolds number of 4000 based on hydraulic diameter, suggesting that the microchannel flow has reached a fully turbulent state and presented a good agreement with macroscale experimental results.

In order to quantify the turbulence in the microchannels, velocity fluctuations and Reynolds shear stresses were computed from the microPIV data. Figs. 3.5 – 3.7 show the dimensionless profiles of $\langle u' \rangle / u_{max}$, $\langle v' \rangle / u_{max}$, and $-\langle u'v' \rangle / u_{max}^2$, respectively for each of the microchannels as a function of Reynolds number. For all the microchannels, the measured centerline values of $\langle u' \rangle / u_{max}$ exhibit a band of overlapped fluctuation values around 1.5% at Reynolds numbers lower than $Re = 1500$, as shown in Fig. 3.5. The measured fluctuations at these low Reynolds numbers are not evidence of turbulence, but are instead due to the measurement uncertainty in the microPIV experiments.

In their microPIV experiments in microtubes, Sharp and Adrian (2004) defined transition to turbulence based on a significant increase in the measured centerline streamwise velocity fluctuations. Using this definition for transition in the present experiments, jumps in the streamwise velocity fluctuations are observed at $Re = 1792, 1885, 1718,$ and 1823 for the $200 \mu\text{m}, 320 \mu\text{m}, 480 \mu\text{m},$ and $640 \mu\text{m}$ microchannels, respectively. These measured transitional Reynolds numbers of $1718 - 1885$ for square microchannels agree very well with the transitional Reynolds numbers of $1800 - 2000$ that Sharp and Adrian reported for round microtubes. Thus, as in the experiments of Sharp and Adrian, no evidence of early transition was observed in the present study. Note that nearly identical transitional Reynolds numbers are obtained if transition is instead defined by a jump in the centerline transverse velocity fluctuations. Using this definition, transition is observed at $Re = 1885, 1718,$ and 1823 for the $320 \mu\text{m}, 480 \mu\text{m},$ and $640 \mu\text{m}$ microchannels (the $200 \mu\text{m}$ microchannel structurally failed at $Re > 1792$, before a jump in the centerline transverse velocity fluctuations could be observed).

As the Reynolds number is increased above transition, increases in both the streamwise and transverse velocity fluctuations are observed. Eventually, the fluctuations no longer increase with increasing Reynolds number, and this behavior, along with the mean velocity profiles approaching that of fully turbulent flow (Fig. 3.4), is indicative of a fully turbulent state being reached. Observing Fig. 3.5 once more, it is apparent

that the 200 μm microchannel failed before a fully turbulent state was reached, since the $Re = 1708$ and $Re = 1792$ results do not overlap. However, fully turbulent flow was observed in the three other microchannel geometries investigated. Both the $\langle u' \rangle / u_{max}$ and the $\langle v' \rangle / u_{max}$ fluctuations consistently overlap for the 320 μm , 480 μm , and 640 μm microchannels at Reynolds numbers somewhere in the range $2400 < Re < 2600$. Coupling these results with the mean velocity profiles shown in Fig. 3.4 suggest fully turbulent flow being reached in the approximate range of $2600 < Re < 2900$.

The solid lines in Figs. 3.5 and 3.6 represent experimental results for turbulent duct flow [Schlichting (1987)]. The experimentally determined fully turbulent values for $\langle u' \rangle / u_{max}$ presented in Fig. 3.5 are slightly higher than classical results for turbulent duct flow [Schlichting (1987)], but in general, the agreement is good, as all of the results fall within the experimental uncertainty. Similarly, the results of $\langle v' \rangle / u_{max}$ for the 480 μm and 640 μm microchannels agree very well with the turbulent duct flow results, with the microchannel results slightly higher than the duct flow results over most of the microchannel, but falling within the experimental uncertainty. Although lower $\langle v' \rangle / u_{max}$ fluctuations are measured near the walls, these results also fall within the experimental uncertainty (note that the measurement uncertainty is higher near the walls because of smaller particle displacements due to lower velocities [Prasad et al. (1992)]). The first suggestion of discrepancies between the microchannel results and turbulent duct flow is observed in the measured $\langle v' \rangle / u_{max}$ fluctuations for the 320 μm microchannel, which are consistently 20 – 40% lower than the results for turbulent macroscale duct flow.

Figure 3.7 shows the Reynolds shear stress, $-\langle u'v' \rangle / u_{max}^2$, for the four microchannels. In the laminar flow regime, the value of $-\langle u'v' \rangle / u_{max}^2$ is very close to zero, as expected. For the 200 μm microchannel, $-\langle u'v' \rangle / u_{max}^2$ is close to zero for all the Reynolds numbers studied. This is not surprising, since the $\langle v' \rangle / u_{max}$ fluctuations were also seen to be close to zero. For the larger microchannels, as the flow transitions and turbulence become significant, the profiles exhibit a continual increase in value. The value of $-\langle u'v' \rangle / u_{max}^2$

is nearly zero in the center of the microchannel, as required by symmetry. The peak values in the plot correspond to the locations where the turbulent friction and momentum transportation have their largest values, the locations of highest values of first derivative of $\langle u' \rangle / u_{max}$ and $\langle v' \rangle / u_{max}$ fluctuations in Figs. 3.5 and 3.6, respectively. The solid lines in Fig. 3.7 represent the results for fully turbulent macroscale duct flow [Schlichting (1987)]. For the 480 μm and 640 μm microchannels (Fig. 3.7(c) and 3.7(d)), an excellent match is observed between the fully turbulent microchannel and macroscale duct flow results over most of the width of the microchannels. There are some discrepancies close to the walls, but as previously stated, measurement errors are higher in these regions. However, for the 320 μm microchannel (Fig. 3.7(b)), the fully turbulent experimental data of $-\langle u'v' \rangle / u_{max}^2$ are slightly lower than macroscale turbulent duct flow results.

Summary and Conclusions

Microscopic particle image velocimetry was used to measure instantaneous velocity fields in square microchannels with hydraulic diameters ranging from 200 μm to 640 μm . Data were collected for Reynolds number ranging from 200 up to 3971. Mean velocity profiles, velocity fluctuations, Reynolds stresses, and spatial correlations of velocity fluctuations were calculated from the microPIV data. With transition to turbulence defined by an increase in the measured centerline velocity fluctuations, transition was observed at Reynolds numbers ranging from 1718 to 1885. These data agree very well with the recent experiments of [Sharp and Adrian (2004)] in round microtubes in which transition was observed at Reynolds numbers between 1800 and 2000. Thus, no evidence of early transition was observed in the present experiments. The 200 μm microchannel structurally failed before fully turbulent flow could be reached. Fully turbulent flow was observed for the larger microchannels (hydraulic diameters of 320 μm , 480 μm , and 640 μm) at Reynolds numbers ranging from 2600 to 2900.

For the fully turbulent flow in the 320 μm , 480 μm , and 640 μm microchannels, the measured $\langle u' \rangle / u_{max}$ fluctuation was slightly higher than results for macroscale turbulent duct flow, but in general agreed well with the macroscale results. There was some variation in the $\langle v' \rangle / u_{max}$ fluctuation results for the microchannels studied. The $\langle v' \rangle / u_{max}$ fluctuations agreed well with macroscale turbulent duct flow results for the 480 μm and 640 μm microchannels, but were 20 – 40% smaller than the results for turbulent duct flow in the 320 μm microchannel. Similar results were observed in the measured Reynolds shear stresses, with the 480 μm and 640 μm microchannel results agreeing well with the macroscale results, and the 320 μm microchannel results showing slight discrepancies.

Table 3.1 Geometric parameters of test microchannels with varying hydraulic diameters

Channel Name	W (μm)	H (μm)	D_h (μm)	Aspect Ratio (W/H)
200 μm	200	200	200	1.00
320 μm	320	330	325	0.97
480 μm	480	490	485	0.98
640 μm	640	640	640	1.00

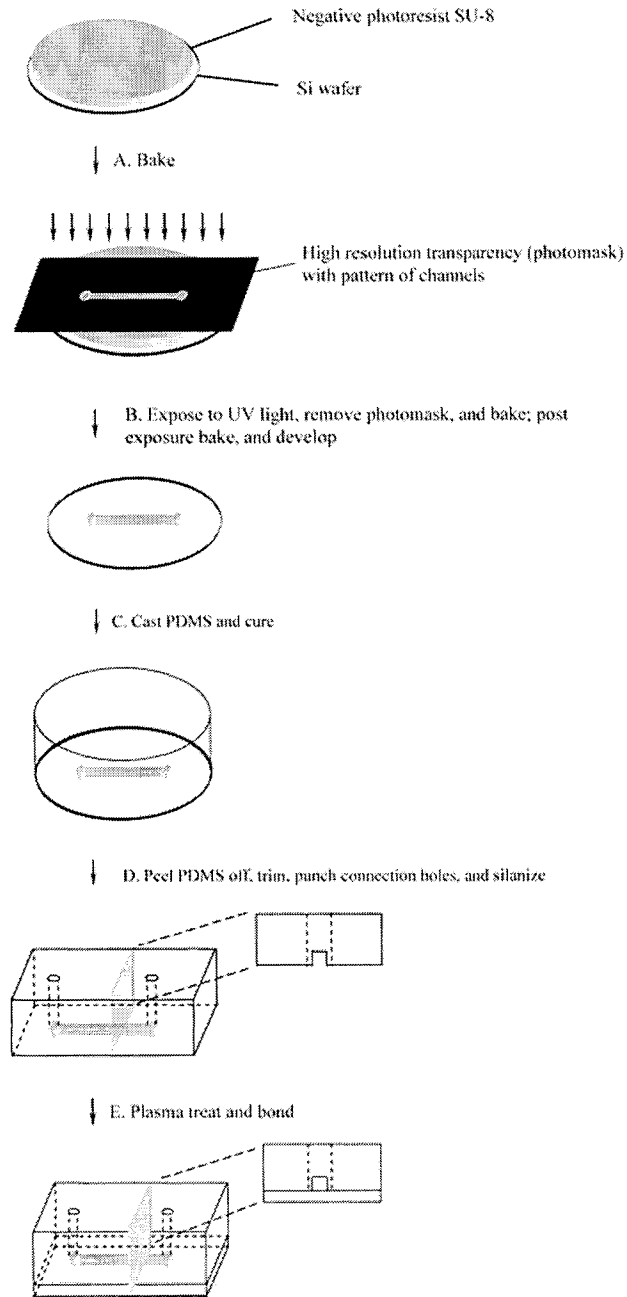


Figure 3.1 Summary of the microchannel fabrication technique

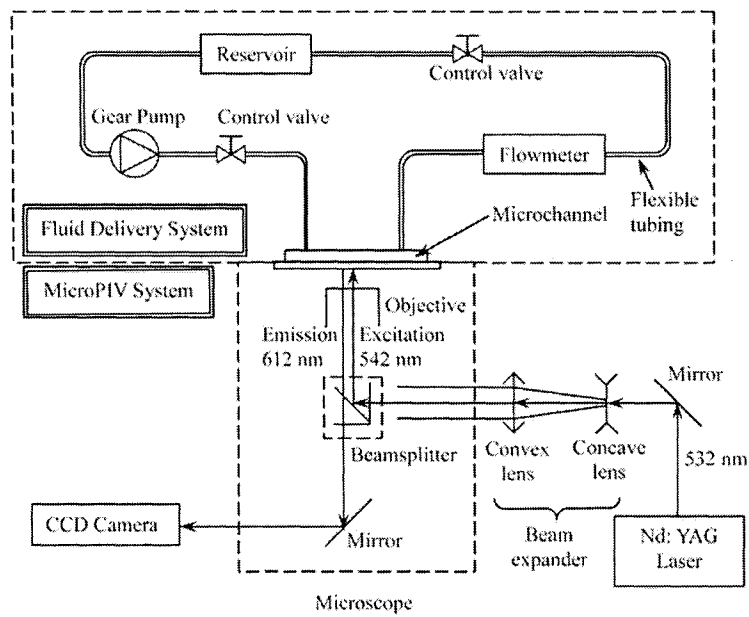


Figure 3.2 Schematic of experimental setup

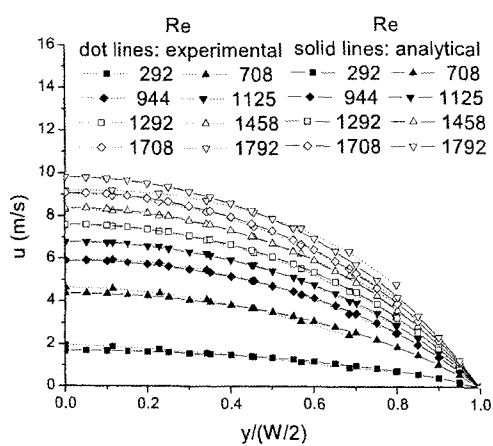
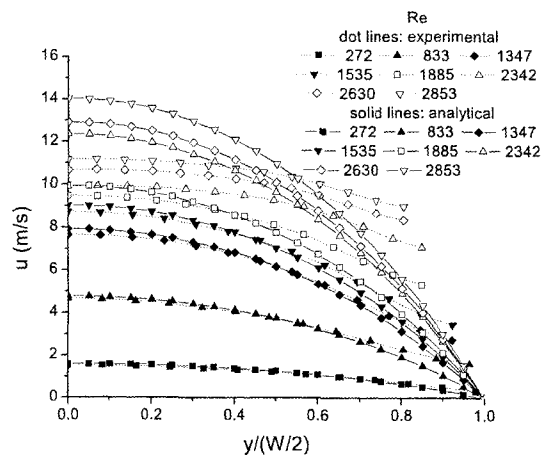
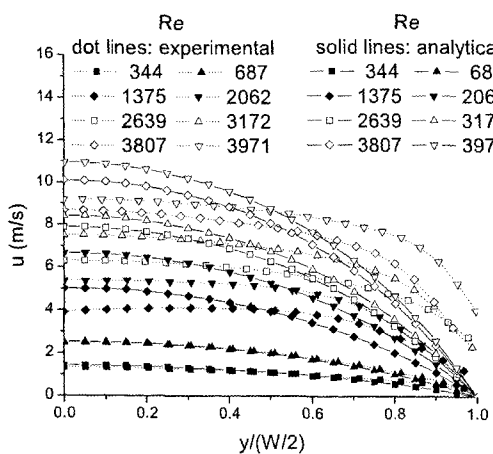
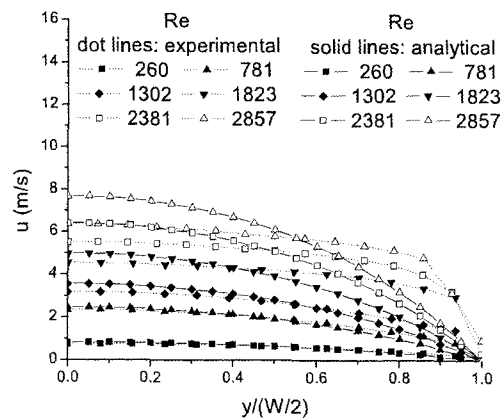
(a) 200 μm (b) 320 μm (c) 480 μm (d) 640 μm

Figure 3.3 Mean streamwise velocity profiles

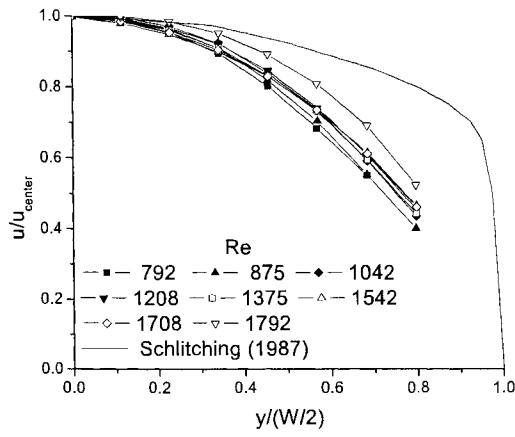
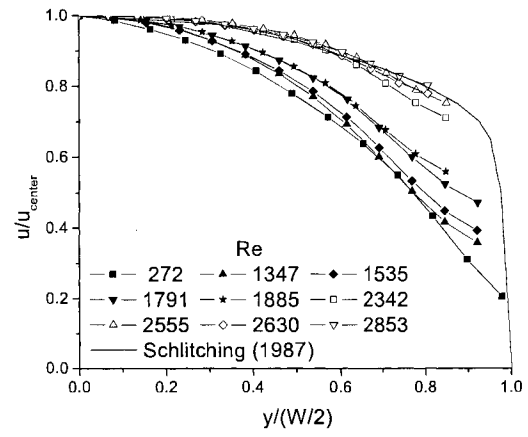
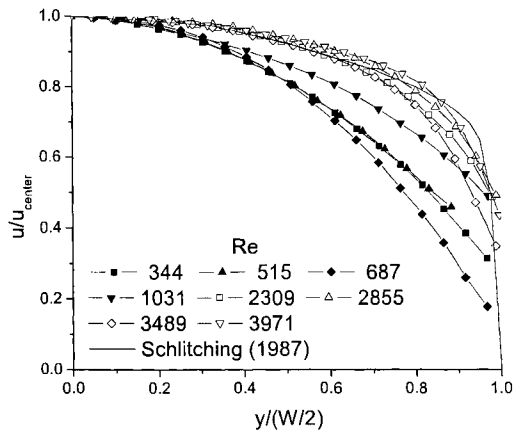
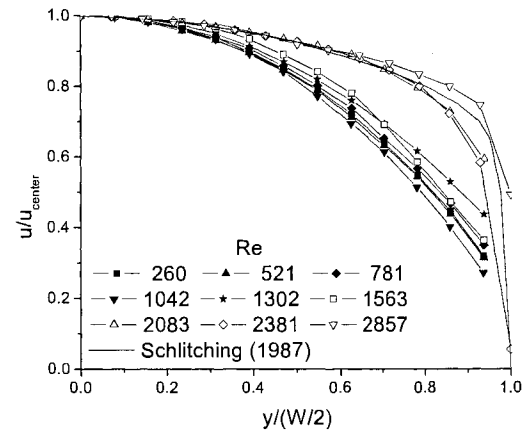
(a) $200 \mu\text{m}$ (b) $320 \mu\text{m}$ (c) $480 \mu\text{m}$ (d) $640 \mu\text{m}$

Figure 3.4 Normalized mean streamwise velocity profiles

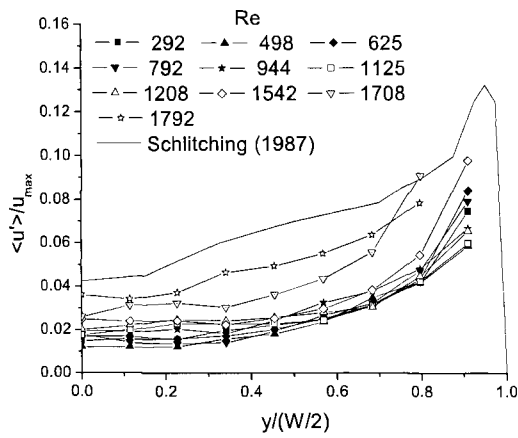
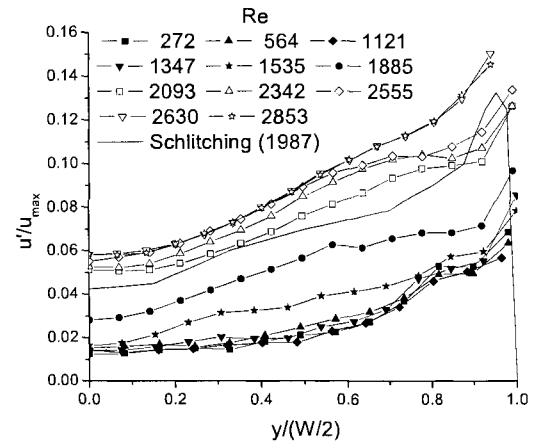
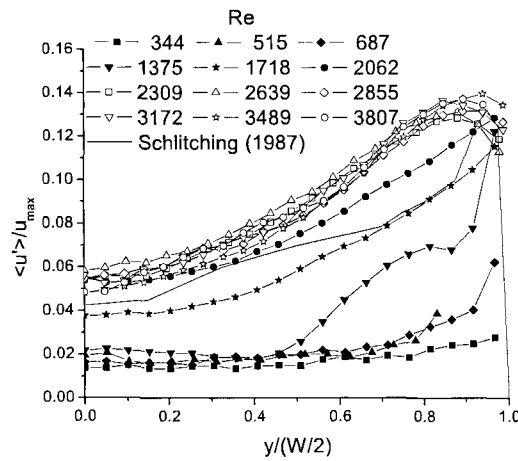
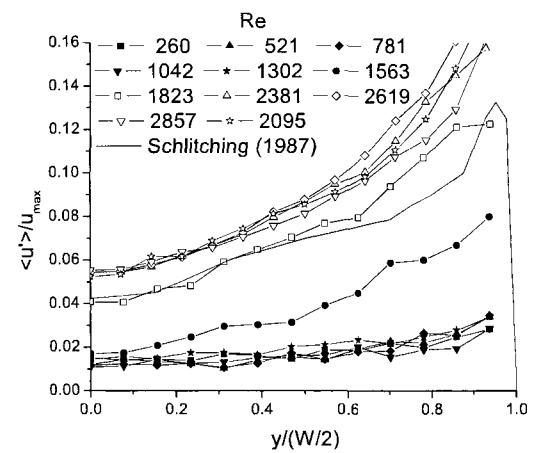
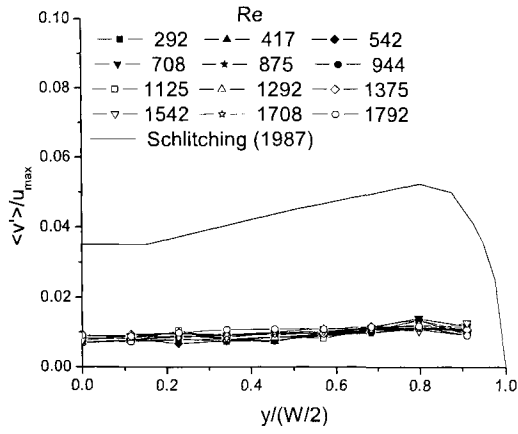
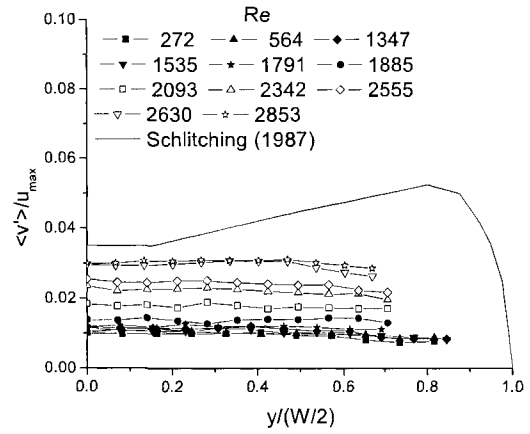
(a) 200 μm (b) 320 μm (c) 480 μm (d) 640 μm

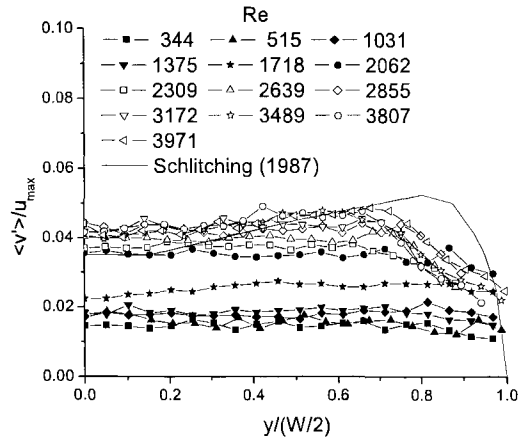
Figure 3.5 Streamwise velocity fluctuations



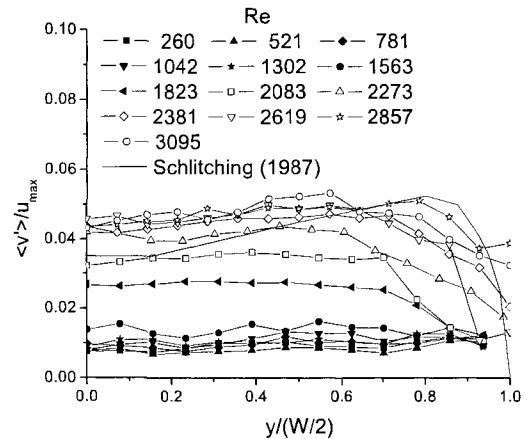
(a) 200 μm



(b) 320 μm



(c) 480 μm



(d) 640 μm

Figure 3.6 Transverse velocity fluctuations

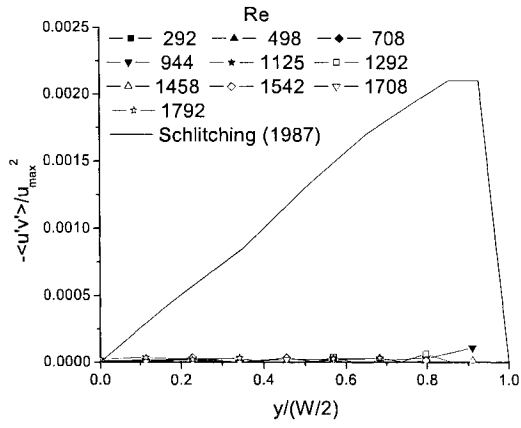
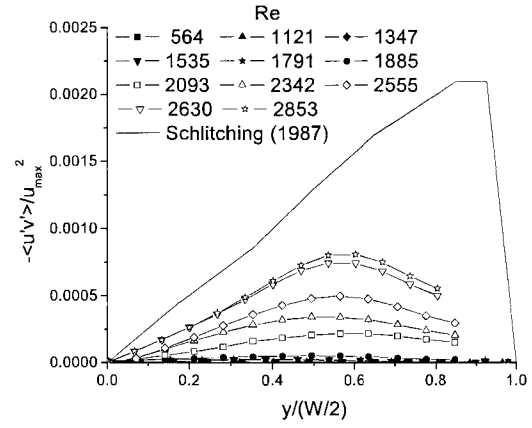
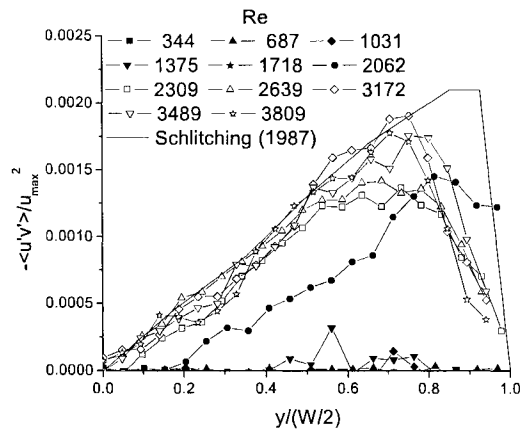
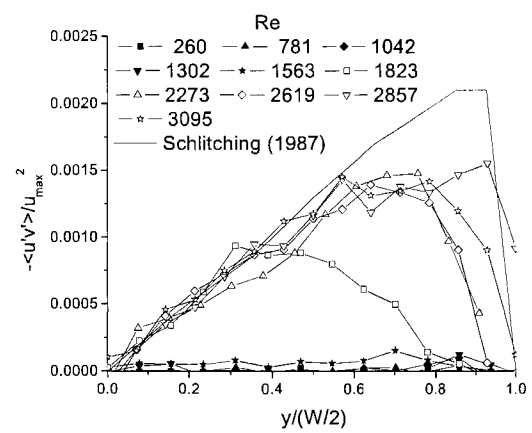
(a) 200 μm (b) 320 μm (c) 480 μm (d) 640 μm

Figure 3.7 Reynolds shear stress

CHAPTER 4 MICROPIV MEASUREMENT OF TURBULENT FLOW IN RECTANGULAR MICROCHANNELS WITH VARYING ASPECT RATIOS

A paper accepted by *Journal of Fluids Engineering*

H. Li and M. G. Olsen

Abstract

Microscopic particle image velocimetry (microPIV) was used to measure velocities in rectangular microchannels with aspect ratios ranging from 0.97 to 5.69 for $200 < Re < 3267$. Mean velocity profiles, velocity fluctuations, and Reynolds stresses were determined from the microPIV data. Transition to turbulence was observed at $Re = 1765 - 2315$ for the five aspect ratios studied, agreeing very well with both recent microscale experiments and macroscale duct flow and indicating no evidence of early transition for any of the aspect ratios studied. The onset of fully turbulent flow was observed at $Re = 2600 - 3200$.

For the fully turbulent flow, the $\langle u' \rangle / u_{max}$ and $\langle v' \rangle / u_{max}$ fluctuations at the channel centerline were 6% and 3-3.5% and generally agreed well with macroscale results. As aspect ratio increased, the $\langle u \rangle / u_{max}$ and $\langle u' \rangle / u_{max}$ profiles became flatter, with nearly uniform values extending for some distance from the centerline of the channel. This region of uniform $\langle u \rangle / u_{max}$ and $\langle u' \rangle / u_{max}$ became larger with increasing aspect ratio. The Reynolds shear stress for fully turbulent flow also displayed a strong dependence on aspect ratio. For the $W/H = 0.97$ microchannel, $\langle u'v' \rangle / u_{max}^2$ steadily increased in value

moving from the centerline to the wall, but for the higher aspect ratio microchannels, $\langle u'v' \rangle / u_{max}^2$ remained close to zero in the center region of the microchannel before increasing in value at locations close to the wall, and this region of near zero $\langle u'v' \rangle / u_{max}^2$ became larger with increasing aspect ratio. This behavior in the Reynolds shear stress is due to the region of uniform velocity, and hence, small mean shear, near the channel centerline of the high aspect ratio microchannels.

Introduction

The recent rapid development of microfluidic microelectromechanical systems (MEMS) and their importance in such applications as microscale cooling [Tuckerman and Pease (1981)], drug delivery, biotechnical analysis, and telecommunication technologies [Henning (1998); Lipman (1999)] has resulted in a growing interest in understanding flow behavior in microchannels. In microscale cooling applications, microchannels with high aspect ratio are often used because their high surface-area-to-volume ratio makes them more efficient in high heat flux applications than microchannels with square or circular cross sections. However, this important microchannel flow geometry has not received nearly the attention that has been given to circular or square cross sectional microchannels.

While the body of work on high aspect ratio microchannels is not as large as for square or circular microchannels, there do exist in the literature some interesting results from previous studies. For example, some studies of flow in high aspect ratio microchannels have reported early transition to turbulent flow compared to macroscale flow and found that the transitional Reynolds number in microchannels was dependent on the aspect ratio. Peng and Peterson (1996a,b) performed single-phase forced convective heat transfer and fluid flow experiments with water flowing through rectangular stainless steel microchannels with heights of 0.2 and 0.3 mm and widths ranging from 0.1 to 0.4 mm.

Although the heat transfer experiments showed negligible effect of aspect ratio H/W due to the small hydraulic radius comparable to the sublayer thickness, the laminar and turbulent flow conditions were still found dependent the geometric parameters including hydraulic diameter D_h and aspect ratio H/W . Likewise, Mo et al. (2004) investigated forced convection of low temperature (80 – 150 K) nitrogen gas flowing through rectangular channels with consistent width of 20 mm and hydraulic diameters ranging from 0.513 – 1.814 mm, corresponding to aspect ratios of 0.013 – 0.048. The laminar-turbulent transition of Nu showed dependence on channel depth, and an optimum channel aspect ratio for maximizing heat transfer was determined (such behavior was also mentioned in Peng’s work [Peng and Peterson (1996a)]). Pfund et al. (2000) detected the turbulent transition by measuring friction factor and performing flow visualization. The rectangular channels in their study had a constant width of 1 cm and varying mean depths of 521, 263, and 128 μm . Although the transitional Reynolds numbers were much larger than the values of 200 – 700 which were reported in previous works, they observed transition occurring at Reynolds numbers lower than the critical Reynolds number for macroscale ducts, and found transitional Reynolds number decreasing with decreasing channel depth.

Although researchers have offered numerous explanations for early transition and deviation from macroscale correlations for friction factor and Nusselt number in microchannel flow, (for example, the relatively high surface roughness [Wu and Little (1983, 1984); Qu et al. (2000); Guo and Li (2003a,b); Sabry (2000); Toh et al. (2002); Tunc and Bayazitoglu (2002); Koo and Kleinstreuer (2003)], flow compressibility induced by surface friction [Chen and Kuo (2004)], surface electrostatic charges, axial heat conduction in channel walls [Guo and Li (2003a,b)], etc.), these explanations fail to explain why other similar studies with the comparable measurement error and surface roughness have reported good agreement between experimental results and theoretical macroscale predictions and reported negligible aspect ratio effects. For example, Hegab et al. (2002,

2001) examined the effects of Reynolds number, relative roughness, and channel aspect ratio by determining f and Nu from measured temperatures, flow rates, and pressure drops for single-phase R134a flow in aluminum microchannels with hydraulic diameters ranging from approximately 112 to 210 μm and aspect ratios from 1.0 to 1.5. The experimental results indicated the onset of transition from laminar to turbulent flow occurring between $Re = 2000$ and 4000. Wu and Cheng (2003) measured the friction factor of deionized water flow in silicon microchannels of trapezoidal cross-section with consistent depth and different widths. The experimental data was found to be in good agreement with existing analytical solution for an incompressible, fully developed, laminar flow under no-slip boundary condition. Also, the transition from laminar to turbulent flow was observed at $Re = 1500 - 2000$. Baviere et al. (2004) experimentally studied friction coefficients as a function of Reynolds number by measuring pressure drop in microchannels with constant width of 25 μm and depths of 100, 200, and 300 μm . Data were collected for $Re = 0.01 - 8000$. The results showed good agreement between the experimental data and macroscale flow predictions. The transitional Re was found around 2700 – 3100 for smooth channels, and generally in good agreement with that of macroscale flow.

It is important to note that the previously mentioned experiments were performed using traditional macroscale pressure drop and temperature measurements which can be quite challenging to apply to microscale flows. In these studies, the behavior of the measured friction factors and/or Nusselt numbers with Reynolds number was used as the criterion to determine the presence of laminar, transitional, or fully turbulent flow. The conflicting results of previous research reflects the potential drawbacks of traditional measurement techniques. Recently, researchers have attempted to clarify the sometimes contradictory results on microfluidic flow transition using a relatively new experimental technique — microscopic particle image velocimetry (microPIV) [Santiago et al. (1998); Meinhart et al. (1999, 2000); Olsen and Adrian (2000a,b); Devasenathipathy et al. (2003)]. Since its development as a non-invasive measurement technique for

microscale flow systems, microPIV has been widely used in researching many different microscale flows [Stone et al. (2002); Klank et al. (2002); Kim et al. (2002); Son et al. (2002)].

MicroPIV has also been used to study transition and turbulence in microchannel flows. Zeighami et al. (2000) performed an experimental investigation on transition in a silicon microchannel with dimensions of $150 \mu\text{m} \times 100 \mu\text{m} \times 1 \text{ cm}$. The repeatability of the velocity data and the motion of seed particles perpendicular to the measurement plane were taken as the criteria to distinguish laminar and turbulent flow. Using these criteria, slightly early transition at $Re = 1200 - 1600$ was suggested. However, in this study, the particle seed density was not sufficient for Reynolds stresses to be measured or for turbulent structures to be observed. Lee et al. (2002) studied flow up to $Re = 2900$ in a rectangular microchannel with an aspect ratio 2.65 and a hydraulic diameter of $380 \mu\text{m}$. In this work, the deviation of velocity profiles and a broadening of the microPIV cross-correlation signal peak with turbulence intensity was used to identify transition at $Re = 2900$. Sharp and Adrian (2004) performed a detailed set of pressure drop and microPIV experiments on transitional flow in round glass microtubes with diameters between 50 and $247 \mu\text{m}$ with working fluids of different polarities. In their microPIV experiments, the unsteady fluctuations of the centerline velocity were taken as indicators of the transition to turbulence. In the laminar region, centerline velocity fluctuations of around 1% (due to experimental noise) were observed. However, at higher Reynolds numbers, the centerline velocity fluctuations increased, and the first abrupt increase of the rms value of centerline velocity was taken as the onset of transitional flow. Using this definition, transition was observed between $1800 < Re < 2200$, and thus Sharp and Adrian concluded that the anomalous early transition observed by previous researchers was not occurring. Li et al. (2005); Li and Olsen (2005) performed microPIV experiments to study the effect of hydraulic diameter changes in transitional and turbulent flow through square PDMS microchannels with hydraulic diameters ranging from 200 to

640 μm . They were the first researchers to report Reynolds stress data in microchannel flows. Using the same definition of transition as Sharp and Adrian (2004), they found the onset of transition between $Re = 1800$ and 2000, in agreement with macroscale flow results.

In the present work microPIV has been used to obtain instantaneous velocity field data for flow through rectangular channels with approximately consistent hydraulic diameters of 320 μm and a range of aspect ratios from 0.97 to 5.69. The measured streamwise velocity profiles, streamwise and transversal velocity fluctuations, and Reynolds stresses are reported and used to determine both the onset of transition to turbulence and the characteristics of fully developed turbulent flow in microchannels of varying aspect ratios. The results are also compared with classical results for macroscale ducts.

Microchannel Fabrication

The straight microchannels used in the present experiments were fabricated using PDMS replica molding [Anderson et al. (2000); Jo et al. (2000)]. A brief summary of the fabrication process follows (greater detail of the fabrication process can be found in Li's work [Li et al. (2005); Li and Olsen (2005)]). Figure 4.1 presents the fabrication procedure graphically. The channel molds were made from patterned negative photoresist (SU-8 2100, MicroChem Corp., Newton, MA) on a silicon wafer (100 mm diameter, Montco Silicon Technologies, Inc, Spring City, PA). A coating of the photoresist was spun on the silicon wafer to a uniform thickness, and select regions of the coated wafer were exposed through a transparency film to ultraviolet light. The photoresist was then developed resulting in a mold of the microchannel geometry in relief. Polydimethylsiloxane (PDMS) elastomer (Sylgard(R) 184 Silicone Elastomer Kit, Dow Corning, Midland, MI) was then cast on the molds and baked. Finally, the two halves of the microchannel are plasma treated and bonded to form the complete microchannel.

Microchannels were fabricated with five different aspect ratios and with hydraulic diameters of approximately $320\ \mu\text{m}$. The different widths were controlled by varying the design drawings of transparencies, and the different depths were controlled by adjusting the amount of photoresist deposited on the wafer, the spinning speed of spin coater, the baking time, and the exposure time to UV light. Accurate determination of dimensions was essential to obtain reliable data. The optical measurement of the dimensions at various positions along the microchannels, accurate to within $\pm 10\ \mu\text{m}$, indicated variations in hydraulic diameter over the entire length of the microchannel of between 1.25% to 5%. The final length-averaged dimensions of the five different microchannel geometries are listed in Table 4.1.

The resulting microchannels were then tested for inner surface roughness using Dektak IIA surface profile measuring system (Veeco Instruments Inc., Santa Barbara, CA). Liner surface surface profiles were taken of the cast PDMS. These measurements were limited, as the profilometer stylus could only be used on the top and bottom surfaces of the channel. The arithmetic average roughness of the microchannels was calculated by the Dektak IIA software and was determined to be approximately 24 nm. This results in a relative roughness of $\epsilon_s/D_h \approx 0.000074$.

Experimental Methodology

Experimental Setup

The experimental system, schematically shown in Fig. 4.2, consists of two sub-systems: (i) the flow delivery system; and (ii) the microPIV system. The flow was driven by a micro gear pump and pump head (115 VAC console digital dispensing drive and 0.084 ml/rev suction shoe gear pump head, Cole-Parmer Instrument Co., Vernon Hills, IL) that provides constant flow rates with accuracy of $\pm 0.3\%$. The working fluid was deionized water. Flow from the gear pump passes through the microchannel, then

through a digital flowmeter (0–100 mL/min volumetric water flow meter, Cole-Parmer Instrument Co., Vernon Hills, IL), and finally through a fluid reservoir before returning to the gear pump to begin a second cycle. The flowmeter contained a thermocouple so fluid temperature could be carefully monitored during each run. The purpose of the fluid reservoir was to increase the thermal mass of the fluid in the system, so that viscous dissipation did not result in any temperature change of the working fluid during the experimental runs.

The microPIV system is shown in the lower portion of Fig. 4.2. A double pulsed Nd:YAG laser (Continuum, Santa Clara, CA), attenuated to 3 mJ/pulse with a wavelength of 532 nm, was expanded and directed into an aperture in the rear of an inverted biological microscope [Nikon model T-300 Inverted Microscope]. The 820 nm diameter fluorescent seed particles (Duke Scientific Co., Palo Alto, CA) were excited by the laser light and emitted light at a peak emission wavelength of 612 nm. The excited light, filtered by a beamsplitter to remove illuminating and background light, was then imaged through the microscope using an objective lens with a magnification of 20X and a numerical aperture of 0.45. A LaVision Flowmaster 3 camera (LaVision Inc., Ypsilanti, MI) was used to capture the PIV image pairs for cross-correlation analysis.

The concentration of the fluorescent particle solution was prepared such that a sufficient number of seed particles fell within depth of correlation [Olsen and Adrian (2000b); Bourdon et al. (2004)] of each interrogation region that erroneous vector measurements were minimized. In the present experiments, the 20X 0.45 NA microscope objective yields a depth of correlation of 8.3 μm . Using interrogation windows measuring 28 μm square and overlapping each interrogation region by 50% yielded a vector spacing of 14 μm . Achieving this spatial resolution required a volumetric particle concentration of approximately 0.057%. This volume fraction of seed particles was small enough that any two-phase effects are negligible, and the working fluid could be considered a single-phase fluid.

The experiments were performed at various flow rates corresponding to Reynolds numbers ranging from 200 to 3257. For each set of experiments, sufficient time was allowed to pass after starting the micro gear pump to allow the flow to reach steady state. For smaller flow rates, it took a longer time to reach a steady state compared to higher flow rates. A multi-pass interrogation scheme with decreasingly smaller window sizes was used in the computation of the vector fields to reach the final 32 x 32 pixel interrogation windows. The only post-processing performed on the vector fields was the removal of bad vectors. No smoothing of vector fields was performed. The number of velocity fields collected for each Reynolds number ranged from 600 for the lowest, laminar Reynolds numbers to 2000 for the transitional and turbulent Reynolds numbers.

Measurement Error

There are two sources of measurement errors in the microPIV experiments: errors introduced by random motion of the seed particles due to Brownian motion, and errors implicit in the interrogation of the PIV images. The significance of Brownian motion in the microPIV measurements can be determined by calculating the Brownian motion parameter [Olsen and Adrian (2000a)], defined as

$$\frac{d_e^2}{d_e^2 + 8M^2\beta^2 D\Delta t} \quad (4.1)$$

where $D = KT/(6\pi\mu d_p)$, β^2 is a constant equal to 3.67, and d_e is the image diameter for a particle in the object plane [Adrian and Yao (1983)].

$$d_e = \sqrt{M^2 d_p^2 + d_s^2} \quad (4.2)$$

where $d_s = 2.44(M + 1)\lambda f^\#$ is the diameter of the diffraction-limited point spread function in the image plane, M is the magnification of the microscopic objective, d_p is

the particle diameter, λ is emitted light wavelength from particles, $f^\#$ is focal number of objective.

For values of the Brownian motion parameter close to unity, Brownian motion has a negligible effect on the measured velocity. For the AR5 microchannel at $Re = 525$, the Brownian motion coefficient is equal to 0.9998, indicating that Brownian motion effects are indeed negligible. For the smaller microchannels, or at higher Reynolds numbers in the AR5 microchannel, the Brownian motion effect is even smaller, due to the smaller Δt required for these measurements. Note that the fact that Brownian motion is negligible should not be surprising, given the short Δt required for each of the measurements (on the order of 1 microsecond).

The experimental error due to interrogation of the PIV images can be estimated by assuming that measured particle displacements are accurate to within approximately 1/10th of a seed particle image diameter [Prasad et al. (1992)]. From Eqn. [4.2], $d_e = 38 \mu\text{m}$, yielding an effective particle diameter when projecting back into flow coordinates of $1.9 \mu\text{m}$, meaning that the measured particle displacement in the microPIV experiments should be accurate to within $0.19 \mu\text{m}$. For the present experiments, the particles travel approximately $8 \mu\text{m}$ between laser pulses, resulting in an experimental uncertainty of approximately 2.3%.

The relative unimportance of the error due to Brownian motion can also be demonstrated by comparing the particle displacement due to particle diffusion with the uncertainty in determining particle displacement. The distance that a particle is expected to diffuse due to Brownian motion can be found using

$$s = \sqrt{2D\Delta t} \quad (4.3)$$

For $Re = 3000$ in the AR1 microchannel, the rms particle displacement due to Brownian motion is $0.001 \mu\text{m}$, which is only 0.5% of the experimental error. Thus, the

effects of Brownian motion can be safely neglected.

The microPIV images were obtained at locations far enough downstream of the microchannel entrance to ensure fully developed flow and avoid any entrance length effects [Lee et al. (2002)]. This was verified by taking measurements at different downstream locations and comparing the mean velocity profiles. In all cases, velocity fields were measured along the microchannel midplane, which was located by finding the maximum velocity peaks in laminar flow.

Results and Discussion

The ensemble-averaged streamwise velocity profiles in the different aspect ratio microchannels for various Reynolds numbers are presented in Fig. 4.3 together with the corresponding fully developed laminar analytical solutions for flow in a rectangular duct White (1991). The transverse coordinate has been normalized by $1/2$ of the width of the microchannel, with 0 corresponding to the microchannel centerline and 1 corresponding to the microchannel wall. For the AR1 microchannel ($W/H = 0.97$), the comparison shows good agreement between the measured velocity and the laminar solution until $Re = 1535$. Deviation from the laminar profile becomes apparent at $Re = 1885$, where the experimental data become flatter than the parabolic laminar solution, with a lower peak value at the centerline and higher velocities close the wall. The measurements were repeated for the AR2, AR3, AR4, and AR5 microchannels ($W/H = 2.09, 3.05, 4.00,$ and 5.69 , respectively), and these data are shown in Figs. 4.3(b), 4.3(c), 4.3(d), and 4.3(e), respectively. For these aspect ratios, the Reynolds numbers at which deviation from the laminar solution is observed range from 1373 to 1837. While some of these results may suggest the onset of early transition, this is not necessarily true, since deviations in the measured mean velocity profile from the analytical laminar solution have been found to occur in both macroscale [Wyganski and Champagne (1973)] and microscale

[Sharp and Adrian (2004)] channel and duct flows before any other evidence of transition (such as increases in rms velocity fluctuations) is observed. As Reynolds number is further increased, the measured velocity near the channel centerline deviates further from the laminar prediction and becomes smaller, while the velocity near the channel walls becomes greater, and the measured velocity profiles begin to resemble those of fully turbulent flow.

The changing shape of the mean velocity profiles with increasing Reynolds number is more distinctive in Fig. 4.4, where the mean velocity profiles are normalized by the centerline velocity. Figure 4.4 also shows the significant variation of velocity profiles from laminar flow to fully turbulent flow. At low Reynolds number, the velocity profiles are grouped together near the analytical laminar solution. As Reynolds number increases, the velocity profiles begin to deviate from the laminar solution, and the center region where a uniform velocity exists grows wider. At the highest Reynolds numbers studied, the velocity profiles become grouped again, suggesting that the microchannel flow is reaching a fully turbulent state. It was not possible to achieve the same maximum Reynolds number for all of the geometries investigated due to constraints of the fabrication process. For example, in the AR5 microchannel experiments, efforts were made to reach Reynolds numbers above 2352, however, at higher Reynolds numbers this microchannel catastrophically failed due to the high pressure resulting from the small aspect ratio of this configuration.

In order to quantify and characterize the turbulence in the microchannels, velocity fluctuations and Reynolds shear stresses were calculated from the microPIV data. Figures 4.5, 4.6, and 4.7 show the dimensionless profiles of $\langle u' \rangle / u_{max}$, $\langle v' \rangle / u_{max}$, and $\langle u'v' \rangle / u_{max}^2$, respectively for each of the different aspect ratio microchannels as a function of Reynolds number. For all the microchannels, the measured centerline values of $\langle u' \rangle / u_{max}$ exhibit a band of overlapped fluctuation values around 1.5% at Reynolds numbers lower than $Re = 1500$, as shown in Fig. 4.5. The measured fluctuations at

these low Reynolds numbers are not evidence of turbulence, but are instead due to the measurement uncertainty in the microPIV experiments.

In their microPIV experiments in microtubes, Sharp and Adrian (2004) defined transition to turbulence based on a significant increase in the measured centerline streamwise velocity fluctuations. Using this definition for transition in the present experiments, jumps in the streamwise velocity fluctuations are observed at $Re = 1885, 2315, 1765, 1867,$ and 1837 for the AR1, AR2, AR3, AR4, and AR5 microchannels, respectively. These measured transitional Reynolds numbers of $1765 - 2315$ for rectangular microchannels agree very well with the transitional Reynolds numbers of $1800 - 2000$ that Sharp and Adrian reported for round microtubes. Since transition in macroscale pipe and duct flows typically occurs at $Re = 1800-2300$, no evidence of early transition was observed in the present study, just as Sharp and Adrian observed no evidence of early transition in their round microtube experiments. Nearly identical transitional Reynolds numbers are obtained if transition is instead defined by a jump in the centerline transverse velocity fluctuations. Using this definition, transition is observed at $Re = 1885, 2315, 1765, 1867,$ and 1837 for the AR1, AR2, AR3, AR4, and AR5 microchannels.

As Reynolds number is increased above transition, increases in both the streamwise and transverse velocity fluctuations are observed. Eventually, the fluctuations will no longer appear to increase with increasing Reynolds number, and this behavior, along with the mean velocity profiles approaching that of fully turbulent flow (Fig. 4.4) is indicative of a fully turbulent state being reached (note that even in fully turbulent duct flow, the mean velocity and velocity fluctuation profiles will continue to show a *weak* dependence on Reynolds number, but over the small range of Reynolds numbers investigated in the present study, the fully turbulent results should appear to overlap). Both the $\langle u' \rangle / u_{max}$ and $\langle v' \rangle / u_{max}$ velocity fluctuations consistently overlap for the AR1, AR2, AR3, AR4, and AR5 microchannels at Reynolds numbers somewhere in the range $2400 < Re < 2700$. Coupling these results with the mean velocity profiles shown in Fig. 4.4 suggests

fully turbulent flow being reached in the approximate range of $2600 < Re < 3000$.

The measured fully turbulent values for $\langle u' \rangle / u_{max}$ presented in Fig. 4.5 are slightly higher than classical macroscale results for turbulent square duct flow [Schlichting (1987)] and high aspect ratio duct flow [Tracy (1965)], although the difference is well within the measurement uncertainty of the present experiments. In general, the values for all cases are remarkably consistent, with measured fluctuations of around 6% at the centerline of the microchannel and higher values occurring moving from the centerline to the wall. Note that some of the increase in measured velocity fluctuations close to the walls of the microchannel may be due to an increase in measurement uncertainty near the walls. The measurement uncertainty is higher near the walls because of smaller particle displacements between PIV images due to lower velocities near the walls. For example, if a near wall location has a velocity that is half of centerline velocity, the measurement uncertainty is then doubled at the near wall location.

The measured fully turbulent values of $\langle v' \rangle / u_{max}$ shown in Fig. 4.6 are also consistent for the various microchannel geometries investigated. For each of the aspect ratios studied, $\langle v' \rangle / u_{max}$ at the centerline is between 3% and 3.5% and shows little variation with transverse location. As with the $\langle u' \rangle / u_{max}$ results, the measured $\langle v' \rangle / u_{max}$ fluctuations for Reynolds numbers in the laminar regime are due to measurement uncertainty and not the presence of turbulent structures.

The effect of aspect ratio on the turbulence characteristics can be observed in Figs. 4.3, 4.4, 4.5, and 4.6 by comparing the fully turbulent values of mean velocity and velocity fluctuations for microchannels with different aspect ratios. A close look at the streamwise velocity profiles in Figs. 4.3(a) through 4.3(e) reveals that as aspect ratio increases, the center region of fully turbulent velocity profiles becomes flatter with a wider uniform distribution of streamwise velocity at the center region. This can be attributed to the diminishing effect that the two side walls in the transverse direction have on the flow relative to the top and bottom walls of the microchannel with increasing aspect ra-

tio. Increasing the aspect ratio to the limiting case of $W/H \rightarrow \infty$, the effect of the side walls would become infinitesimally small, and the flow would approach two-dimensional flow between two infinite parallel plates, in which case the streamwise velocity would be uniform in the transverse direction. The variation of the distribution of fully turbulent velocity fluctuations $\langle u' \rangle / u_{max}$ and $\langle v' \rangle / u_{max}$ in Figs. 4.5 and 4.6 also display a similar aspect ratio effect. The velocity fluctuations become uniform across nearly 80% of the microchannel width as aspect ratio increases, and only show variations from the centerline fluctuations close to the side walls. This is because as the aspect ratio increases, the shear stresses induced by the two side walls becomes much smaller than the stresses induced by the top and bottom walls.

The aspect ratio effect is even more pronounced in the data for Reynolds shear stress, $\langle u'v' \rangle / u_{max}^2$, presented in Fig. 4.7 for the five microchannel geometries studied. In the laminar flow regime, $\langle u'v' \rangle / u_{max}^2$ is very close to zero, as expected, since any Reynolds stress measured for laminar flow is purely an artifact of the measurement uncertainty. As the flow transitions to turbulence, $\langle u'v' \rangle / u_{max}^2$ increases and eventually reaches the fully turbulent value. For the AR1 microchannel, the fully turbulent $\langle u'v' \rangle / u_{max}^2$ is zero at the centerline of the channel (as it must be due to flow symmetry), and steadily increases in value moving from the centerline to the wall (the shear stress must be zero at the wall due to the no slip condition, but the measurements do not extend close enough to the wall to see this behavior). For the higher aspect ratio microchannels, the Reynolds shear stress is also zero along the centerline of the microchannel, but instead of steadily increasing as one moves toward the wall, $\langle u'v' \rangle / u_{max}^2$ remains close to zero over some distance in center region of the microchannel before increasing in value at locations close to the wall. This region of near zero Reynolds shear stress becomes larger with increasing aspect ratio. This behavior in the Reynolds shear stress is due to the region of uniform velocity near the channel centerline in the low aspect ratio microchannels. From Prandtl's mixing length theory, turbulent shear stress is dependent on gradients in the

mean velocity field. In regions of nearly uniform mean velocity, the velocity gradients are small and thus the turbulent stresses are close to zero. Since the region of uniform mean velocity near the channel centerline grows with increasing aspect ratio, the region of near zero $\langle u'v' \rangle / u_{max}^2$ also grows. Closer to the walls of the channels, the velocity gradient is strong, thus accounting for the increase in Reynolds shear stress observed in Fig. 4.7 near the walls.

Summary and Conclusions

Microscopic particle image velocimetry was used to measure instantaneous velocity fields in rectangular microchannels with aspect ratios ranging from 0.97 to 5.69 for Reynolds numbers from 200 to 3267. Mean velocity profiles, velocity fluctuations, and Reynolds stresses were determined from the microPIV data. With transition to turbulence defined by an increase in the measured centerline velocity fluctuations, transition was observed at Reynolds numbers ranging from 1765 - 2315 for the five aspect ratios studied. These data agree very well with the recent experiments of Sharp and Adrian (2004) in round microtubes and Li and Olsen (2005) in square microchannels in which transition was observed for Re between 1800 and 2000. The results are also in agreement with transitional Reynolds numbers for macroscale duct flow, and thus no evidence of early transition was observed for any of the aspect ratios studied. Fully turbulent flow was achieved in all of the microchannels studied except the AR5 microchannel ($W/H = 5.69$), which structurally failed before fully turbulent flow could be achieved. In the other four aspect ratios studied, the onset of fully turbulent flow was observed for Reynolds numbers ranging from 2600 to 3200.

For the fully turbulent flow, the measured $\langle u' \rangle / u_{max}$ and $\langle v' \rangle / u_{max}$ fluctuations at the channel centerline were consistently around 6% and 3-3.5% and generally agreed well with classical macroscale results for turbulent square duct flow [Schlichting (1987)] and

high aspect ratio duct flow [Tracy (1965)]. As aspect ratio increased, the measured mean streamwise velocity and streamwise velocity fluctuation profiles became flatter, with nearly uniform values extending for some distance from the centerline of the channel. This region of uniform $\langle u \rangle / u_{max}$ and $\langle u' \rangle / u_{max}$ became larger with increasing aspect ratio.

The Reynolds shear stress for fully turbulent flow also displayed a strong dependence on aspect ratio. In all cases studied, $\langle u'v' \rangle / u_{max}^2$ was zero at the channel centerline, as required by symmetry. For the AR1 microchannel ($W/H = 0.97$) $\langle u'v' \rangle / u_{max}^2$ steadily increased in value moving from the centerline to the wall, but for the higher aspect ratio microchannels, $\langle u'v' \rangle / u_{max}^2$ remained close to zero over some distance in center region of the microchannel before increasing in value at locations close to the wall, and this region of near zero $\langle u'v' \rangle / u_{max}^2$ became larger with increasing aspect ratio. This behavior in the Reynolds shear stress is due to the region of uniform velocity, and hence, small mean shear, near the channel centerline of the high aspect ratio microchannels.

Table 4.1 Geometric parameters of test microchannels with varying aspect ratios

Channel Name	W (μm)	H (μm)	D_h (μm)	Aspect Ratio (W/H)
AR1	320	330	325	0.97
AR2	480	230	311	2.09
AR3	640	210	316	3.05
AR4	800	200	320	4.00
AR5	1080	190	323	5.69

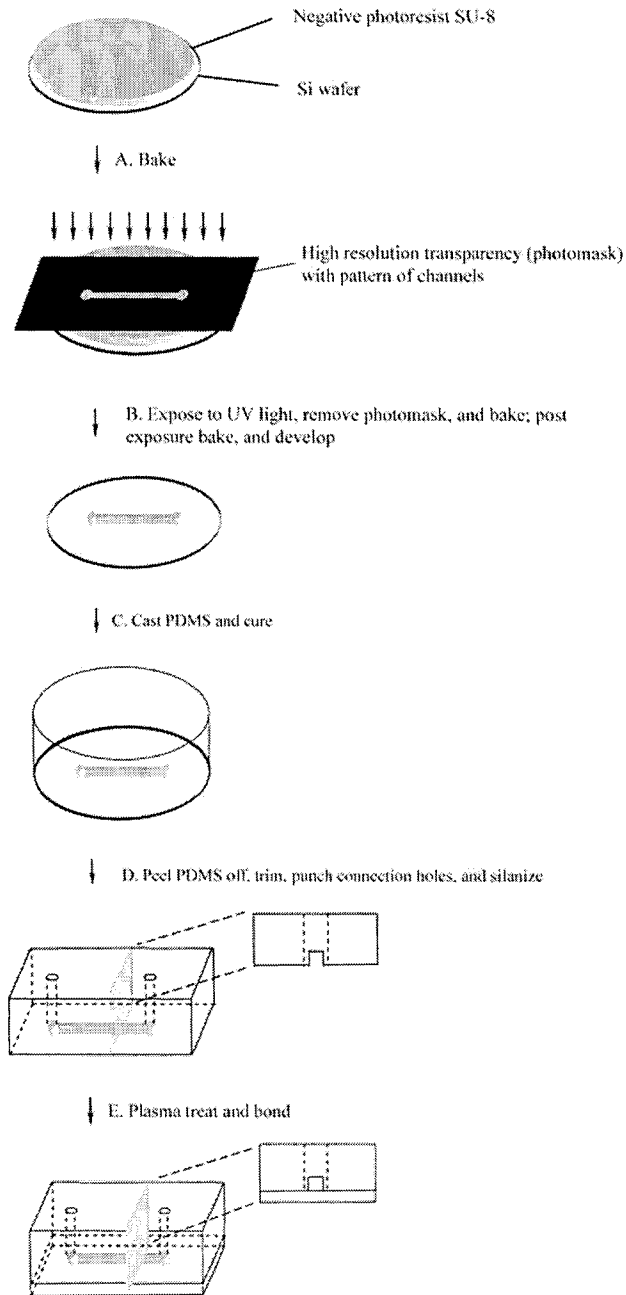


Figure 4.1 Summary of the microchannel fabrication technique

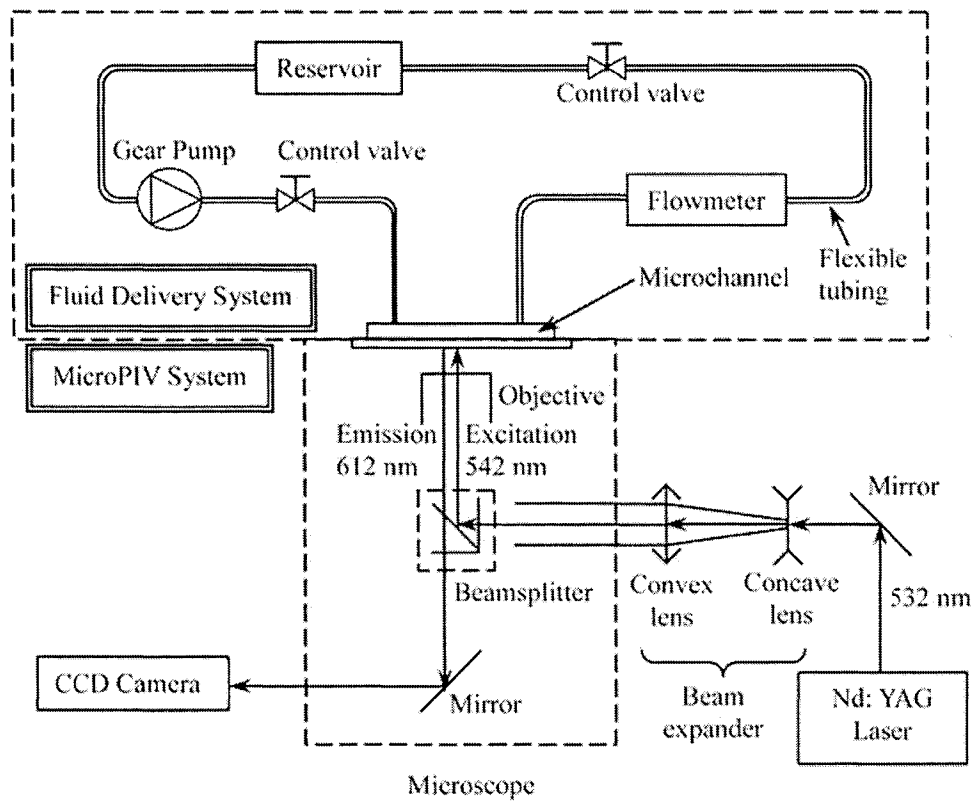
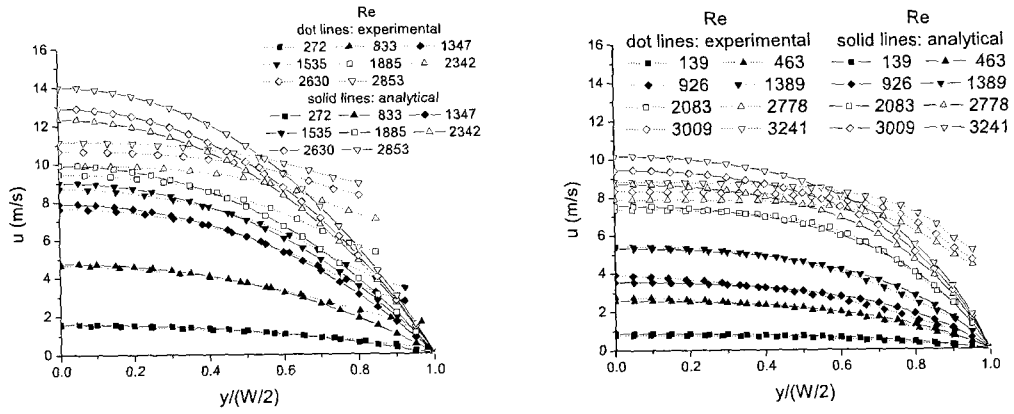
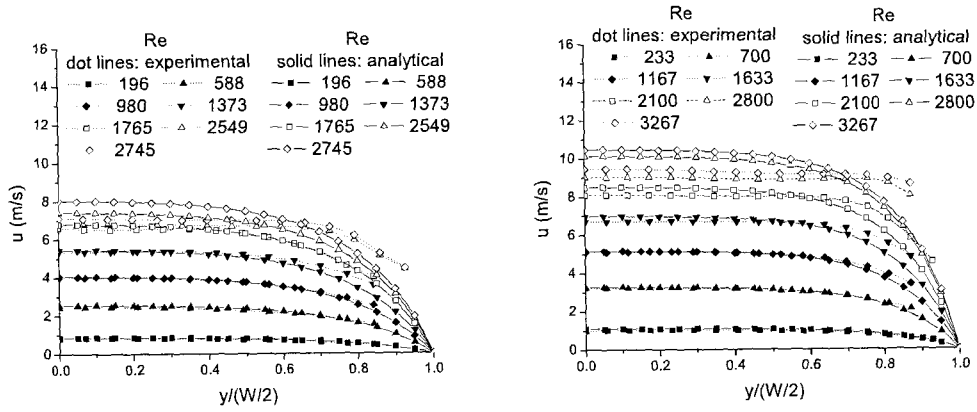


Figure 4.2 Schematic of experimental setup



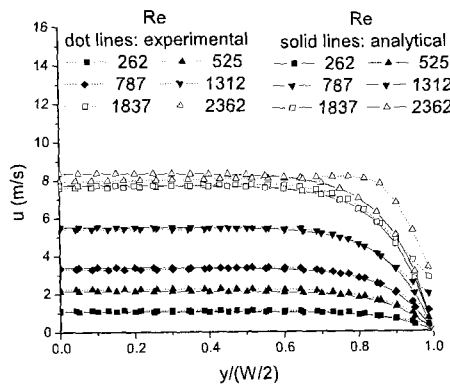
(a) AR1

(b) AR2



(c) AR3

(d) AR4



(e) AR5

Figure 4.3 Mean streamwise velocity profiles for five different aspect ratios as measured by microPIV

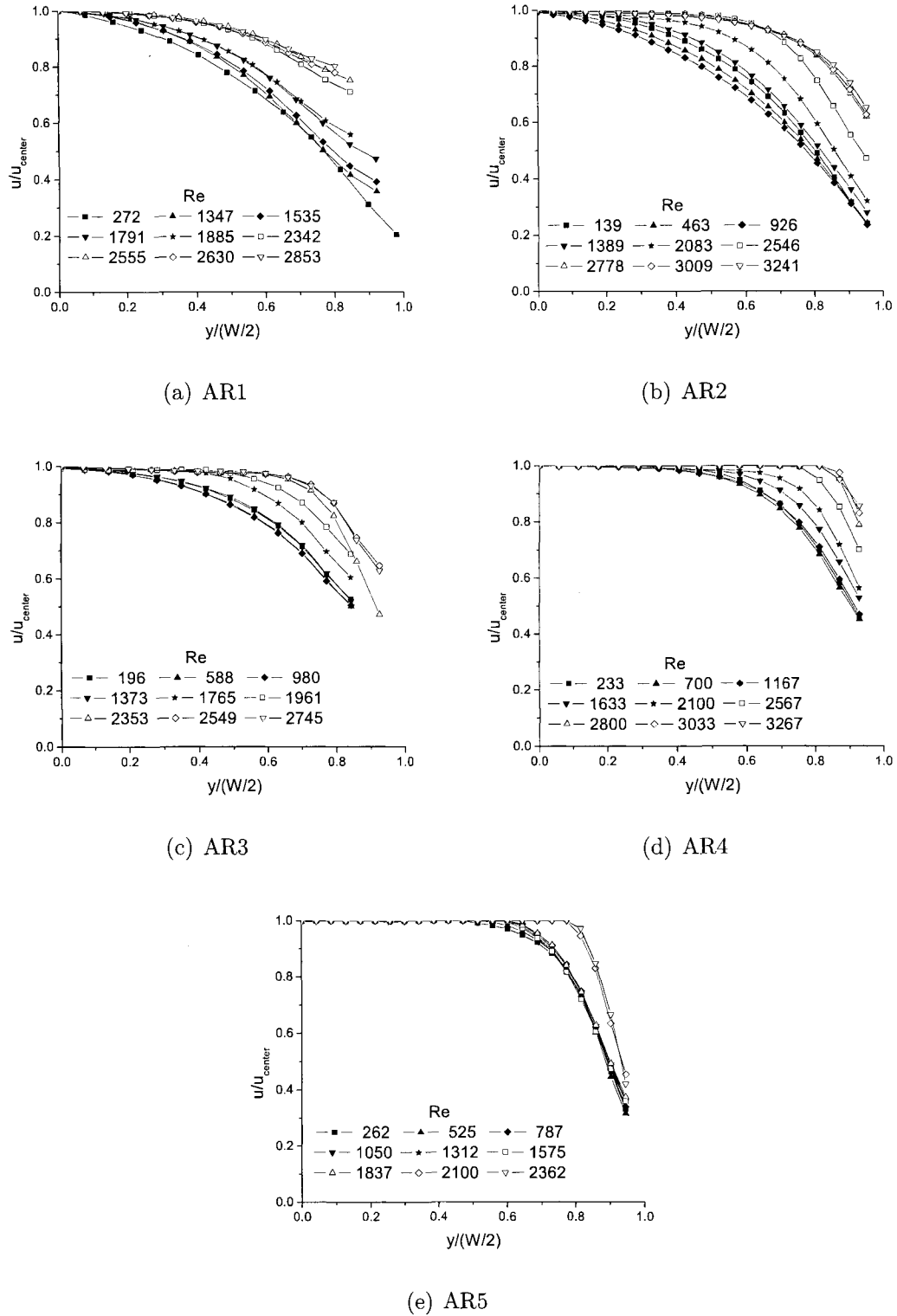


Figure 4.4 Normalized streamwise velocity profiles for five different aspect ratios as measured by microPIV

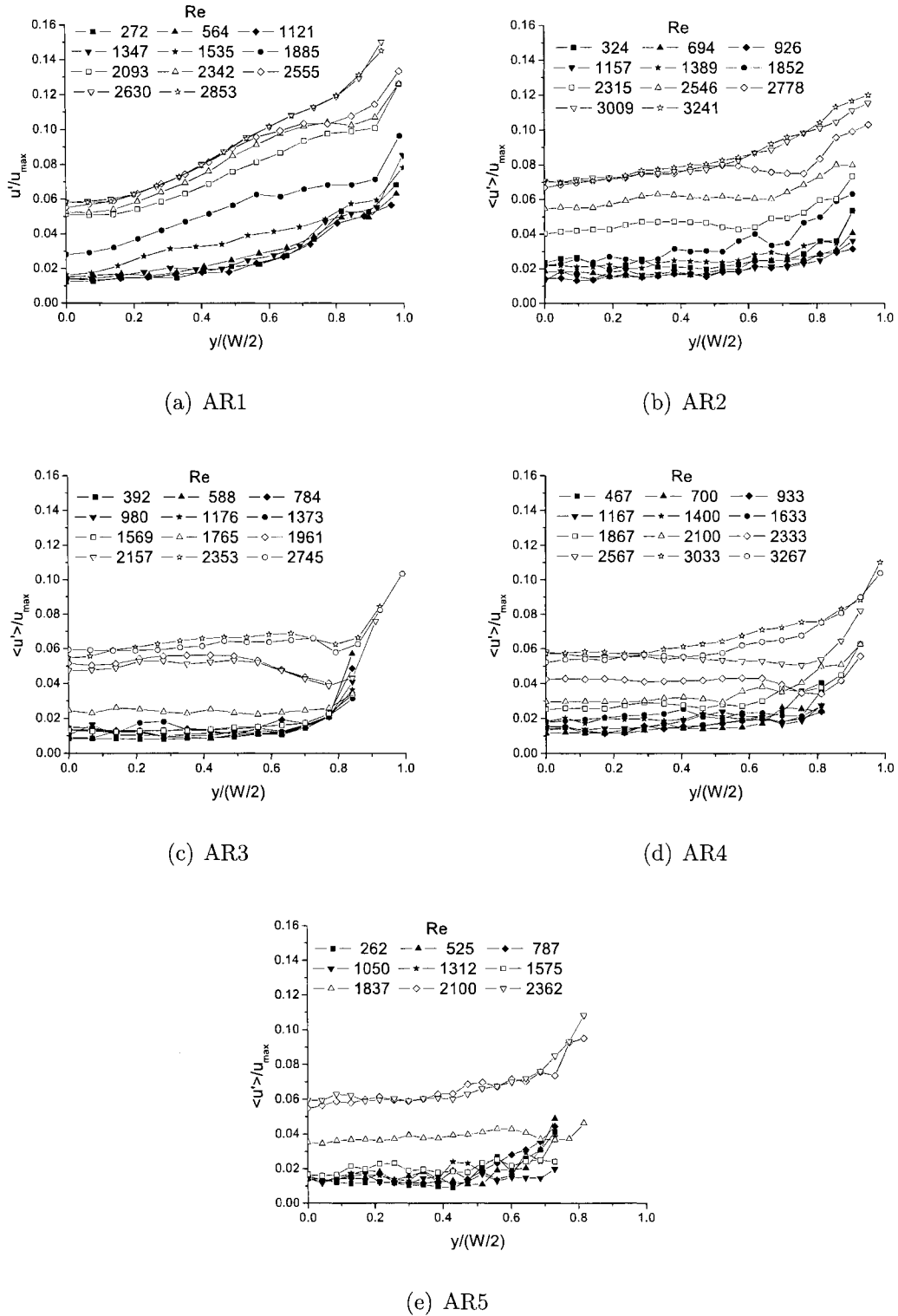


Figure 4.5 Streamwise velocity fluctuation profiles for five different aspect ratios as measured by microPIV

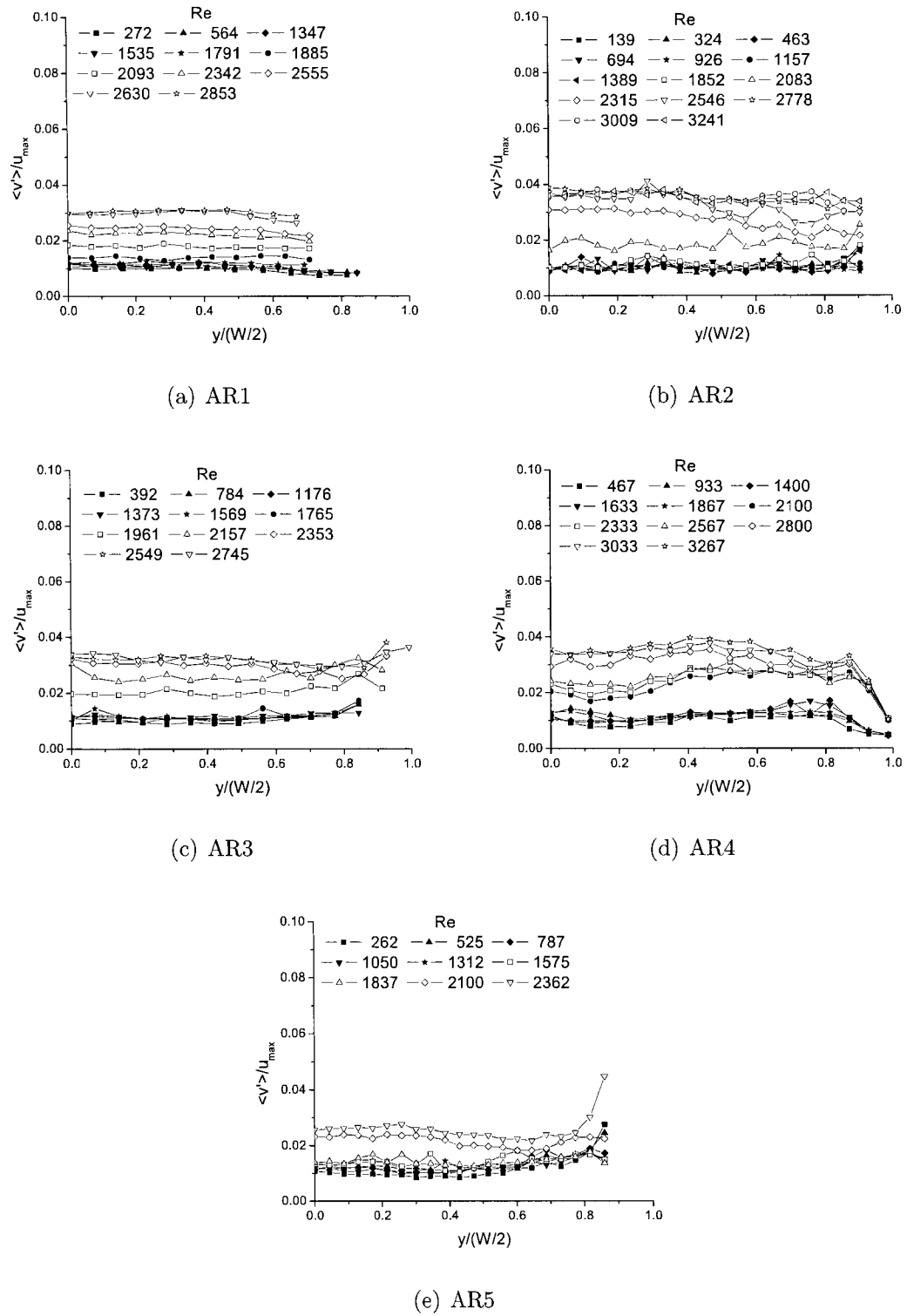


Figure 4.6 Transverse velocity fluctuation profiles for five different aspect ratios as measured by microPIV

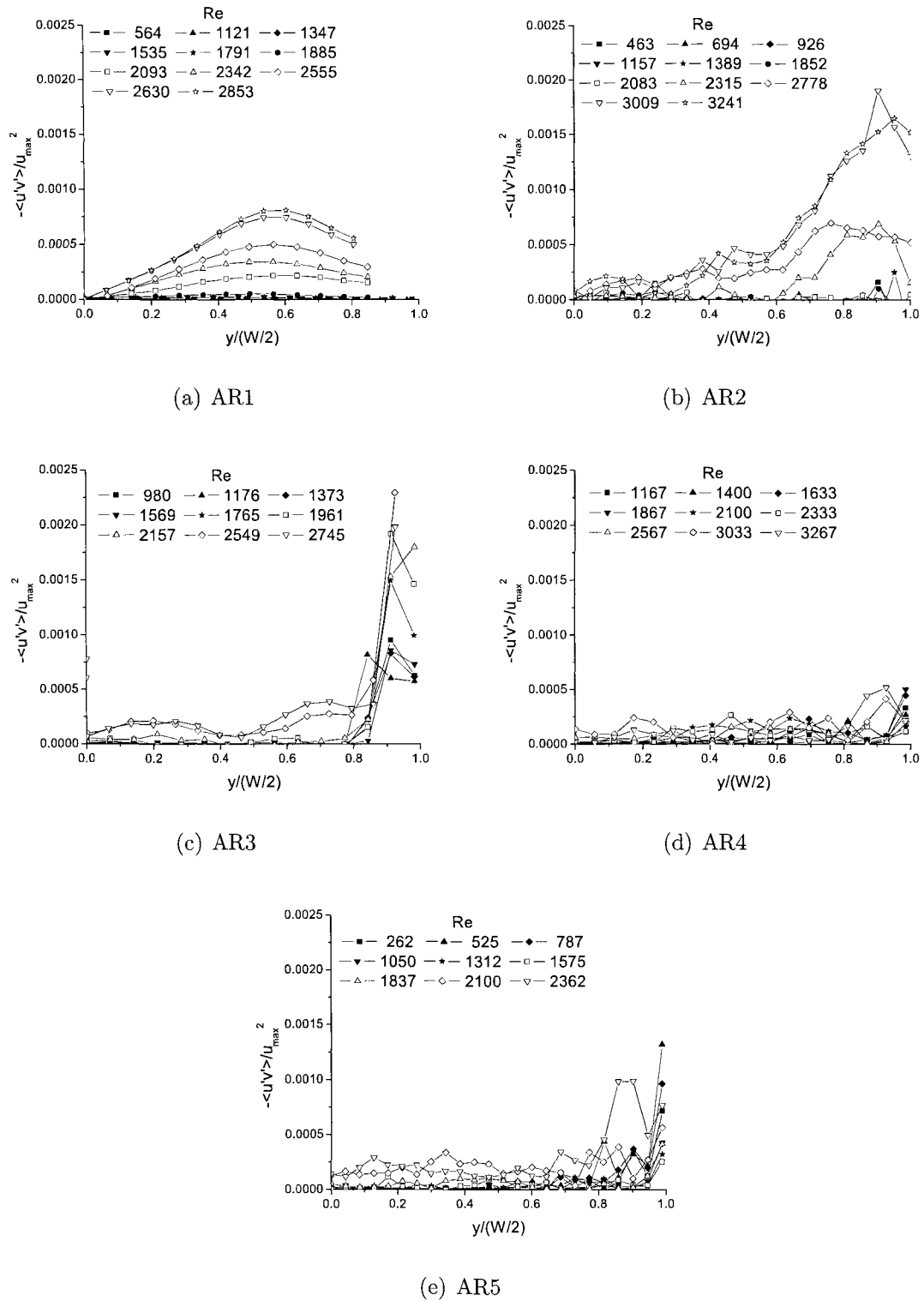


Figure 4.7 Reynolds shear stress profiles for five different aspect ratios as measured by microPIV

CHAPTER 5 EXAMINATION OF LARGE-SCALE STRUCTURES IN TURBULENT MICROCHANNEL FLOW USING MICROPIV

A paper submitted to *Experiments in Fluids*

H. Li and M. G. Olsen

Abstract

Microscopic particle image velocimetry was performed on turbulent flow in microchannels of various diameters and aspect ratios to evaluate the characteristics of large-scale turbulent structures. Spatial correlations of velocity fluctuations were measured along the channel centerlines and at four other locations, and characteristic turbulent length scales were defined. For square microchannels, excellent agreement was observed between the measured length scales and results for macroscale duct flow. Along the centerline of the square microchannels the normalized longitudinal length scale, $2Lx_{uu}/W$, ranged from 0.30-0.37, the lateral length scale, $2Ly_{uu}/W$, ranged from 0.16 – 0.18, and the ratio between the two length scales, Lx_{uu}/Ly_{uu} ranged from 1.88 – 2.00, results which agree well with macroscale results. Results for non-square microchannels indicate that as aspect ratio increases, the ratio Lx_{uu}/Ly_{uu} also increases, ranging from 2.29 for an aspect ratio of 2.09 up to 3.75 for an aspect ratio of 5.68. Measurements were repeated at various distances from the side walls of the microchannels. For the square microchannels the turbulent structures are smaller near the side walls than near the

center of the microchannel with $2Lx_{uu}/W$ ranging from 0.30-0.38 along the centerline, but dropping to 0.04-0.06 at $y/(W/D) = 0.94$. Similar results were observed for the rectangular microchannels. For the rectangular microchannels $2Lx_{uu}/W$ ranged from 0.32 to 0.42, compared to 0.30-0.38 for the square microchannels.

Introduction

In recent years, the characteristics of fluid flow in microchannels has been an area of great interest because of the importance of microfluidic microelectromechanical systems in such applications as microscale cooling [Tuckerman and Pease (1981)], drug delivery, biotechnical analysis, and telecommunication technologies [Henning (1998); Lipman (1999)]. However, many experimental studies of flow in microchannels have led to contradictory and controversial results. For example, a number of researchers have reported microscale fluid behavior that differs from classical macroscale results, while others have observed no such discrepancies.

The most commonly reported discrepancies have been transition to turbulence in microchannels at anomalously low Reynolds numbers and larger than expected frictional losses. For example, Wu and Little (1983, 1984) measured the friction factors of gas flow through etched microchannels with hydraulic diameters ranging from $45.46 \mu\text{m}$ to $83.08 \mu\text{m}$. Their results suggested an early onset of transition around $Re = 350$, far from the conventional macroscale transitional Reynolds number of $1800 - 2300$. They also measured abnormally high values of friction factor and attributed this to the large relative roughness of the etched channels. Peng et al. (1994a) and Peng and Peterson (1996a) measured the friction factor of water flow through rectangular stainless steel microchannels with hydraulic diameters of $0.133 - 0.367 \text{ mm}$ and aspect ratios of $0.333 - 1$ and reported transition at $Re = 200 - 700$ and fully turbulent flow also occurring at lower Reynolds numbers than macroscale channels. Mala and Li (1999) investigated

water flow through microtubes with diameters ranging from 50 to 254 μm and based on observations of the nonlinear relationship between pressure gradient and the volumetric flow rate concluded that early transition was occurring. A number of other researchers have similarly reported anomalous early transition in microchannels [Pfund et al. (2000); Gui and Scaringe (1995); Wu and Cheng (2003); Qu et al. (2000); Guo and Li (2003a,b); Sabry (2000)]. The relatively high surface roughness of microchannels compared to macroscale pipes and ducts is often given as a reason for these discrepancies.

However, a number of studies in microchannels with the same magnitude of channel surface roughness (1% – 2%) as researchers mentioned before have shown no anomalies in microchannel behavior. For instance, Hegab et al. (2002) performed experiments on single-phase flow in microchannels with hydraulic diameters ranging from 112 μm to 210 μm and reported transition between $Re = 2000 - 4000$. Qu and Mudawar (2002) studied the fluid flow characteristics of a microchannel heat sink with dimensions of 231 μm x 713 μm and found neither evidence of early transition nor deviation from macroscale pressure drop correlations. Judy et al. (2002) measured pressure drop in microtubes with hydraulic diameters between 15 μm and 150 μm for three different fluids (water, methanol, isopropanol), two different tube materials (fused silica, stainless steel) and two different tube cross-section geometries (circular, square) and found no distinguishable deviation from macroscale flow theory. Chung et al. (2002) studied single-phase flow in a 100 μm capillary tube and found the measured friction factor compared well with the conventional theory. The measured velocity also matched the theoretical profile for laminar flow in a circular microchannel.

The previously mentioned experiments were performed using traditional pressure drop and temperature measurements which can be quite challenging to apply to microscale flows. Indeed, in a recent review paper, Hetsroni et al. (2005) concluded after careful examination of data from previous experimental studies of microchannel flows that transition in both smooth and rough microchannels occurs between $1800 < Re <$

2200, and that reported instances of early transition were due to experimental conditions that were improper for comparisons to theoretical predictions.

Recently, researchers have begun to study transitional and turbulent microchannel flow using a relatively new experimental technique, microscopic particle image velocimetry (microPIV) [Santiago et al. (1998)]. The experiments performed thus far using microPIV have consistently shown microchannel behavior in agreement with classical theory. Sharp and Adrian (2004) performed pressure drop and microPIV experiments on transitional flow in round glass microtubes with diameters between 50 and 247 μm with working fluids of different polarities. In their microPIV experiments, the unsteady fluctuations of the centerline velocity were taken as indicators of the transition to turbulence. In the laminar region, centerline velocity fluctuations of around 1% (due to experimental noise) were observed, but at higher Reynolds numbers, the centerline velocity fluctuations increased, and the first abrupt increase of the rms value of centerline velocity was taken as the onset of transitional flow. Using this definition, transition was observed between $1800 < Re < 2200$. Li and Olsen performed microPIV experiments on square microchannels of differing hydraulic diameters [Li and Olsen (2005)] and rectangular microchannels with differing aspect ratios [Li and Olsen (2006)]. Using the same definition of transition as Sharp and Adrian (2004), they found the onset of transition between $Re = 1800$ and 2000 for all cases studied. Li and Olsen were the first researchers to report Reynolds stress data in microchannel flows and found that the measured Reynolds stresses agreed well with macroscale pipe and duct results.

Previous studies of turbulent microchannel flow have all reported either bulk fluid properties, such as pressure drop and flowrate, or pointwise velocity statistics, such as mean velocity and velocity fluctuations. In the present work, the characteristics of large-scale structures of turbulent flow in microchannels of various hydraulic diameters and aspect ratios are investigated. It will be shown that the present microPIV experiments have sufficient spatial resolution that individual large-scale turbulent structures can be

observed in the instantaneous velocity fields. In order to statistically characterize the large-scale structures, spatial correlations of velocity fluctuations are calculated, and these are compared to results for macroscale duct flow to determine if any differences exist in the characteristics of large-scale turbulent structures at the microscale compared to the macroscale.

Experimental Techniques

Microchannel Fabrication

The straight microchannels used in the present experiments were fabricated using PDMS replica molding [Anderson et al. (2000); Jo et al. (2000)]. Channel molds were prepared with patterned negative photoresist (SU-8 2100, MicroChem Corp., Newton, MA) on Silicon wafers (100 mm diameter, Montco Silicon Technologies, Inc., Spring City, PA) using UV light photolithography. Polydimethylsiloxane (PDMS) elastomer (Sylgard(R) 184 Silicone Elastomer Kit, Dow Corning, Midland, MI) was cast on the molds and baked. Finally, the two pieces of baked PDMS were plasma treated and bonded to form a complete microchannel. The surface roughness of the resulted channels was measured as $\epsilon_s/D_h \approx 0.000074$ by Dektak IIA surface profile measuring system (Veeco Instruments Inc., Santa Barbara, CA). The microchannel fabrication procedure is described in greater detail in Li's work [Li et al. (2005); Li and Olsen (2005, 2006)].

Microchannel widths were controlled by varying the design drawings of transparencies, and the microchannel depths were controlled by adjusting the amount of photoresist deposited on the wafer, the spinning speed of spin coater, the baking time, and the exposure time to UV light. Accurate determination of dimensions was essential to obtain reliable data. The optical measurement of the dimensions at various positions along the microchannels, accurate to within $\pm 10 \mu\text{m}$, indicated variations between 1.25% to 5%. The final length-averaged dimensions of the microchannel geometries were confirmed

with a microscope and are listed in Table 5.1.

Experimental Setup

The experimental system, schematically shown in Fig. 5.1, consists of two subsystems: (i) the flow delivery system (top portion); and (ii) the microPIV system (lower portion). The deionized water mixed with fluorescent particles was pressure-driven by a micro gear pump and pump head (115 VAC console digital dispensing drive and 0.084 ml/rev suction shoe gear pump head, Cole-Parmer Instrument Co., Vernon Hills, IL) with accuracy of flow rate at $\pm 0.3\%$. The fluorescent particles (Duke Scientific Co., Palo Alto, CA) delivered to the test section were excited by a double pulsed Nd:YAG laser beam (Continuum, Santa Clara, CA) and emitted light which was filtered and imaged through the inverted biological microscope [Nikon model T-300 Inverted Microscope] and LaVision Flowmaster 3 camera (Lavisoin Inc., Ypsilanti, MI). The instantaneous microPIV image pairs were analyzed using a cross-correlation technique to yield velocity vectors in the longitudinal (x) and transverse (y) directions. A multi-pass interrogation scheme with decreasingly smaller window sizes was used in the computation of the vector fields to reach the final 50% overlapped 32 x 32 pixels interrogation windows, yielding an in-plane spatial resolution of 14 μm . The out-of-plane spatial resolution is defined by the *depth of correlation* [Olsen and Adrian (2000b); Bourdon et al. (2004)]. In the present experiments, the 20X 0.45 NA microscope objective yields a depth of correlation of 8.3 μm . Achieving this spatial resolution required a volumetric particle concentration of approximately 0.057%. This volume fraction of seed particles was small enough that any two-phase effects were negligible, and the working fluid could be considered a single-phase fluid. Greater detail of the experimental principles and procedures can be obtained in Li's work Li et al. (2005); Li and Olsen (2005, 2006)].

Previous experiments [Li and Olsen (2005, 2006)] have indicated that the flow in the microchannels used in this study becomes fully turbulent at Reynolds numbers around

3000. To ensure fully turbulent flow in the present study, the experiments were performed at the maximum Reynolds numbers reported in the previous studies. Since the pressure drop within the microchannels is a function of flow rate, hydraulic diameter, and aspect ratio of microchannels, and since the bonding strength of each of the channels used in this study varied, a different maximum Reynolds number was achieved for each channel investigated in this study. The maximum achieved Reynolds numbers are summarized in Table 5.2.

Measurement Error

There are two sources of measurement errors in the microPIV experiments: errors introduced by random motion of the seed particles due to Brownian motion, and errors implicit in the interrogation of the PIV images. The significance of Brownian motion in the microPIV measurements can be determined by calculating the Brownian motion parameter, which is described in Olsen's work [Olsen and Adrian (2000a)]. The Brownian motion parameter quantifies the broadening of the correlation signal peak due to random Brownian motion of seed particles. For values of the Brownian motion parameter close to unity, Brownian motion has a negligible effect on the correlation signal peak, and hence a negligible effect on the measured velocity. For the AR5 microchannel at $Re = 525$, the Brownian motion coefficient is equal to 0.9998, indicating that Brownian motion effects are indeed negligible. For the smaller hydraulic diameter microchannels, or at higher Reynolds numbers in the AR5 microchannel, the Brownian motion effect is even smaller, due to the smaller Δt required for these measurements. Note that the fact that Brownian motion is negligible should not be surprising, given the short Δt required for each of the measurements (on the order of 1 microsecond).

The experimental error due to interrogation of the PIV images can be estimated by assuming that measured particle displacements are accurate to within approximately 1/10th of a seed particle image diameter [Prasad et al. (1992)]. The effective particle

diameter when projecting back into flow coordinates is $1.9 \mu\text{m}$, meaning that the measured particle displacement in the microPIV experiments should be accurate to within $0.19 \mu\text{m}$. For the present experiments, the particles travel approximately $8 \mu\text{m}$ between laser pulses, resulting in an experimental uncertainty of approximately 2.3%.

Results and Discussion

Visualization of Turbulent Structures

Great care was taken to sufficiently seed the working fluid so that high resolution, instantaneous velocity vector fields could be obtained. This resulted in velocity fields which had sufficient spatial resolution that large-scale turbulent structures could be observed. The turbulent structures within the velocity fields are readily observable if a constant convective velocity is subtracted from the instantaneous turbulent velocity fields. Figure 5.2 shows example instantaneous velocity fields with a convective velocity subtracted for microchannels SQ1, SQ3, RE1, and RE3 at the highest Reynolds numbers mentioned in Table 5.2 (note that because the mean velocity in each channel is different, a different convective velocity was used for each of the channels shown). Large-scale turbulent eddies of various sizes and shapes can be observed in each of the velocity fields. Varying the convective velocity that is subtracted from these images can make other turbulent structures within the flowfield more apparent. Although velocity fields such as those shown in Fig. 5.2 provide anecdotal evidence that turbulent structures in microscale flow appear similar to those observed in similar macroscale flows, definitive conclusions about the similarity (or lack thereof) between turbulent structures in microscale vs. macroscale flow can only come from a statistical analysis of the data. This was accomplished by calculating spatial correlations of velocity fluctuations and integral length scales.

Spatial Correlations and Integral Lengths along Channel Centerlines

Spatial correlations of velocity fluctuations and turbulent length scales are two parameters that can be used to quantitatively analyze the size of large-scale turbulent structures. The spatial correlation coefficient function was first defined by Taylor (1936). In the present work, only linear spatial correlations were calculated, meaning that only x or y were varied (and not both simultaneously) in an individual correlation calculation. In this way, both longitudinal correlations, denoted by $Rx_{u_i u_i}$, and lateral correlations, denoted by $Ry_{u_i u_i}$ were calculated using the following equations

$$Rx_{u_i u_i}(x; x_o, y_o) = \frac{\langle u'_i(x_o, y_o) u'_i(x + x_o, y_o) \rangle}{\sqrt{\langle u_i'^2(x_o, y_o) \rangle} \sqrt{\langle u_i'^2(x + x_o, y_o) \rangle}} \quad (5.1)$$

$$Ry_{u_i u_i}(y; x_o, y_o) = \frac{\langle u'_i(x_o, y_o) u'_i(x_o, y + y_o) \rangle}{\sqrt{\langle u_i'^2(x_o, y_o) \rangle} \sqrt{\langle u_i'^2(x_o, y + y_o) \rangle}} \quad (5.2)$$

where $u'_i(x_o, y_o)$ is the turbulent fluctuation of velocity in the i direction at a fixed point, (x_o, y_o) in the microchannel (hereafter referred to as the basis point), and $u'_i(x + x_o, y + y_o)$ is the turbulent fluctuation of velocity at a point displaced from the basis point by distances x and y in the streamwise and transverse directions, respectively. In the present work, only linear spatial correlations were calculated, meaning that only x or y were varied (and not both simultaneously) in an individual correlation calculation. In this way, both longitudinal correlations, denoted by $Rx_{u_i u_i}$, and lateral correlations, denoted by $Ry_{u_i u_i}$ were calculated. Because of the normalization used in the denominator, the value of $Rx_{u_i u_i}(0)$ or $Ry_{u_i u_i}(0)$ is always equal to one.

Figures 5.3(a) and 5.3(b) show the longitudinal spatial correlation Rx_{uu} and the lateral spatial correlation Ry_{uu} , respectively, for each of the microchannel geometries investigated for basis points located along the centerline of the microchannels. The spatial dimensions have been normalized by the half width of the microchannels, thus 0 represents a point along the center of the microchannel and 1 represents a point on the

side wall. Due to the normalization, all of the correlations are equal to 1 for a separation distance of zero. As the separation distance increases, the correlation function value decreases and exhibits an asymptotic decay to zero at large separation. This behavior is observed for both the longitudinal and the lateral correlations.

Comparison of spatial correlation data between different experimental conditions and locations using spatial correlation plots, such as those shown in Figs. 5.3(a) and 5.3(b) can be a rather clumsy exercise. A more efficient and direct comparison can be accomplished by calculating the integral length scales arising from the correlations. The integral length scales of the correlation functions represent one definition of the characteristic turbulent structure length scale. These length scales arise from the fluid particles within an individual turbulent structure moving cohesively. The integral length scales are calculated by integrating the spatial correlation functions as follows

$$Lx_{u_i u_i} = \int_0^{\infty} Rx_{u_i u_i}(x) dx \quad (5.3)$$

and

$$Ly_{u_i u_i} = \int_0^{W/2} Ry_{u_i u_i}(y) dy \quad (5.4)$$

Since it is physically impossible to collect experimental data, and therefore to integrate $Rx_{u_i u_i}$ all the way to ∞ , in practice $Lx_{u_i u_i}$ is calculated by integrating over a finite domain. This is not a problem so long as the data is collected over a large enough region that $Rx_{u_i u_i}$ asymptotes to zero, allowing the truncated integral to converge. However, in many of the cases investigated in the present study, the measured microPIV velocity fields did not cover a large enough area of the flowfield for the calculated spatial correlations to decay to zero, and thus Eqn. 5.3 could not be used to calculate a turbulent length scale. Instead, an alternative definition was used following the example of previous researchers. Wang et al. (1995) and Bernard-Michel et al. (2002) have suggested

defining a turbulent length scale based on the distance from the basis point where the normalized correlation function decreases to $1/e$ to indicate the size of turbulent structure. In the present work, this definition had to be modified slightly since in two of the investigated geometries (the RE3 and RE4 microchannels) it was impossible to collect data over a large enough window for the correlation to drop to $1/e$. Instead, the authors have chosen to define the turbulent length scales based on the location where spatial correlations decrease to 0.5. For consistency, this definition was used for all microchannel geometries and dimensions investigated.

Using this definition, the characteristic turbulent length scales Lx_{uu} and Ly_{uu} for basis points along the center of the microchannels have been determined. Normalized versions of these length scales and also the ratio of the two length scales are presented in Table 5.2. To determine if the large-scale turbulent structures observed in microchannel flows exhibit similar tendencies to the large-scale structures found in macrochannel flows, data from previous studies of flow in macroscale channel and pipe flows are also presented in Table 5.2. For consistency, these macroscale data were obtained using author's turbulent length definition.

The first seven entries in Table 5.2 are the results from the present study. Note that the total Reynolds number range for all the seven microchannels is from 2362 to 3489. This variation is in large part due to limitations in the microchannel fabrication process and the Reynolds numbers represent the maximum Reynolds number that could be attained before the microchannel catastrophically failed. As mentioned earlier, previous work [Li and Olsen (2005, 2006)] has indicated that in each case, the flow approaches a fully turbulent state at these Reynolds numbers.

The next four entries in Table 5.2 represent the results of Clark (1970) and Morton and Clark (1971) in a study of flow in a 25 mm square duct using laser-Doppler velocimetry (LDV). Clark collected his results for a range of Reynolds numbers from 3460 through 18,100 and observed some Reynolds number dependence on the measured

turbulent length scales. In the present study, the SQ1, SQ2, and SQ3 microchannels have the same square geometry as the duct used in Clark's study. The results from the present study agree very well with the macroscale results of Clark. The normalized longitudinal length scale, $2Lx_{uu}/W$, for the three square microchannels falls within the range of 0.30 – 0.37, which agrees very well with the range of 0.29 – 0.37 reported by Clark for Reynolds numbers between 3460 and 8300. Similarly, the lateral length scale, $2Ly_{uu}/W$, for the three microchannels falls within the range of 0.16 – 0.18, which agrees very well with the range of 0.16 – 0.20 reported by Clark for $3460 < Re < 8300$. Finally, a comparison of the ratio between the two length scales, Lx_{uu}/Ly_{uu} also shows good agreement, with the microchannel results ranging from 1.88-2.00 and the macroscale duct results ranging from 1.85 – 1.93. These results suggest that the large-scale structures observed in turbulent microchannel flows exhibit similar characteristics to those observed in macrochannel flows.

The final entries in Table 5.2 are from the experiments of Fraser et al. (1986) and Taylor (1936). In these studies only lateral turbulent length scales are reported. These results are for much higher Reynolds numbers than for the present microscale experiments, but they do show results for $2Ly_{uu}/W$ that are consistent with the experiments of Clark, and hence provide further evidence of the similarity between the large-scale structures observed in the microchannel experiments and macroscale fluid behavior.

Results of turbulent length scales along the channel centerline for non-square microchannels are also given in Table 5.2. These results indicate that as microchannel aspect ratio increases, the ratio Lx_{uu}/Ly_{uu} also increases, ranging from 2.29 for an aspect ratio of 2.09 up to 3.75 for an aspect ratio of 5.68. This increase in Lx_{uu}/Ly_{uu} is due to a decrease in the $2Ly_{uu}/W$ length scale, as the $2Lx_{uu}/W$ remains relatively constant with changes in aspect ratio. The authors were unable to find the results of similar experiments for macroscale flows for comparison.

Spatial Correlations and Length Scales at Various Distance from the Wall

Spatial correlations and turbulent length scales were also calculated using basis points at locations other than the microchannel centerline, but still in the midplane of the microchannel. In the high aspect ratio microchannels, this midplane was parallel to the ‘long’ sides of the microchannel (*i.e.*, the ‘short’ sides of the microchannels were bisected by this measurement plane). Correlation and turbulent length scales were calculated for basis points lying approximately at the microchannel centerline and at distances approximately equal to one-half, one-fourth, one-eighth, and one-sixteenth of a microchannel half-width from the side wall. Note that because microPIV vectors are located only at discrete points in the flowfield, the locations of the basis points varied slightly from these locations for each case studied.

Results for the longitudinal spatial correlations of u velocity and v velocity for basis points located at various distances from the side wall are shown in Figs. 5.4 and 5.5, respectively for each of the seven microchannels investigated in this study. For the three square channels (SQ1, SQ2, and SQ3), the results indicate that the Rx_{uu} curves for $y/(W/2) = 0, 0.5, \text{ and } 0.75$ are all nearly identical. It is only for the two basis point locations closest to the side walls ($y/(W/2) = 0.87, \text{ and } 0.94$) that variations in Rx_{uu} are observed. The correlations drop off much more drastically at these near wall locations, indicating that the large-scale turbulent structures are smaller near the side walls than near the center of the microchannel. These results are quantified by calculating a turbulent length scale based on distance from the basis point where the correlation drops to 0.5, as described earlier. These turbulent length scales as a function of distance from the side walls are summarized in Table 5.3. As Table 5.3 indicates, the normalized turbulent length scale, $2Lx_{uu}/W$ ranges from 0.30 – 0.38 for the three square microchannels for centerline basis point locations with the $y/(W/2) = 0.5$, and 0.75 being slightly lower. However, $2Lx_{uu}/W$ drops significantly at $y/(W/2) = 0.87$ and

falls even further for $y/(W/2) = 0.94$ where $2Lx_{uu}/W$ is between 0.04 and 0.06.

Similar results are observed for the RE1 – RE4 microchannels, with the interior basis point locations showing similar correlation curves for these these channels, and the correlation dropping off more quickly at the two near wall locations. The RE4 microchannel does show slightly different behavior, with the correlation also dropping off a bit from the centerline to the $y/(W/D) = 0.5$, and 0.75 locations and then dropping off again at the two near wall locations. As seen in Table 5.3, the centerline length scales for these four channels are similar to the length scales in the square channels, with $2Lx_{uu}/W$ ranging from 0.32 to 0.42, which is nearly the same as the 0.30 – 0.38 range observed in the square microchannels.

Results for the Rx_{vv} correlations are shown in Fig. 5.5. These results are a bit noisier than the Rx_{uu} results, but still show the same general trends with correlations falling off more quickly in the near wall regions than near the channel centerline. Turbulent length scales were also measured from these correlations, and the results for $2Lx_{vv}/W$ are also presented in Table 5.3. These results show that $2Lx_{vv}/W$ tends to decrease by 70 – 80% as the basis point is moved from the centerline to the near wall location.

Summary and Conclusions

Microscopic particle image velocimetry (microPIV) experiments were performed on turbulent microchannel flows to determine if the large-scale turbulent structures in microchannels exhibited similar characteristics to large-scale structures in macroscale pipes and ducts. Three different diameters of square microchannels were investigated, and five different aspect ratios of microchannel were investigated. The microPIV measurements were of sufficient spatial resolution that large-scale turbulent structures could be observed in the flowfield. To provide a statistical basis for evaluation of the large-scale structures, spatial correlations of velocity fluctuations were measured from the instan-

taneous velocity fields for basis points located along the channel centerline and at four other locations throughout the channel. Characteristic turbulent length scales were then defined based on the distance from the basis point where the correlation falls to one-half of its peak value.

For the square microchannels, excellent agreement was observed between the measured turbulent length scales and previous results for macroscale duct flow. The normalized longitudinal length scale, $2Lx_{uu}/W$, for basis points located along the centerline of the three square microchannels ranged between 0.30 – 0.37, which agrees very well with the range of 0.29 – 0.37 reported for macroscale ducts of similar Reynolds numbers. Moreover, the lateral length scale, $2Ly_{uu}/W$, for the microchannels ranged from 0.16 – 0.18, also agreeing well with macroscale duct results. A comparison of the ratio between the two length scales, Lx_{uu}/Ly_{uu} also shows good agreement, with the microchannels ranging from 1.88 – 2.00 and the macroscale ducts ranging from 1.85 – 1.93. Results of turbulent length scales along the channel centerline for non-square microchannels indicate that as microchannel aspect ratio increases, the ratio Lx_{uu}/Ly_{uu} also increases, ranging from 2.29 for an aspect ratio of 2.09 up to 3.75 for an aspect ratio of 5.68. This increase in Lx_{uu}/Ly_{uu} is due to a decrease in the $2Ly_{uu}/W$ length scale, as the $2Lx_{uu}/W$ remains relatively constant with changes in aspect ratio.

Spatial correlations and turbulent length scales for basis points located at various distances from the side wall were also measured for each of the seven microchannels investigated in this study. For the three square channels the results indicate that the large-scale turbulent structures are smaller near the side walls than near the center of the microchannel. The normalized turbulent length scale, $2Lx_{uu}/W$ ranges from 0.30 – 0.38 for centerline basis point locations, but drops significantly at $y/(W/2) = 0.87$ and falls even further for $y/(W/D) = 0.94$ where $2Lx_{uu}/W$ is between 0.04 and 0.06. Similar results are observed for the RE1 – RE4 microchannels. The centerline length scales for these channels are similar to the length scales in the square channels, with $2Lx_{uu}/W$

ranging from 0.32 to 0.42, which is nearly the same as the 0.30 – 0.38 range observed in the square microchannels.

Table 5.1 Geometric parameters of test microchannels

Channel Name	W (μm)	H (μm)	D_h (μm)	Aspect Ratio (W/H)
SQ1	320	330	325	0.97
SQ2	480	490	485	0.98
SQ3	640	640	640	1.00
RE1	480	230	311	2.09
RE2	640	210	316	3.05
RE3	800	200	320	4.00
RE4	1080	190	323	5.68

Table 5.2 Comparison of normalized turbulent length defined at the length where $R = 0.5$.

Reference	Test Channel	Measurement Technique	Re	$2Lx_{uu}/W$	$2Ly_{uu}/W$	Lx_{uu}/Ly_{uu}
Author	SQ1	microPIV	2853	0.38	0.20	1.90
Author	SQ2	microPIV	3489	0.34	0.17	2.00
Author	SQ3	microPIV	3333	0.30	0.16	1.88
Author	RE1	microPIV	3241	0.32	0.14	2.29
Author	RE2	microPIV	2745	0.42	0.18	2.33
Author	RE3	microPIV	3267	0.32	0.12	2.67
Author	RE4	microPIV	2362	0.30	0.08	3.75
Clark (1970)	25 mm	LDV	3460	0.37	0.20	1.85
Clark (1970)	25 mm	LDV	8300	0.29	0.16	1.93
Clark (1970)	25 mm	LDV	14300	0.25	0.13	1.93
Clark (1970)	25 mm	LDV	18100	0.26	0.13	2.0
Fraser et al. (1986)	76 mm	LDV	190000	–	0.12	–
Fraser et al. (1986)	76 mm	HWA	190000	–	0.10	–
Taylor (1936)	73.7 mm	HWA	14000	–	0.14	–

Table 5.3 Wall effect on normalized turbulent length

Test Channel	Longitudinal turbulent length	Distance from centerline $2y/W$				
		0.00	0.50	0.75	0.87	0.94
SQ1	$2Lx_{uu}/W$	0.38	0.38	0.33	0.16	0.04
	$2Lx_{vv}/W$	0.22	0.22	0.10	0.08	0.06
SQ2	$2Lx_{uu}/W$	0.34	0.26	0.29	0.08	0.05
	$2Lx_{vv}/W$	0.07	0.08	0.08	0.07	0.05
SQ3	$2Lx_{uu}/W$	0.30	0.35	0.32	0.07	0.06
	$2Lx_{vv}/W$	0.14	0.14	0.14	0.11	0.09
RE1	$2Lx_{uu}/W$	0.32	0.29	0.36	0.13	0.04
	$2Lx_{vv}/W$	0.20	0.16	0.16	0.04	0.04
RE2	$2Lx_{uu}/W$	0.42	0.40	0.32	0.08	0.04
	$2Lx_{vv}/W$	0.20	0.20	0.09	0.04	0.04
RE3	$2Lx_{uu}/W$	0.32	0.32	0.30	0.22	0.11
	$2Lx_{vv}/W$	0.08	0.03	0.03	0.02	0.02
RE4	$2Lx_{uu}/W$	0.30	0.18	0.17	0.09	0.07
	$2Lx_{vv}/W$	0.10	0.04	0.04	0.02	0.02

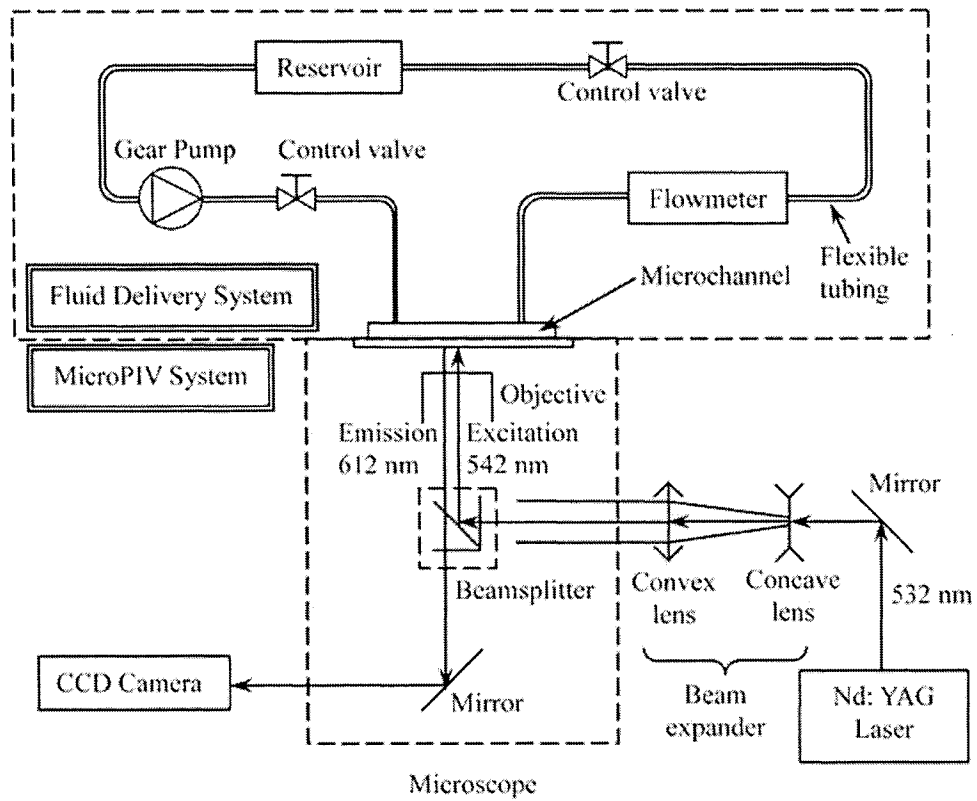


Figure 5.1 Schematic of experimental setup

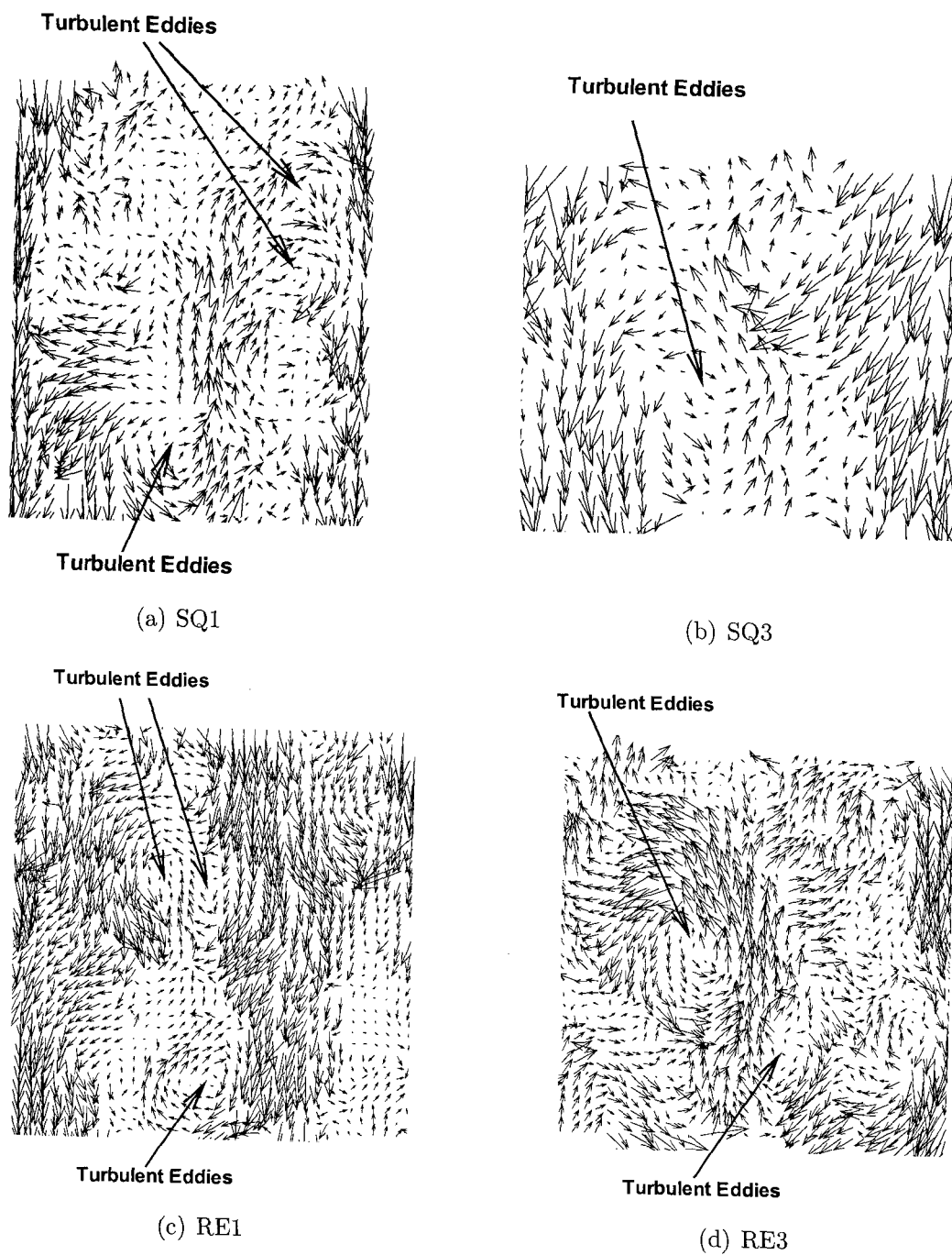
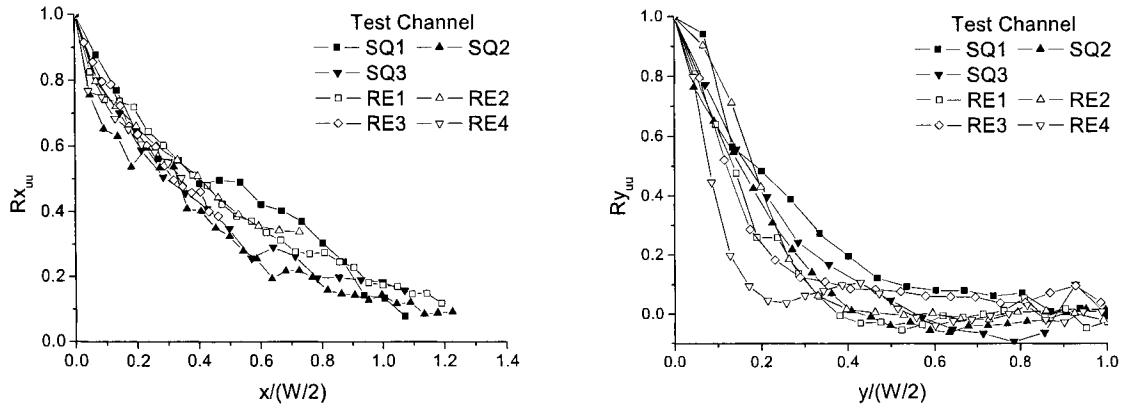
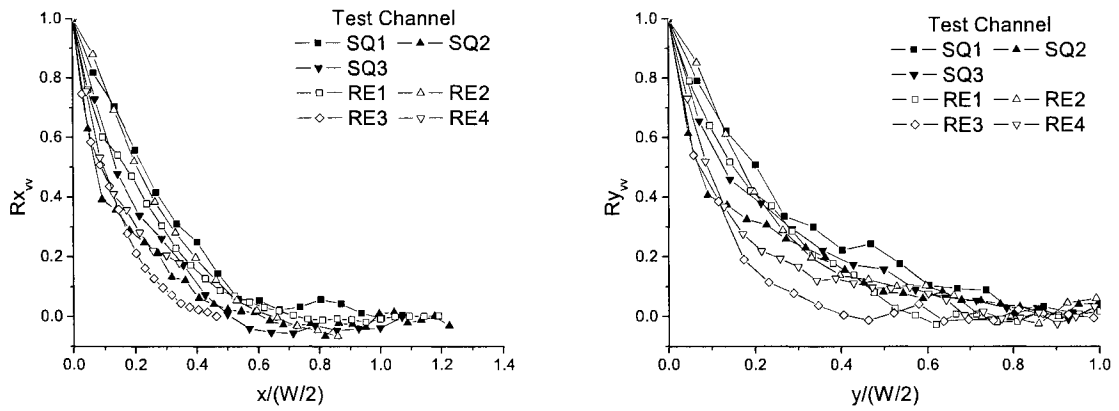


Figure 5.2 Example velocity fields indicating the presence of turbulent structures

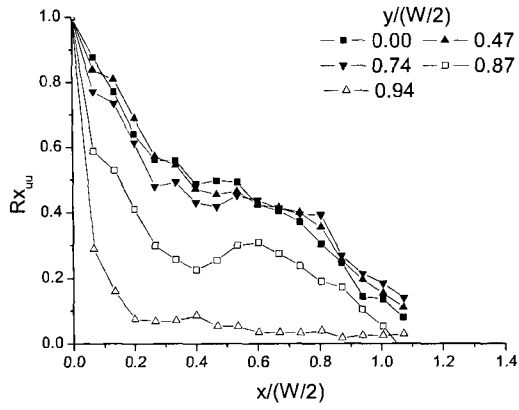


(a) Longitudinal correlation of streamwise velocity components, $R_{x_{uu}}(x, 0)$ (b) Lateral correlation of streamwise velocity components, $R_{y_{uu}}(0, y)$

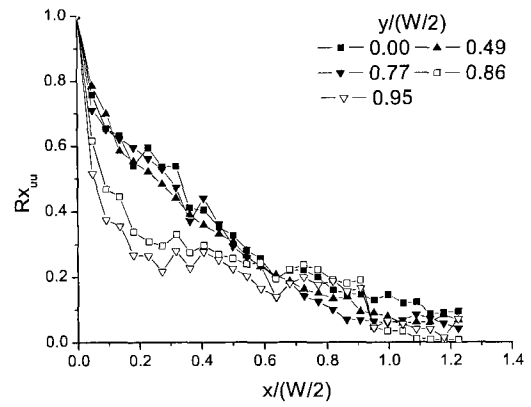


(c) Longitudinal correlation of transverse velocity components, $R_{x_{vv}}(x, 0)$ (d) Lateral correlation of transverse velocity components, $R_{y_{vv}}(0, y)$

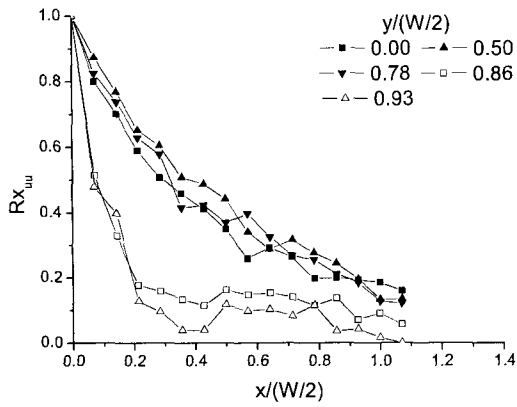
Figure 5.3 Spatial correlations at microchannel centerlines



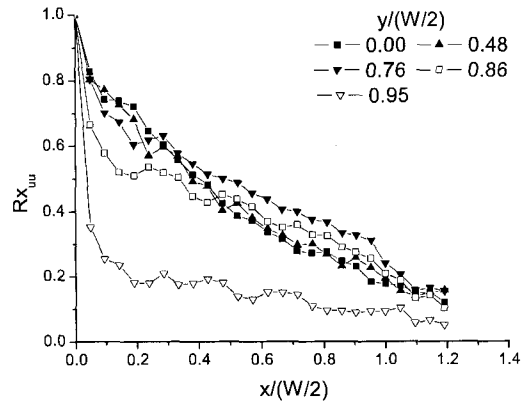
(a) SQ1



(b) SQ2



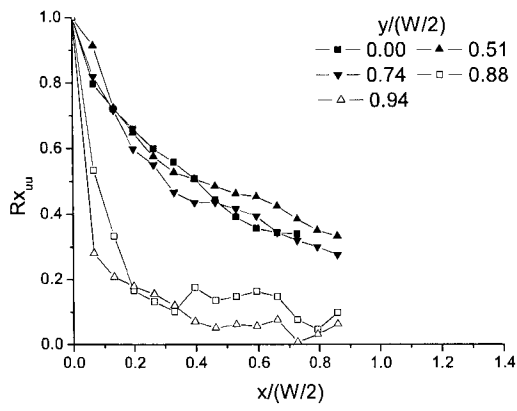
(c) SQ3



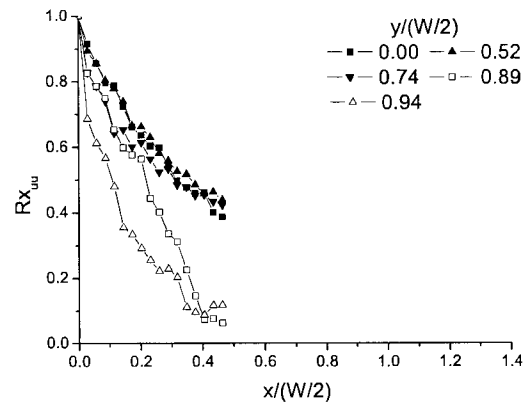
(d) RE1

Figure 5.4 Wall effect on spatial correlation functions $R_{x_{uu}}$

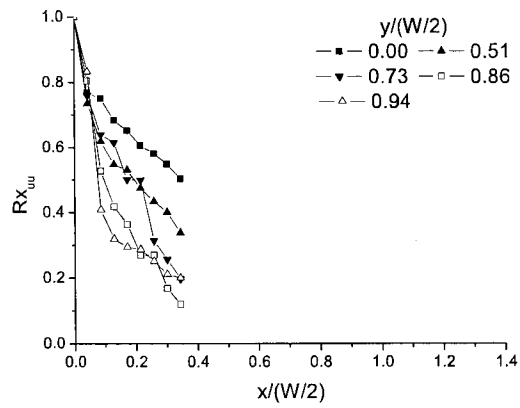
Figure 5.4 (Continued)



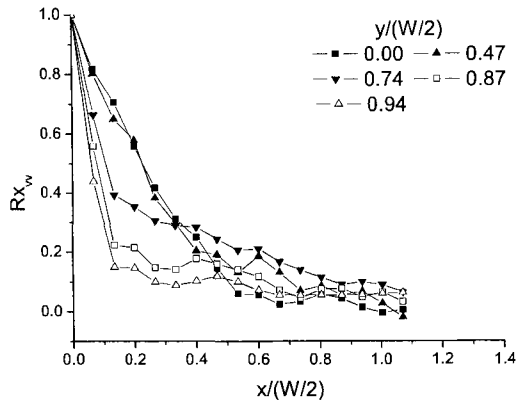
(e) RE2



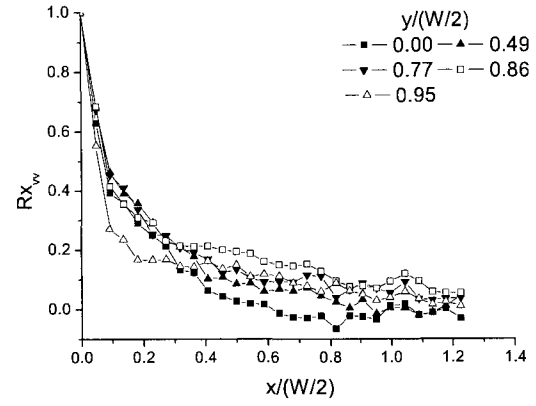
(f) RE3



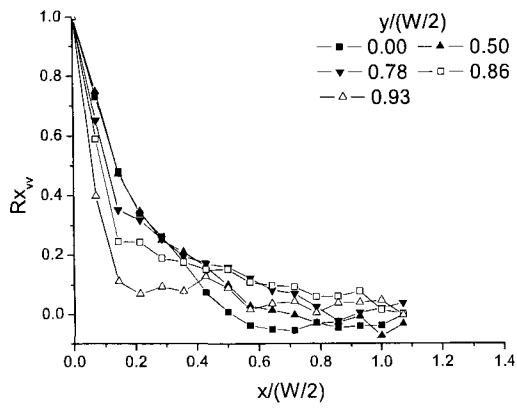
(g) RE4



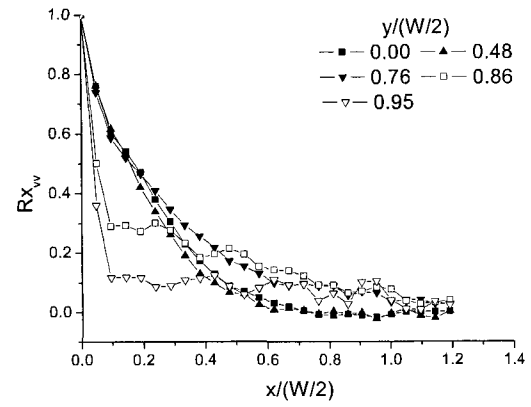
(a) SQ1



(b) SQ2



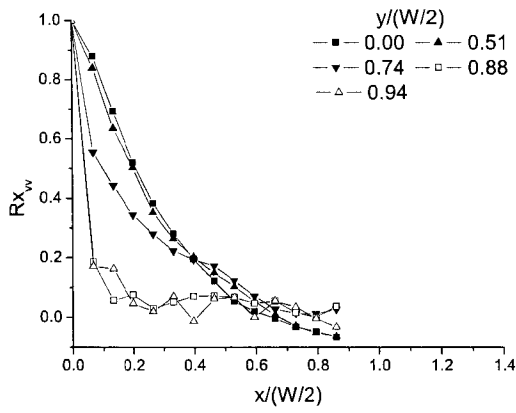
(c) SQ3



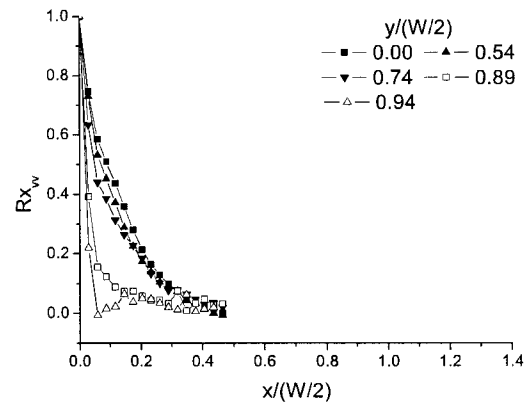
(d) RE1

Figure 5.5 Wall effect on spatial correlation functions Rx_{vv}

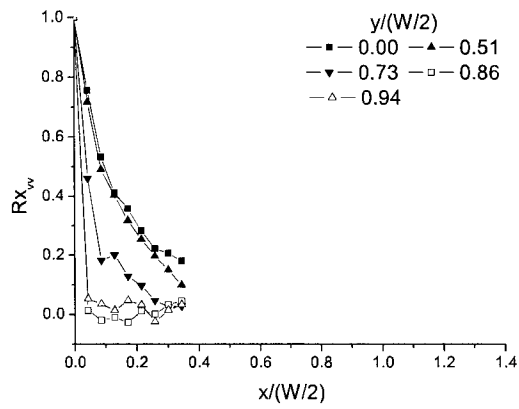
Figure 5.5 (Continued)



(e) RE2



(f) RE3



(g) RE4

CHAPTER 6 MICROFLUIDIC FLOW AROUND A SINGLE MICROSTRUCTURE IN A MICROCHANNEL

A paper submitted to *Journal of Microelectromechanical Systems*

H. Li, A. Tworek, F. Bondar, K. James, F. Battaglia, and M. G. Olsen

Abstract

A microchannel with a microstructure protruding from one surface was investigated experimentally using microscopic particle image velocimetry (microPIV), and numerical calculations were performed on a microchannel of the same geometry for comparison. Adding microstructures to a microchannel can increase the surface-area-to-volume ratio and increase the heat transfer rates for high heat flux applications. Microstructures may also enhance mixing in microscale combustion applications. Experiments were performed to measure the velocity field downstream of a $120\ \mu\text{m}$ square microchannel with a height of $43\ \mu\text{m}$ in a rectangular microchannel with a cross section measuring $600\ \mu\text{m}$ by $165\ \mu\text{m}$. Velocity fields were measured for Reynolds numbers based on microchannel hydraulic diameter of 108, 216, 431, and 1078. Experimental measurements showed a prominent wake downstream of the microstructure that propagated far downstream. As Reynolds numbers were increased, the wake effects downstream of the microstructure are more pronounced. The numerical simulations were shown to be in excellent agreement with the experiments, thus validating the use of simulations as an additional tool in analyzing flow features and providing data that can not otherwise be measured for microchannels

and microstructures of the scale investigated in this study.

Introduction

Microelectromechanical systems (MEMS) are an emerging technology that has transcended many areas of engineering and science. Microfluidic MEMS involve the flow of liquid or gas through the device to accomplish its design purpose. One application area of microfluidic MEMS is in the development of compact heat exchangers for use in heat sinks for microprocessors, wearable air conditioners for firefighters or soldiers in harsh environments, and portable cooling units such as mini refrigerators and mini air conditioners. Another emerging technology that relies heavily on microchannel flows and heat transfer is the development of compact fuel cells. Microscale flows are also important in power generating technologies such as microcombustors and micro gas turbines.

Microscale channels transfer heat very efficiently due to their large surface-area-to-volume ratios. As spatial dimensions become smaller, convective heat transfer in pipes or channels becomes more efficient because the surface-area-to-volume ratio increases [Tuckerman and Pease (1981, 1982)]. However, increasing the surface-area-to-volume ratio by decreasing pipe or channel diameter comes at a potentially great cost. For a constant volumetric flowrate, the pressure required to drive fluid through a microchannel is inversely proportional to the diameter to the fourth power, so a small decrease in channel diameter may necessitate a large increase in the power required for pumping. Moreover, the necessary pumping power to force fluid through microchannels can be even greater than values predicted by conventional theory, as was found by researchers who measured frictional losses in microchannels [Peng and Wang (1993); Peng et al. (1994a,b,c); Peng and Peterson (1995, 1996a); Papautsky et al. (1999); Adams et al. (1998); Rahman and Gui (1993); Mala and Li (1999)]. These greater than expected frictional losses have usually been attributed to surface roughness effects.

Instead of decreasing channel diameter, the surface-area-to-volume ratio of microchannels can also be increased by introducing microstructures onto the interior walls (e.g., the effectiveness of adding grooves to mesoscale channels has been demonstrated by Hopkins et al. (1999) and Khrustalev and Faghri (1999)). Microstructures can increase the surface-area-to-volume ratio and help maintain smaller corresponding frictional losses than for smaller diameter microchannels with the same surface area-to-volume ratio. Thus, the addition of arrays of microstructures into microchannels may be an efficient method to enhance heat transfer in high heat flux applications.

Through careful design of microchannel characteristics such as microstructure size and geometry, and array characteristics such as microstructure spacing and placement, it may be possible to determine an optimal microchannel design for heat flux applications that both maximizes the heat flux from a microchannel while keeping frictional losses to a minimum. This type of design optimization can be performed best using computational fluid dynamics (CFD), where flowfields can be investigated in great detail and geometries can be easily changed, instead of a time-consuming trial-and-error approach using microfabrication and experimental methods. However, before pursuing CFD as a tool for microchannel design, it is first necessary to verify that the computational methodologies used are able to accurately predict the flow phenomena associated with flows in microchannels containing protruding microstructures.

The objective of the work presented here is to provide a validation of computational results for flow around microstructures in microchannels with experimental data collected using microscopic particle image velocimetry (microPIV). First, microchannels were designed and constructed containing a single microstructure protruding from one of the microchannel walls. MicroPIV experiments were then performed to measure the velocity field around these microstructures over a range of Reynolds numbers. Finally, the experimental results were compared with CFD results for similar geometries to determine the viability of using CFD for design of microchannels with microstructures.

Microchannel Fabrication

Advances in microfluidic device technology have in large part been made possible by the vast array of microfabrication techniques available. Many of these fabrication techniques, such as micromachining, photolithography, and wet and dry etching have been developed for creating microdevices from silicon. However, one drawback of silicon-based microdevices is that the opaque nature of silicon can limit the accessibility of optical-based flow diagnostics techniques to the flowfield. The microPIV experiments described herein require devices that allow for optical access. For this reason, PDMS replica molding, a rapid-prototyping photolithography technique using polydimethylsiloxane (PDMS) [Anderson et al. (2000); Jo et al. (2000)], was utilized in the fabrication of the microchannels used in these experiments. Devices fabricated using this technique are ideal for optical-based experiments because PDMS is transparent in wavelengths from 230 – 700 nm, allowing for unlimited optical access to the interior of the device within this range of wavelengths.

The channels used in the described experiments were microchannels with a rectangular microstructure protruding along the centerline of one of the walls. The channel was cast in two pieces. The piece containing the rectangular microstructure was fabricated at a thickness of 43 μm , and the empty piece was made at a thickness of approximately 120 μm . After the plasma treatment, these two pieces were bonded together, resulting in an enclosed microchannel containing a single rectangular microstructure. Despite the rather large pressure drops associated with flow through these microchannels, especially at the highest Reynolds numbers investigated, the plasma bonding held up very well, and no leaking at the bonded interface was observed. The PDMS replica molding procedure consists of two steps, the mold fabrication and channel fabrication. The mold and channel fabrication processes are summarized in Fig. 4.1.

Mold Fabrication

A 4-inch, one-sided silicon wafer was used as a substrate for the formation of the mold (Fig. 6.1A). The substrate was cleaned with solvent and developer using a spin coater and then prebaked for 90 minutes at 150°C to remove moisture. The wafer was then placed on a spin coater, and SU-8 50 negative photoresist (MicroChem) was deposited onto the wafer (Fig. 6.1B). To achieve a photoresist thickness of 43 μm , the wafer and resist were spun for 30 seconds at about 2500 rpm. For the 120 μm pieces, the speed was decreased to about 1500 rpm. All spin processes were preceded by 10 seconds at 500 rpm, to reduce surface irregularities caused by rapid acceleration. The resist-coated wafer was then slowly heated and soft baked at 90°C on a level surface for about 40 minutes to evaporate the solvent in the resist.

The desired microchannel and microstructure geometries were then imparted on the photoresist by exposing select regions of the resist-coated wafer to ultraviolet light through the use of masks. The masks were printed on transparencies with a 3048 dpi laser printer. The resist was exposed through the mask to a UV light source with a total exposure dose of 650 mJ/cm^2 . The wafer was then slowly heated and baked again at 90°C for about 15 minutes to complete cross-linking (Fig. 6.1C). The mold was cooled and immersed in propylene glycol methyl ether acetate (PGMEA) for 6-10 minutes to develop the photoresist and then cleaned with isopropanol (Fig. 6.1D). No hard bake was necessary.

Microchannel Fabrication and Geometry

PDMS was then mixed and poured onto each half of the channel mold (Fig. 6.1E). Once all visible bubbles had evaporated, the PDMS casting was baked at 90°C for 30 minutes to cure. The channel halves were cut out (Fig. 6.1F) and inlet holes were punched into the empty half. The PDMS was then plasma-treated at 35 W for 1 minute

to promote bonding, and the two halves were immediately assembled under a microscope with a mask aligner (Fig. 6.1G). Care was taken in alignment to minimize any overhang between the two halves. To retain the hydrophilic properties introduced by plasma treatment, the channels were cleaned and stored in deionized water. The fabricated channel is 600 μm wide and 165 μm deep; the microstructure is 120 μm square and 43 μm high. Figure 6.2 shows an overhead view of the completed channel containing the microstructure. The widths and depths of the channel on each mold were verified by examining a cut PDMS cross-section under a calibrated microscope.

Experimental Methodology

The experimental apparatus, schematically shown in Fig. 3, consisted of two parts: (i) the flow delivery system; and (ii) the microPIV system. Capillary tubes were inserted into entry ports fabricated into the PDMS upstream and downstream of the microchannel. The interface between the capillary tubes and the PDMS was then sealed using an epoxy to prevent any fluid leakage from the entrance and exit ports of the microchannel. The microchannel was connected to the flow delivery system by affixing flexible tubing to the capillary tubes. The tubing diameter was chosen such that it fit tightly enough over the capillary tubes that no fluid leakage occurred. The flow was driven by a syringe pump. The syringe pump was chosen because it allowed a wide range of volumetric flowrates to be easily investigated. The microchannel was connected to the flow delivery system with flexible tubing.

The microPIV system is shown in the lower portion of Fig. 6.3. The microchannel was placed on the stage of an inverted biological microscope [Nikon model T-300 Inverted Microscope], and fluid containing fluorescent microspheres was allowed to flow through the microchannel. The light beam from a New Wave Research Gemini Nd:YAG PIV laser was expanded before entering the microscope through an aperture in the back. The

laser light was then directed toward the microchannel by a dichroic mirror and passed through a microscope objective, illuminating the seed particles. The Gemini laser is capable of producing up to 120 mJ per laser pulse, but only a small fraction of this light is necessary for the present microPIV experiments. An optical attenuator is therefore used to reduce the laser energy to less than 3 mJ/pulse.

The 900 nm diameter fluorescent seed particles (Polystyrene microspheres, Interfacial Dynamics Corp., Portland, OR) were excited by the laser light and emitted light at a peak excitation wavelength of 612 nm. A beamsplitter removed the illuminating and background light such that only the emitted light from the particles reached the CCD camera. Two images were captured per realization, and the two images were analyzed using a cross-correlation technique to yield the instantaneous velocity vector field. The PIV system and software include a LaVision Flowmaster 3 camera and DaVis analysis software (LaVision Inc., Ypsilanti, MI).

An equation describing the depth of the measurement volume (termed the depth of correlation in microPIV) was derived by Olsen and Adrian (2000b) and can be expressed in terms of a correlation distance, Z_{corr} , beyond which particles no longer significantly contribute to the measured velocity. The measurement depth, or depth of correlation is simply $2Z_{corr}$, where Z_{corr} is

$$Z_{corr} = \left[\frac{(1 - \sqrt{\epsilon})}{\sqrt{\epsilon}} \left(f^{\#2} d_p^2 \frac{5.95(M + 1)^2 \lambda^2 f^{\#4}}{M^2} \right) \right]^{1/2} \quad (6.1)$$

In Eqn. 6.1, $\epsilon = 0.01$, $f^{\#}$ is the focal number of the lens, d_p is the particle diameter, M is the magnification, and λ is the wavelength of light emitted by the particle (note that an alternative equation for the depth of correlation derived by Meinhart et al. (2000) yields a similar result). In the present experiments, a 20X 0.45 NA objective was used, yielding a depth of correlation of 8.3 μm .

The seed particle concentration used in these experiments was equal to approximately

0.0567% by volume. This volume fraction of seed particles is small enough that any two-phase effects are negligible, and the working fluid can be considered a single-phase fluid. In the microPIV experiments, deionized water was used as the working fluid. In order to prevent the buildup of contaminants in the system, air was pumped through the microchannel first to expel stagnant water and other contaminants. The fluorescent-particle-containing deionized water solution was then pumped through the microchannel at the specified volumetric flowrate.

The experiments were performed for various volumetric flow rates that yielded Reynolds numbers based on the microchannel hydraulic diameter ranging from 108 to 1078. For each flow rate, the system was allowed to run long enough before the collection of data such that the flow reached a steady state. For smaller flow rates, it took a longer time to reach a steady state compared to higher flow rates. Interrogation windows were 32 pixels square and measured $28\ \mu\text{m}$ on a side. Adjacent interrogation windows were overlapped by 50%, yielding a spatial resolution of $14\ \mu\text{m}$. This spatial resolution resulted in 44 vectors to be measured across the width of the microchannel. The timing between laser pulses was set such that the particles moved approximately 1/4th of an interrogation window between pulses. This results in an experimental uncertainty of less than $\pm 2.5\%$ [Prasad et al. (1992)]

For every volumetric flow rate, images at six different microchannel depths were collected. In order to determine the steady state, (i.e., time-averaged) velocity field and to minimize the effects of random measurement noise, for each flow rate and depth, 50 instantaneous images were captured and an ensemble average of correlation fields was used for the calculation of the vector field. Before computation, masks were applied in the certain regions of the flowfield images, for example, in the microstructure structure region and beyond the microchannel walls, to eliminate any effects due to spurious velocity vectors. In order to show the effect of the microstructure on the fluid flow, images were captured at various locations downstream of the microstructure. These

experimentally measured velocity vector fields were used to validate the accuracy of computational results for this microchannel geometry.

Computational Methodology

Three-dimensional numerical simulations were performed using FLUENT 6.0 and GAMBIT for grid-meshing. The governing equations were formulated using standard finite volume procedures. A second-order upwind scheme was selected for discretization of the advection terms in the momentum equation. The diffusion terms were discretized using second-order central differences. An implicit segregated solver to correct for the pressure field was implemented and the pressure-velocity coupling was based on the SIMPLE method. All simulations were carried out for steady-state calculations. Convergence was attained by requiring that the solution residuals of the dependent variables decreased by at least a factor of four orders of magnitude.

The overriding issue for computations in microchannels is grid resolution. Adequate grid resolution is necessary for reliability of any simulation. In the case of a microchannel, often the geometry includes one dimension that is significantly larger than the other dimensions. The experimental microchannel used in this study was designed to attain fully developed laminar flow, therefore, the channel length is more than 100 times the hydraulic diameter. Due to the large geometric aspect ratio of the microchannel, ($x/y = 66$ and $x/z = 242$), simulations were computationally intensive for adequate grid resolution. Therefore, a modification to the geometry was first considered for the computational model in order to speed-up the simulations.

The geometry used for all simulations was identical to the experimental geometry with the exception that the channel length downstream of the microstructure was shortened to 8 mm (as opposed to 20 mm in the fabricated channels). This shorter length was chosen in an effort to reduce the number of grid cells used in the computations in

the streamwise direction. To ensure that the shorter channel length did not adversely affect the flow dynamics upstream, velocity profiles were examined at the exit to verify that fully developed flow was recovered in the simulations. In addition, it was found that simulations of the channel for the full width (600 μm) produced symmetric flow about the midplane (as expected), which was consistent with the experiments. The symmetric nature of the flowfield in the spanwise direction permitted modeling one-half of the microchannel width. Boundary conditions were specified for an inlet velocity profile based on the mean velocity, u_{mean} , and ambient pressure at the exit. A no-slip boundary condition was enforced at all surfaces and a symmetry boundary condition was invoked along the channel centerline.

An extensive grid sensitivity study was conducted whereby resolution was increased in all three directions independently. It was found that the flow results were not affected with increased resolution in the streamwise direction. Both the cross-stream (z) and spanwise (y) resolutions were increased simultaneously, but the most significant changes were found in the y -direction. A finer grid was used around the bump surfaces. The final grid size included 1812 x 30 x 42 cells in the x -, y -, and z -directions, respectively. It was found that using this resolution resulted in only 2% error compared to higher resolutions.

Results and Discussion

Experimental measurements of the flow downstream of the microstructure in the microchannel were conducted at four Reynolds numbers based on the hydraulic diameter: $Re_{D_h} = 108, 216, 431, \text{ and } 1078$ (these Reynolds numbers can also be expressed in terms of the microstructure lengths, resulting in measurements taken at $Re_d = 50, 100, 200 \text{ and } 500$). MicroPIV measurements were taken at several locations downstream of the microstructure, ranging up to 1 mm downstream. Two downstream measurement

locations, 350 and 700 μm will be used to compare with the computational results. At each downstream location, data was collected at six cross-stream locations (or channel depths, z). The locations of the six cross-stream locations and their correspondence to the microstructure and channel height are shown in Fig. 6.4. Hereafter, these six cross-stream locations will be referred to as z_1 through z_6 .

Examples of microPIV velocity fields collected for a Reynolds number of 1078 are shown in Fig. 6.5. These figures show the flow turning and accelerating as it passes by the microstructure and also the wake region behind the microstructure. At height z_2 , the region directly behind the structure has nearly zero velocity, and a low velocity region extending for some distance beyond the zero velocity region. Height z_3 does not display a zero velocity region, but clearly depicts a wake region that extends beyond the farthest downstream measurement location. The wake is also observed at height z_4 , although it is not as prominent as at the lower measurement locations.

Figures 6.6(a) and 6.6(b) compare the streamwise velocity profiles between the experimental and numerical data for $Re_{D_h} = 108$. The velocity data have been normalized by the mean microchannel velocity u_{mean} based on the volumetric flowrate. Only one-half of the channel in the spanwise direction is shown due to flowfield symmetry, and position is normalized with respect to the channel width $W = 600 \mu\text{m}$. The experimental data are represented with symbols and the numerical simulations are represented with lines. As shown in Fig. 6.6(a), at 350 μm downstream of the microstructure each of the velocity profiles shown for depths z_2 through z_6 exhibit a maximum near $y/W = 0.3$ and a local minimum at the centerline, indicative of the presence of a wake. Examining the velocity profiles z_1 through z_5 , the velocity increases with increasing measurement location height, with maximum velocities occurring at height z_5 (the microchannel centerline). Similar trends are observed at 700 μm downstream of the microstructure. However, for height z_6 , the measured velocities are higher at a downstream distance of 350 μm than at 700 μm . This is an effect of the presence of the microstructure upstream, whereby

the flow is accelerated as it passes above and to the sides of the structure due to the reduction in microchannel cross-sectional area. After being initially accelerated by the constriction, the fluid at height z_6 then decelerates as downstream distance increases. This behavior at height z_6 is also observed in the other Reynolds numbers investigated. At $Re_{D_h} = 108$, the agreement between computation and experiment is excellent.

As the flowrate is increased, the wake becomes more pronounced, as shown in Fig. 6.7(a) for $Re_{D_h} = 216$ and a downstream distance of $350 \mu\text{m}$. The presence of the wake is most noticeable at $z_4 = 43 \mu\text{m}$ (a channel location corresponding to the height of the microstructure). At this height, that the streamwise velocity peaks near the microstructure edge ($y/W = 0.36$) and then decreases toward the channel centerline. At position z_6 , a channel location far above the position of the top of the microstructure, the wake effects are still observable. Further downstream of the microstructure at $700 \mu\text{m}$ (Fig. 6.7(b)), a velocity defect is no longer observed at heights at or below those corresponding to the microstructure height and it is only near the top of the microchannel that any evidence of a wake remains. Even at these measurement locations, the velocity defect is very small. At this Reynolds number, the experimental data and computational data once again show very good agreement.

The wake becomes much more prominent at $Re_{D_h} = 431$ (Figs. 6.8(a) and 6.8(b)). At a downstream distance of $350 \mu\text{m}$, the wake is especially noticeable at measurement locations at or below the height of the microstructure, and the two top measurement locations show no evidence of a velocity defect. However, at a downstream distance of $700 \mu\text{m}$, the wake is also observed at measurement location z_5 (the centerline of the channel), indicating that the wake is spreading upward as the flow propagates downstream. One consequence of the spreading of the wake is that the velocity defect at the lower measurement locations decreases between downstream distances of $350 \mu\text{m}$ and $700 \mu\text{m}$, as is shown in Figs. 6.8(a) and 6.8(b). Agreement between computation and experiment at this Reynolds number is good. There is a small discrepancy between

the computations and experiments at height z_2 in Fig. 6.8(a). At this location, the experiments and computations agree very well near the centerline of the channel, but moving from the centerline to the wall, the computations first underpredict and then overpredict the velocity compared to the experimental results.

Finally, for $Re_{D_h} = 1078$ the wake effects are highly pronounced, as shown in Fig. 6.9. At downstream distance $350 \mu\text{m}$ (Fig. 6.9(a)), there are two local peaks in the streamwise velocity, with the largest peak close to the channel centerline and a smaller, secondary peak closer to the channel wall. In addition, the profiles at or below the microstructure height (z_1 through z_4) exhibit a sharp decrease in the velocity magnitude at the centerline. With increasing downstream distance, Fig. 6.9(b) suggests that the wake is still dominant, extending to downstream distances far beyond those investigated in the microPIV experiments. Even at height z_6 , the velocity profile trends are not flat as with the other Re cases, indicating the residual presence of the wake. The experimental and numerical data are in good agreement, with some differences noticeable at the centerline. This and other small discrepancies noticed elsewhere are most likely due to difficulties in precisely determining the height of the measurement volume in the microPIV experiments.

The mean velocity results can also be rendered in three-dimensional contour plot form to provide a visualization of the flow around and downstream of the microstructure. Up to this point, velocity profiles have been shown at specific streamwise locations. Another point of view is a three-dimensional evolution of the flow for various planes in the streamwise direction. Figure 6.10 compares the experimental and simulated velocity flow fields at $Re_{D_h} = 216$ as contour plots of the streamwise velocity; the same velocity scale and dimensions are used in Fig. 6.10(a) and 6.10(b). As was shown previously in Fig. 6.7, the velocity fields are in very good agreement between experiments and computations. Furthermore, the planes near the microstructure show that the velocities are highest in regions just above the level of the structure and that the velocities decrease

in magnitude in the downstream direction.

Summary and Conclusion

A combined experimental-numerical effort was pursued to validate and substantiate microscale channel flows. Specifically, the channel was designed such that a microstructure protrudes from bottom surface of the channel wall. Arrays of such microstructures could be used in high heat flux applications to increase the surface-area-to-volume ratio, thus increasing heat transfer rates. Such microstructures may also prove useful in applications requiring rapid mixing such as microcombustion and microscale chemical processing.

The microchannel was fabricated using a rapid-prototyping photolithography technique with polydimethylsiloxane (PDMS). MicroPIV experiments were performed to measure the nearby velocity fields in the vicinity of the microstructure, for a range of Reynolds numbers. Three-dimensional numerical simulations were performed using FLUENT 6.0 to compare with the experimental results.

MicroPIV measurements taken downstream of the microstructure indicate the presence of a wake region downstream of the microstructure that grows more prominent with increasing flow rates, i.e., higher Reynolds numbers. The velocity profile trends indicate that as the flow passes the microstructure, the velocities increase in order to conserve mass for the incompressible flow. In particular, at cross-stream locations near the level of the microstructure height, the streamwise velocity magnitudes are largest. Another observed feature was that at the highest Reynolds number investigated, the wake downstream of the microstructure is most pronounced and there are two local peaks corresponding to regions of maximum velocity.

The numerical simulations were shown to be in excellent agreement with the experiments, thus validating the use of simulations as an additional tool in analyzing

flow features and providing data that can not otherwise be measured for microchannels and microstructures of the scale investigated in this study. Therefore, computational approaches can be used both to complement experiments and to provide additional flow field information that may be difficult to measure experimentally. The agreement between experiment and computations also confirm the viability of using CFD for determining optimal designs of microchannels with microstructures.

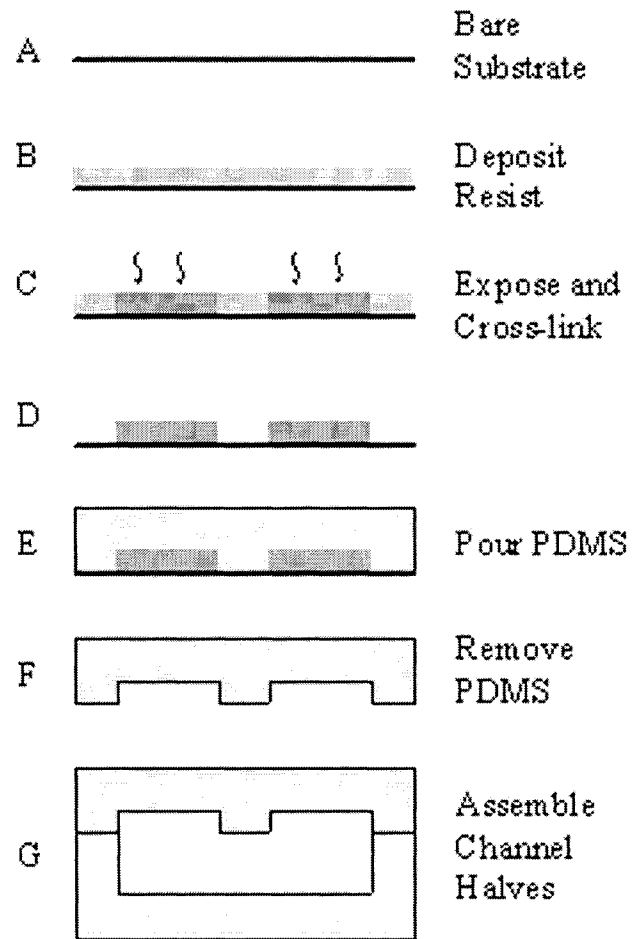


Figure 6.1 Mold and microchannel fabrication processes using PDMS. View is a cross-section of the $50\ \mu\text{m}$ half, cut through the microstructure.

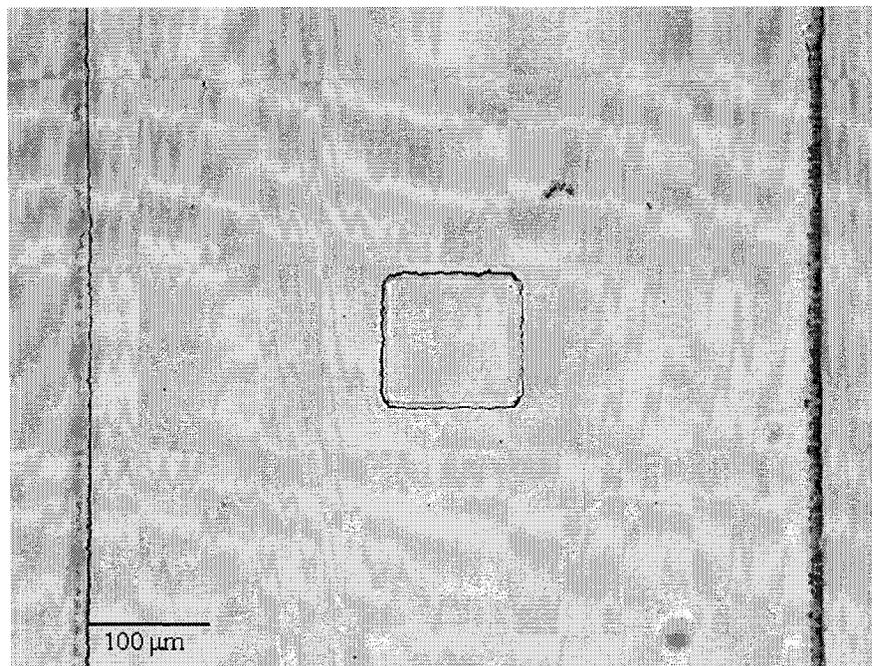


Figure 6.2 Overhead view of the microstructure in the microchannel.

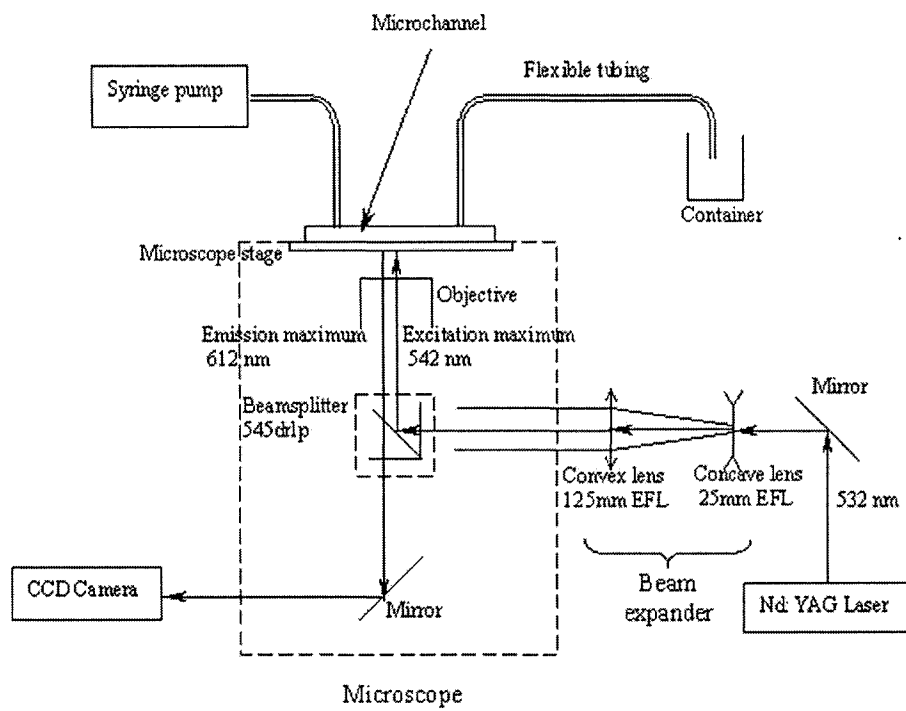


Figure 6.3 Schematic of the microPIV system

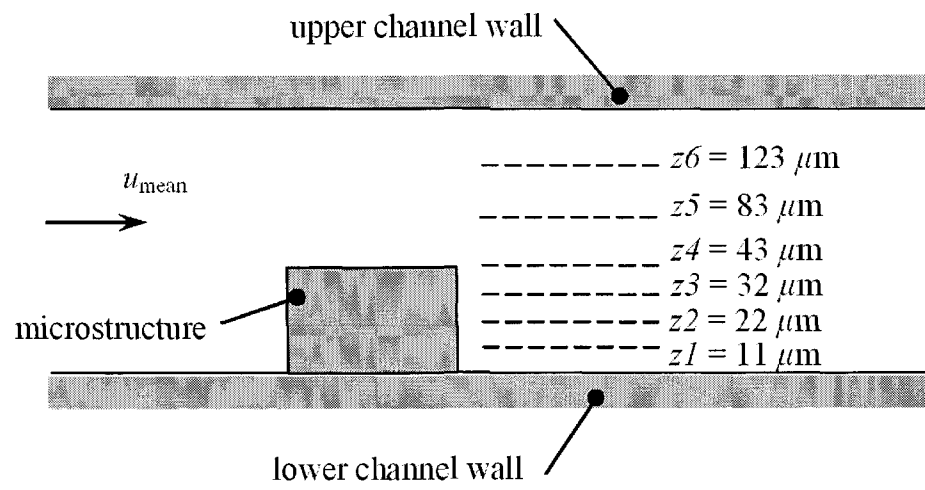


Figure 6.4 Locations of the velocity measurement planes in the microchannel

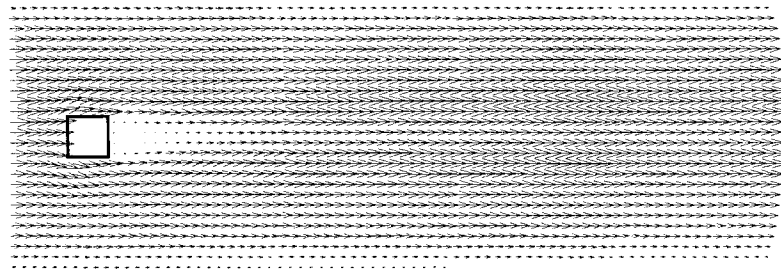
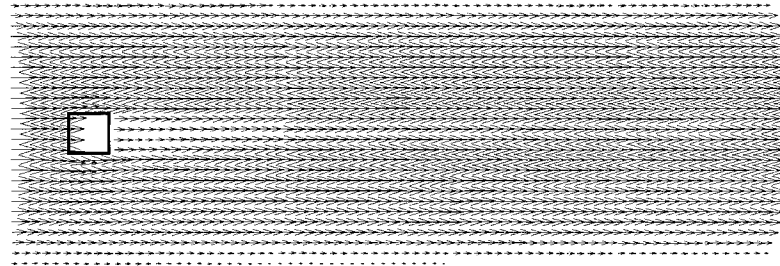
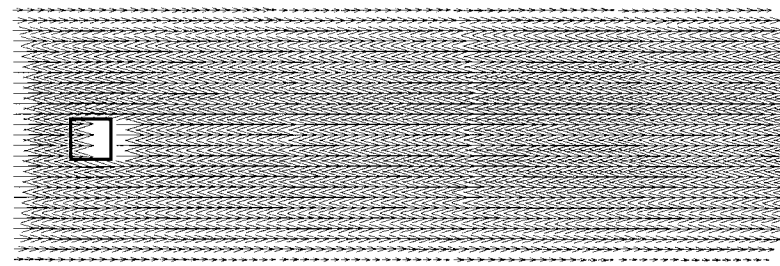
(a) $z_2 = 22 \mu\text{m}$ (b) $z_3 = 32 \mu\text{m}$ (c) $z_4 = 43 \mu\text{m}$

Figure 6.5 Velocity fields as measured by microPIV for at channel heights (every other vector shown)

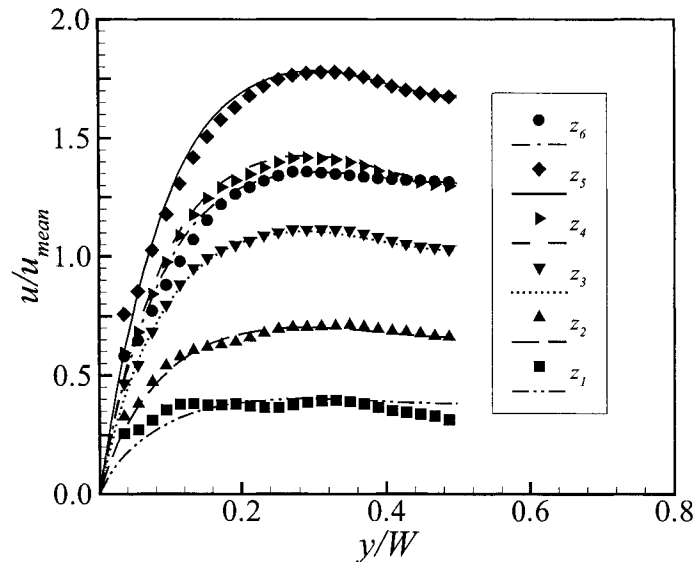
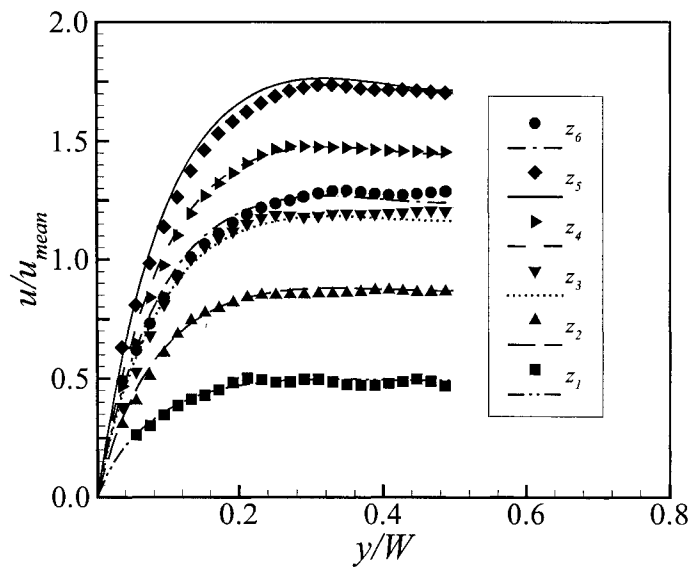
(a) $350 \mu\text{m}$ downstream of the microstructure(b) $700 \mu\text{m}$ downstream of the microstructure

Figure 6.6 Normalized streamwise velocity profiles for the microchannel at various depths for $Re_{D_h} = 108$ (Experiments - symbols; simulations - lines)

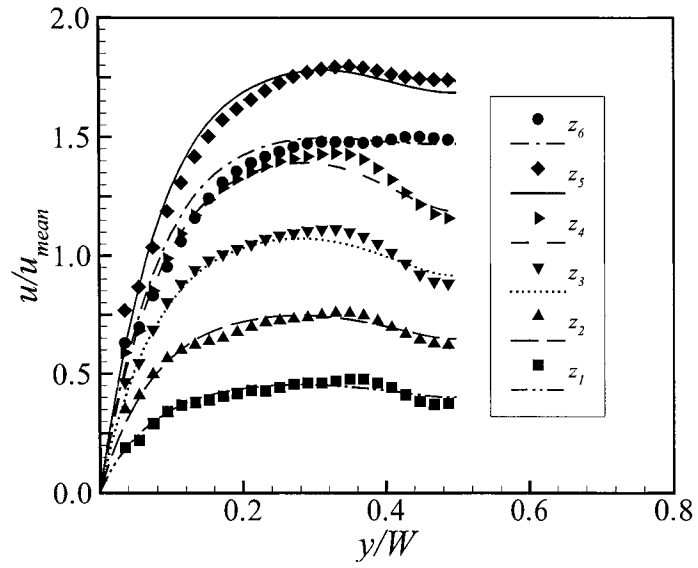
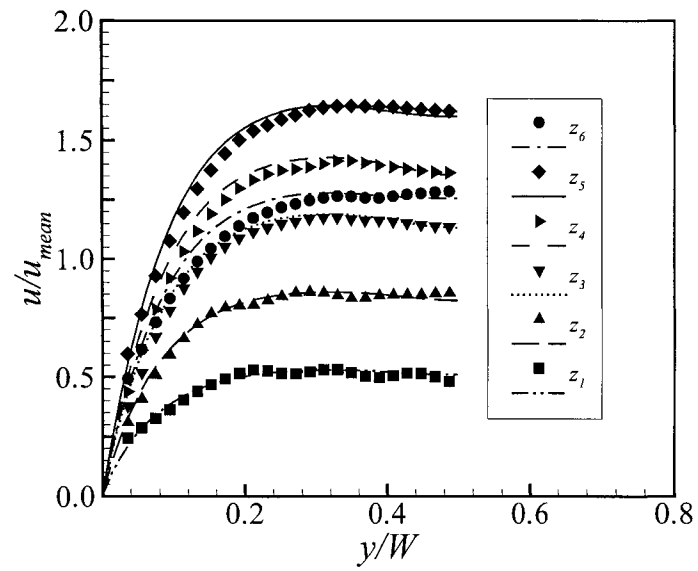
(a) $350 \mu\text{m}$ downstream of the microstructure(b) $700 \mu\text{m}$ downstream of the microstructure

Figure 6.7 Normalized streamwise velocity profiles for the microchannel at various depths for $Re_{D_h} = 216$ (Experiments - symbols; simulations - lines)

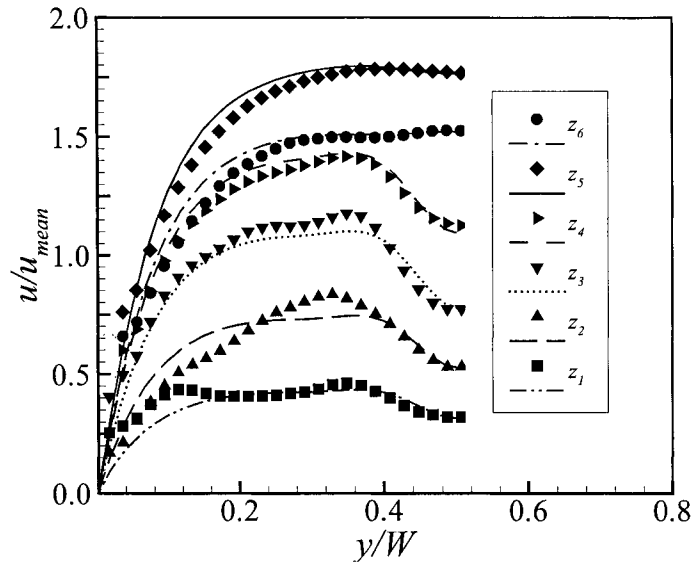
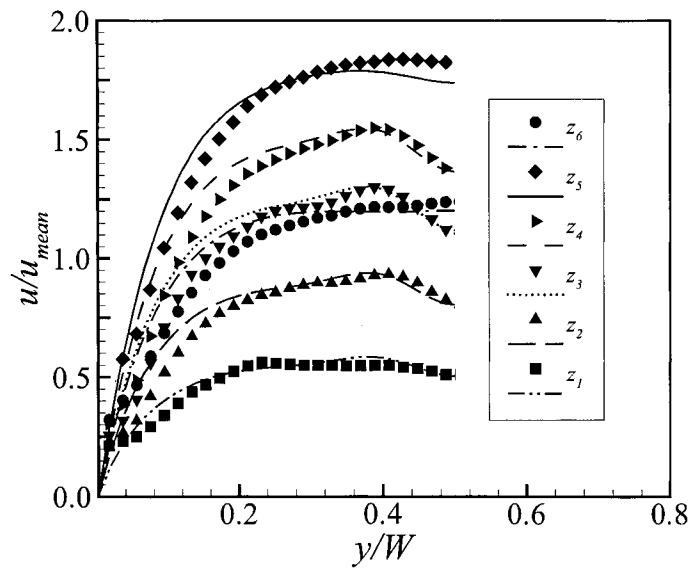
(a) $350 \mu\text{m}$ downstream of the microstructure(b) $700 \mu\text{m}$ downstream of the microstructure

Figure 6.8 Normalized streamwise velocity profiles for the microchannel at various depths for $Re_{D_h} = 431$ (Experiments - symbols; simulations - lines)

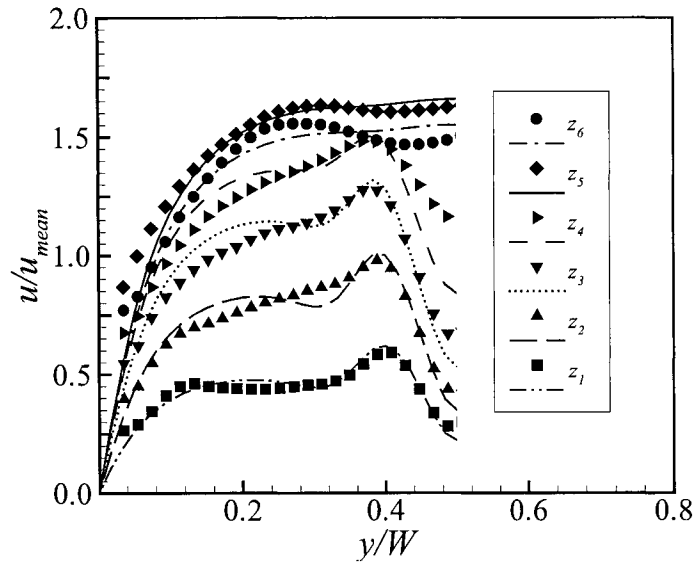
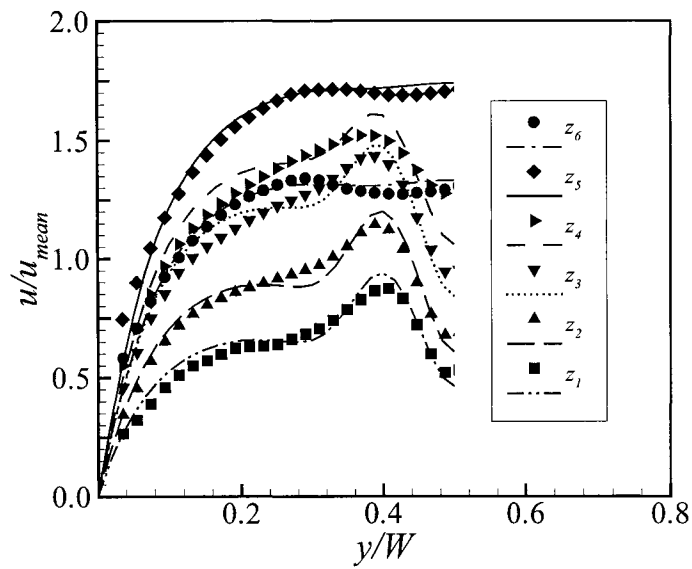
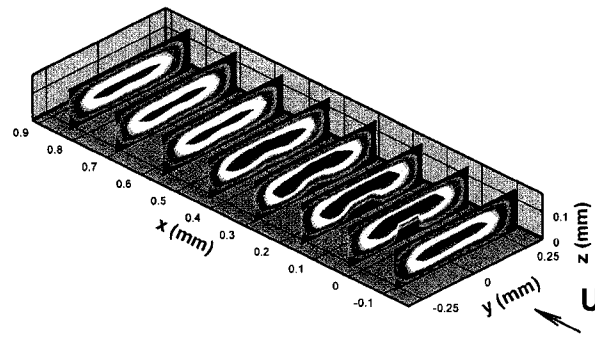
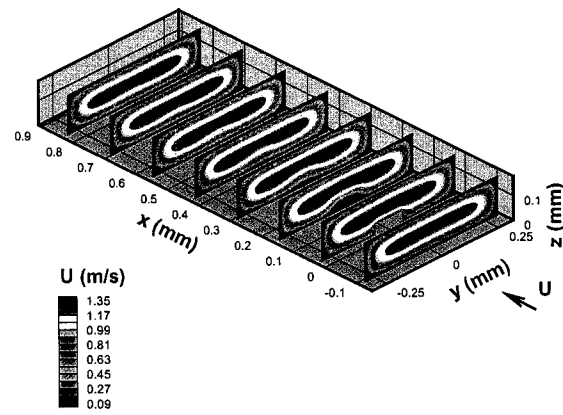
(a) $350 \mu\text{m}$ downstream of the microstructure(b) $700 \mu\text{m}$ downstream of the microstructure

Figure 6.9 Normalized streamwise velocity profiles for the microchannel at various depths for $Re_{D_h} = 1078$ (Experiments - symbols; simulations - lines)



(a) Experiments



(b) Simulations

Figure 6.10 Planes of streamwise velocity contours for $Re_{D_h} = 216$

CHAPTER 7 VELOCITY MEASUREMENTS OF LAMINAR AND TURBULENT FLOW IN RECTANGULAR MICROCHANNELS CONTAINING CUBIC MICROSTRUCTURES

A paper submitted to *Journal of Micromechanics and Microengineering*

H. Li and M. G. Olsen

Abstract

Microscopic particle image velocimetry (microPIV) was used to study the turbulent and transitional microfluidic flow in rectangular polydimethylsiloxane (PDMS) microchannels at cross section $600\ \mu\text{m}$ (W) \times $400\ \mu\text{m}$ (H). Different dimensions of single cubic microstructures with characteristic dimension 20, 40, and $50\ \mu\text{m}$ were designed at the center of the bottom wall. The flow data upstream and downstream the microstructure were captured using microPIV technique at Reynolds number 500, 1500, and 2500. The mean velocity profiles u/u_{max} and fluctuations u'/u_{max} indicated significant turbulence enhancement introduced by the man-made surface roughness.

Introduction

Microelectromechanical systems (MEMS) are an emerging technology that have applications in multiple areas of engineering and science. Microfluidic MEMS involve the

flow of liquid or gas through the device to accomplish its design purpose. Microfluidic MEMS often rely on rapid heat or mass transfer to operate most efficiently. For example, microscale heat exchangers used for heat sinks and cooling units application [Tuckerman and Pease (1981)] operate most effectively when heat transfer rates are maximized, and microscale combustion devices yield highest combustive efficiency when mixture of gas and oxygen is completely thorough. Similarly, chemical processing devices [Manz and Becker (1998)] and biological analysis devices [Mullis et al. (1994)] require sufficient mixing, reaction, and separation of fluids to improve yields and decrease required time and cost.

Microscale systems potentially have several characteristic advantages over macroscale devices, such as high surface-area-to-volume ratios, short diffusion distances, and small heat capacities, that serve to make heat transfer and mass transportation process more efficient than at the macroscale. These advantageous characteristics become more pronounced as the microfluidic devices become smaller. However, decreasing microchannel diameter in an effort to improve transport characteristics has one serious drawback: an increase in frictional losses, and consequently, pressure drop. The pressure drop required to drive a fluid through a microchannel is inversely proportional to the diameter to the fourth power; therefore, a small decrease in channel dimensions will require a larger increase in the power for pumping. Optimal design of a microfluidic device thus requires a careful balance of improving transfer characteristics and minimizing losses.

Instead of decreasing channel diameter, the surface-area-to-volume ratio of microchannels can also be increased by adding microstructures or microgrooves onto the interior channel walls [Khrustalev and Faghri (1999); Hopkins et al. (1999)]. Microstructures can increase the surface-area-to-volume ratio and help maintain smaller corresponding frictional losses than for smaller diameter microchannels with the same surface area-to-volume ratio. Furthermore, the microstructures may introduce secondary flows or turbulence into the fluid flow (similar to mixing tabs in macroscale flows) that can re-

sult in enhanced heat and mass transfer. For these reasons, the addition of arrays of microstructures into microchannels may be an efficient method to enhance heat transfer and mixing in analysis and engineering applications.

Despite their potential great importance in microfluidic applications, studies of flow in microchannels containing microfins or microgrooves have been limited to measurements of bulk fluid properties [Marques and Kelly (2004); Peles et al. (2005)], such as velocity and pressure drop, and a few computational fluid dynamics studies in the laminar regime [Peles et al. (2005); Croce and D'Agaro (2005); Hu et al. (2003); Aubin et al. (2005)]. The work presented here attempts to supplement these previous studies by using a non-intrusive method velocity measurement technique (Microscopic particle image velocimetry) to obtain detailed information about the flow characteristics in a microchannel containing a single microstructure. MicroPIV is a recently developed technique that has proven to be a useful technique for the study of fluid flow in microfluidic spanning the laminar regime [Santiago et al. (1998); Meinhart et al. (1999, 2000); Devasenathipathy et al. (2003); Stone et al. (2002)] through fully developed turbulent flow [Zeighami et al. (2000); Lee et al. (2002); Sharp and Adrian (2004); Hao et al. (2005); Li et al. (2005); Li and Olsen (2005, 2006)].

Particle image velocimetry (PIV) has been previously used to study flow in channels containing roughness elements (*i.e.*, bumps or fins) or ribs in macroscale geometries [Son et al. (2002); Shafiqul Islam et al. (2002)]. Son et al. (2002) performed PIV measurements on high-Reynolds number turbulent flow in a two-pass square channel for both a smooth wall and a 90° rib-roughened wall. Shafiqul Islam et al. (2002) investigated turbulent water flow through a channel of cross section 120 mm (W) x 24 mm (H) with 4-mm-high square-sectioned ribs at Reynolds number of 7000 and 20000. The experiment contained high resolution to show mean velocity, turbulent kinetic energy profiles, and rotating eddies downstream the ribs.

In the presented work, microPIV was used to obtain instantaneous velocity field

data for flow through rectangular microchannels containing a single cubic microstructure attached along the centerline of the bottom wall. The cross-sectional dimension of each microchannel is $600\ \mu\text{m} \times 400\ \mu\text{m}$ and the characteristic dimension of the attached microstructures ranged from $20\ \mu\text{m}$ to $50\ \mu\text{m}$. The particle seeding was dense enough that, in addition to mean velocity fields, velocity fluctuations and Reynolds stresses could be measured throughout the microchannel. The measurements were repeated for three different Reynolds numbers based on microchannel hydraulic diameter. The measured streamwise velocity profiles, fluctuations, and centerline velocity deficits are reported and discussed for three different depths within the microchannel. Where possible, the results are compared with previous results from macroscale studies and simulations.

Microchannel Fabrication and Experimental Procedure

Microchannel Fabrication

The microchannels used in the present experiments were fabricated using PDMS replica molding [Anderson et al. (2000); Jo et al. (2000)]. Channel molds were prepared with patterned negative photoresist (SU-8 2100, MicroChem Corp., Newton, MA) on Silicon wafers (100 mm diameter, Montco Silicon Technologies, Inc., Spring City, PA) using UV light photolithography. Two separate molds were fabricated, one containing the features of the microstructure and the other containing the features of the channel. Polydimethylsiloxane (PDMS) elastomer (Sylgard(R) 184 Silicone Elastomer Kit, Dow Corning, Midland, MI) was cast on the molds and baked. Finally, the two pieces of baked PDMS were plasma treated and bonded to form a complete microchannel. The fabrication process is summarized in Fig. 7.1.

A schematic of the microchannel geometries investigated is presented in Fig. 7.2. The dimensions of the microchannels were measured optically at various positions along the length of the microchannel, and these observations, accurate to within $\pm 10\ \mu\text{m}$, indicated

variations around 2%. The final length-averaged dimensions of the microchannels were measured by a microscope as $600\ \mu\text{m}$ (W) \times $400\ \mu\text{m}$ (H). A summary of the microchannel and microstructure geometries investigated in this study are listed in Table 7.1.

The microstructures were placed at locations far enough downstream of the microchannel entrance to ensure fully developed flow reaching the front edge of the microstructures and avoid any entrance length effects [Lee et al. (2002)]. This was verified by taking velocity measurements at different locations upstream of the microstructure and comparing the mean velocity profiles to ensure that a fully developed state had been achieved.

The resulting microchannels were then tested for inner surface roughness using Dektak IIA surface profile measuring system (Veeco Instruments Inc., Santa Barbara, CA). Linear surface profiles were taken of the cast PDMS. These measurements were limited, as the profilometer stylus could only be used on the top and bottom surfaces of the channel. The resulted relative roughness $\epsilon_s/D_h \approx 0.000074$, which is negligible compared to the roughness due to the microstructure.

Experimental Setup and Procedure

The experimental system used in the present experiments is the same that was used in previous studies [Li et al. (2005); Li and Olsen (2005, 2006)], and thus is only briefly described here. The flow system comprised of a closed loop with the flow driven by a micro gear pump and pump head that provided constant flow rates with accuracy of $\pm 0.3\%$. Flowrates were measured using a digital flowmeter (Cole-Parmer Instrument Co., Vernon Hills, IL). The flowmeter contained a thermocouple so fluid temperature could be carefully monitored during each run. A fluid reservoir was added to the flow loop to increase the thermal mass of the fluid in the system so that viscous dissipation did not result in any temperature change of the working fluid during the experimental runs. The working fluid was deionized water.

In the microPIV system, illumination was provided by a double pulsed Nd:YAG laser (Continuum, Santa Clara, CA). The laser beam was expanded and directed into an aperture in the rear of an inverted biological microscope (Nikon model T-300 Inverted Microscope). The flow was seeded with 820 nm diameter fluorescent seed particles (Duke Scientific Co., Palo Alto, CA) which emitted light at a peak emission wavelength of 612 nm. The excited light, filtered by a beamsplitter to remove illuminating and background light, was then imaged using an objective lens with 20X Magnification and a numerical aperture of 0.45. A LaVision Flowmaster 3 camera (LaVision Inc., Ypsilanti, MI) was used to capture the PIV image pairs for cross-correlation analysis.

The experiments were performed at various flowrates corresponding to Reynolds numbers based on microchannel hydraulic diameter of 500, 1500, and 2500. For each Reynolds number, the velocity measurements were performed at three heights, $z = a/2$, a , and $H/2$ above the bottom wall of the microchannels and also at various locations downstream of the microstructures. A multi-pass interrogation scheme with decreasingly smaller window sizes was used in the computation of the vector fields to reach the final 32 x 32 pixels interrogation windows. Interrogation windows were overlapped by 50% yielding an in plane vector spacing of 12.8 μm . The number of velocity fields collected for each case investigated is 1000.

The concentration of the fluorescent particle solution was prepared such that a sufficient number of seed particles fell within depth of correlation [Olsen and Adrian (2000b); Bourdon et al. (2004)] of each interrogation region that erroneous vector measurements were minimized. In the present experiments, the 20X 0.45 NA microscope objective yields a depth of correlation of 8.3 μm . Achieving this spatial resolution required a volumetric particle concentration of approximately 0.057%. This volume fraction of seed particles was small enough that any two-phase effects are negligible, and the working fluid could be considered a single-phase fluid.

There are two sources of measurement errors in the microPIV experiments: errors im-

implicit in the interrogation of the PIV images, and errors introduced by random motion of the seed particles due to Brownian motion. The experimental error due to interrogation of the PIV images can be estimated by assuming that measured particle displacements are accurate to within approximately 1/10th of a seed particle image diameter [Prasad et al. (1992)]. The effective particle diameter when projected back into flow coordinates at $1.96 \mu\text{m}$, meaning that the measured particle displacement in the microPIV experiments should be accurate to within $0.196 \mu\text{m}$. For the present experiments, the particles moved approximately $8 \mu\text{m}$ between laser pulses, resulting in an experimental uncertainty of 2.45%.

One way to estimate the significance of Brownian motion in the microPIV measurements can be determined by calculating the Brownian motion parameter [Olsen and Adrian (2000a)]. For values of the Brownian motion parameter close to unity, Brownian motion has a negligible effect on the measured velocity. For flow in the microchannel at $Re = 500$, the Brownian motion coefficient is equal to 0.9999, indicating that Brownian motion effects are small. For higher Reynolds numbers in all the three microchannel, the Brownian motion effect is even smaller, due to the smaller Δt required for these measurements. Note that the fact that Brownian motion is negligible is not surprising, given the short Δt required for each of the measurements (on the order of 1 microsecond).

The relative unimportance of the error due to Brownian motion can also be demonstrated by comparing the particle displacement due to particle diffusion with the uncertainty in determining particle displacement. The distance that a particle is expected to diffuse due to Brownian motion can be found using

$$s = \sqrt{2D\Delta t} \quad (7.1)$$

For $Re = 2500$, the rms particle displacement due to Brownian motion is $0.001 \mu\text{m}$, which is only 0.5% of the experimental error. Thus, the effects of Brownian motion can

be safely neglected.

Results and Discussion

For each of the fabricated microchannels containing microstructures, ensemble-averaged streamwise velocity profiles and streamwise velocity fluctuation profiles were obtained far upstream of the microstructure and at three downstream locations, $l = 3a, 5a$ and $9a$, where l is the distance downstream from the trailing edge of microstructure. Moreover, profiles were obtained for each of these locations at three different depths in the microchannel: $z = H/2$, (the midplane of the microchannel), $z = a$ (a plane located one microstructure height from the bottom wall), and $z = a/2$ (a plane located one-half of a microstructure height from the bottom wall). The locations of these different planes are determined by focusing on the top and bottom surfaces of the microchannel to locate the top and bottom walls, and then moving the focal plane of the microscope to the desired depth using the control knob of the translation stand. The accuracy of the location of the focal plane is estimated to be within $2 \mu\text{m}$. In all of the plots presented in this work, the transverse positions of data are normalized by $1/2$ of the width of the microchannel; thus, 0 corresponds to the microchannel centerline and 1 corresponds to the microchannel side wall. Meanwhile, the streamwise velocities u and fluctuations u' are normalized by the upstream peak velocity at the midplane.

Microchannel Containing the $20 \mu\text{m} \times 20 \mu\text{m} \times 20 \mu\text{m}$ Microstructure

Streamwise velocity and fluctuation profiles for $Re = 500$ in the microchannel containing the $20 \mu\text{m} \times 20 \mu\text{m} \times 20 \mu\text{m}$ microstructure are shown in Fig. 7.3. Upstream of the microstructure (Fig. 7.3(a)), the velocity profile at $z = H/2$ is parabolic, as expected for laminar channel flow. At the two measurement depths investigated, $z = a$ and $z = a/2$, a parabolic shape is also observed, but the peak velocities are much lower

than at $z = H/2$ due to the short physical distance from the bottom wall (10 μm and 20 μm , respectively), where the no-slip condition requires the velocity to be zero. The nearly perfect parabolic profiles observed in Fig. 7.3 also demonstrate that the upstream measurement location is far enough downstream that the effect of the entrance length is negligible [Lee et al. (2002)]. The measured streamwise velocity fluctuations, u'/u_{max} , upstream of the microstructure are low, typically around 2-3% at all measurement locations. These fluctuations are not indicative of turbulence, but instead represent the experimental error in the experiment. Indeed, the fluctuation values shown in Fig. 7.3(a) agree very well with the estimated experimental error of 2.45%. Note that u'/u_{max} is higher near the walls of the microchannel. This is to be expected, since the experimental error in microPIV is inversely proportional to the distance that seed particles move between the two image frames. Since particles near the wall move more slowly than particles near the center of the microchannel, and hence move shorter distances between laser pulses, the experimental error will be higher near the walls.

As the fluid flow passes over the microstructure and moves downstream, there is very little change in the mean velocity along the centerline at $z = H/2$ at either $l = 3a$ (Fig. 7.3(b)), $l = 5a$ (Fig. 7.3(c)), or $l = 9a$ (Fig. 7.3(d)), indicating that because of the small dimensions of the microstructure and long physical distance between the planes of $H/2$ and a , the effects of the microstructure on the mean velocity are nearly insignificant at $z = H/2$. An increase in u'/u_{max} is observed at all three l locations for $z = H/2$, however, due to vortices generated at the trailing edge of the microstructure.

The wake downstream of the microstructure is noticeable at $z = a$ and $z = a/2$, although even at these depths, evidence of the wake has disappeared at $l = 9a$. An increase in u'/u_{max} is also observed downstream of the microstructure at $z = a$ and $z = a/2$, and the increase is greater than that observed at $z = H/2$. At a depth of $z = a$, $u'/u_{max} = 0.07$ near the channel centerline at $l = 3a$, and steadily decreases to about 0.05 at $l = 9a$. Centerline values of u'/u_{max} for $z = H/2$, are $u'/u_{max} = 0.07$ at $l = 3a$

decreasing to $u'/u_{max} = 0.06$ at $l = 9a$. Centerline fluctuation values for $z = a/2$ are slightly lower than those observed for $z = a$ and $z = H/2$. At each measurement depth, u'/u_{max} decreases with increasing downstream distance from the microstructure. This is not surprising since the vortices generated by the microstructure are expected to weaken with increasing downstream distance due to viscous effects. The centerline velocity fluctuations for the microchannel containing this microstructure are summarized in Table 7.2 along with the centerline velocity fluctuations for the microchannels containing the larger microstructures.

It is interesting to note that the velocities at $z = a/2$ and $z = a$ downstream of the microstructure are greater than those at the same channel depths upstream of the microstructure. This is because the vortices formed downstream of the microstructure improve the three-dimensional momentum transport compared to the laminar flow upstream of the microstructure, and, in turn, result in increased velocities near the walls. The resulting velocity profile is “fuller” downstream of the microstructure, just like it would be in turbulent channel flow.

The measurements were repeated in the microchannel with the $20\ \mu\text{m} \times 20\ \mu\text{m} \times 20\ \mu\text{m}$ microstructure at higher Reynolds numbers, and these results are shown in Figs. 7.4 and 7.5. The results upstream of the microstructure for $Re = 1500$ are shown in Fig. 7.4(a). The mean velocity profile for $Re = 1500$ is fuller than the mean velocity profile for $Re = 500$. While this result may suggest the onset of early transition to turbulence, this is not necessarily true, since deviations in the measured mean velocity profile from the analytical laminar solution have been found to occur in both macroscale [Wyganski and Champagne (1973)] and microscale [Sharp and Adrian (2004); Li and Olsen (2005, 2006)] channel flows before any other evidence of transition (such as increases in rms velocity fluctuations) is observed. A better definition of transition is an increase in the measured velocity fluctuations. The measured velocity fluctuations at $z = H/2$ for $Re = 1500$ are still only approximately 2.5% (nearly equal to the experimental error),

and thus there is no evidence of transition to turbulence at this Reynolds number. This result is consistent with earlier microPIV studies in which transition to turbulence in microchannels was observed at Reynolds numbers between 1800 and 2000 [Sharp and Adrian (2004); Li and Olsen (2005, 2006)].

Just as at $Re = 500$, there is very little change in the mean velocity along the centerline downstream of the microstructure at $z = H/2$ and $l = 3a$ (Fig. 7.4(b)), $l = 5a$ (Fig. 7.4(c)), and $l = 9a$ (Fig. 7.4(d)). The presence of the wake is much more prominent at $z = a$ and $z = a/2$, and even at $l = 9a$, the velocity deficit near the channel centerline is prominent. Just as for $Re = 500$, there is a sharp increase in u'/u_{max} downstream of the microstructure due to the presence of vortices shed from the microstructure. These increases may also be due to the microstructure temporarily tripping the flow to turbulent downstream of the microstructure. The flow is expected to be laminar at $Re = 1500$, but this is close to the transitional Reynolds number, and thus the strong disturbances introduced by the microstructure may cause this temporary premature transition. The measured downstream velocity fluctuations for $Re = 1500$ are much larger than those observed for $Re = 500$.

At a depth of $z = a$, $u'/u_{max} = 0.11$ near the channel centerline at $l = 3a$, decreasing to about 0.10 at $l = 9a$. Centerline values of u'/u_{max} are lower for $z = H/2$, with u'/u_{max} between 0.08 and 0.09 observed at all three downstream measurement locations. The centerline fluctuation values for $z = a/2$ are slightly lower than those at $z = a$. The velocities at $z = a/2$ and $z = a$ downstream of the microstructure are once again observed to be greater than those in at the same channel depths upstream of the microstructure due to the increase in momentum transport due to the vortices in the flow.

The results upstream of the microstructure for $Re = 2500$ are shown in Fig. 7.5(a). Here the mean velocity profile is even fuller than the mean velocity profile for $Re = 1500$ and closely resembles the velocity profiles for fully turbulent microchannel flow observed

in previous studies [Li and Olsen (2005, 2006)]. Centerline velocity fluctuation values for $z = H/2$ are approximately 5%, increasing to approximately 10% in regions close to the microchannel walls. These values also agree well with previous results for fully turbulent microchannel flow [Li and Olsen (2005, 2006)].

Again, there is no evidence of the wake downstream of the microstructure at a depth of $z = H/2$. It is only in the measurement planes closer to the microchannel lower wall where the wake becomes noticeable. There is a sharp increase in u'/u_{max} downstream of the microstructure, and these fluctuation values are even greater than those observed at $Re = 1500$. At a depth of $z = a$, $u'/u_{max} = 0.20$ near the channel centerline at $l = 3a$, decreasing to about 0.13 at $l = 9a$. Centerline values of u'/u_{max} are generally lower for $z = H/2$, with $u'/u_{max} = 0.15$ at $l = 3a$ decreasing to $u'/u_{max} = 0.14$ at $l = 9a$. The centerline fluctuation values for $z = a/2$ are similar to those at $z = a$. These increases in velocity fluctuation increase momentum transport, resulting in the mean velocities at $z = a/2$ and $z = a$ that are greater than those observed upstream of the microstructure.

Microchannel Containing the $40 \mu\text{m} \times 40 \mu\text{m} \times 40 \mu\text{m}$ Microstructure

The experiments were then repeated at all three Reynolds numbers for a microchannel containing a microstructure measuring $40 \mu\text{m} \times 40 \mu\text{m} \times 40 \mu\text{m}$. Streamwise velocity and fluctuation profiles at $Re = 500$ for this microchannel are shown in Fig. 7.6. Although the flow far upstream of the microstructure should be identical to that observed for microchannel with the smaller microchannel, the results for the upstream flow at $Re = 500$ for the microchannel containing the larger microstructure are shown in Fig. 7.6(a) for the purpose of demonstrating the repeatability of the present measurements. Indeed, excellent agreement is observed between these results and those shown in Fig. 7.3(a), as one would expect.

Even though the dimensions of this microstructure are twice as large as the smaller microstructure, there is still no evidence of a wake observed in the mean velocity along

the centerline at $z = H/2$ and $l = 3a$ (Fig. 7.6(b)), $l = 5a$ (Fig. 7.6(c)), or $l = 9a$ (Fig. 7.6(d)). However, the wake is observable at $z = a$ and $z = a/2$. As with the smaller microstructure, an increase in u'/u_{max} is observed at all three l locations for $z = H/2$.

The measured velocity fluctuations for this microstructure at $Re = 500$ agree remarkably well with those observed for the smaller microstructure. At a depth of $z = a$, u'/u_{max} is approximately 0.10 near the channel centerline at $l = 3a$, and decreases to about 0.08 at $l = 9a$. Centerline values of u'/u_{max} are lower for $z = H/2$, with $u'/u_{max} = 0.06$ at $l = 3a$ and remaining close to this value at the other downstream locations investigated. The centerline fluctuation values for $z = a/2$ are similar to those observed at $z = H/2$.

As with for the microchannel containing the smaller microstructure, the measurements were repeated in the microchannel with the $40 \mu\text{m} \times 40 \mu\text{m} \times 40 \mu\text{m}$ microstructure at higher Reynolds numbers, and these results are shown in Figs. 7.7 and 7.8. The results upstream of the microstructure for $Re = 1500$ are shown in Fig. 7.7(a). Downstream of the microstructure, there is very little change in the mean velocity along the centerline at $z = H/2$. The presence of the wake is only observed at $z = a$ and $z = a/2$, and at these depths, a prominent wake is observed at all three downstream measurement locations $l = 9a$. Just as for $Re = 500$, there is a sharp increase in u'/u_{max} downstream of the microstructure.

The downstream velocity fluctuations for $Re = 1500$ are much higher than those observed for $Re = 500$. At a depth of $z = a$, $u'/u_{max} = 0.15$ near the channel centerline at $l = 3a$, decreasing to about 0.12 at $l = 9a$. Centerline values of u'/u_{max} are lower for $z = H/2$, with $u'/u_{max} = 0.13$ at $l = 3a$ decreasing to $u'/u_{max} = 0.10$ at $l = 9a$. The centerline fluctuation values for $z = a/2$ are in general similar to those observed at $z = H/2$. These results also compare well to those observed for the microchannel with the $20 \mu\text{m} \times 20 \mu\text{m} \times 20 \mu\text{m}$ microstructure for $Re = 1500$, especially at $l = 5a$ and $l = 9a$, where the results match almost exactly. The mean velocities at $z = a/2$

and $z = a$ downstream of the microstructure are once again observed to be greater than those at the same channel depths upstream of the microstructure due to the increase in momentum transport due to the vortices in the flow.

The results upstream of the microstructure for $Re = 2500$ are shown in Fig. 7.8(a). Just as at the lower Reynolds numbers, there is no evidence of the wake downstream of the microstructure at a depth of $z = H/2$, and the wake only becomes noticeable in the measurement planes closer to the microchannel lower wall. There is a sharp increase in u'/u_{max} downstream of the microstructure, and these fluctuation values are once again even greater than those observed at $Re = 1500$. At a depth of $z = a$, $u'/u_{max} = 0.21$ near the channel centerline at $l = 3a$, decreasing to 0.16 at $l = 9a$. Centerline values of u'/u_{max} for $z = H/2$ are similar to those observed for the smaller microstructure, with $u'/u_{max} = 0.17$ at $l = 3a$ decreasing to $u'/u_{max} = 0.13$ at $l = 9a$. The centerline values at $z = a/2$ are somewhat lower than those observed for the smaller microstructure, with $u'/u_{max} = 0.12$ at $l = 3a$ increasing to $u'/u_{max} = 0.14$ at $l = 9a$. However, keep in mind that small errors in the location of the measurement plane are likely have the most significant effects in these near wall locations, especially for the microchannel containing the $20 \mu\text{m} \times 20 \mu\text{m} \times 20 \mu\text{m}$ microstructure. The observed discrepancy in the data at $z = a/2$ is therefore most likely due to some error in the estimation of the location for the measurement plane for the $Re = 2500$ experiments in the microchannel containing the $20 \mu\text{m} \times 20 \mu\text{m} \times 20 \mu\text{m}$ microstructure. Once again, the observed increases in velocity fluctuations compared to $Re = 500$ increase momentum transport, although the resulting increases in the mean velocities at $z = a/2$ and $z = a$ that are smaller than those observed downstream of the smaller microstructure for this Reynolds number.

Microchannel Containing the $50 \mu\text{m} \times 50 \mu\text{m} \times 50 \mu\text{m}$ Microstructure

Finally, the experiments were repeated for a microchannel containing a microstructure measuring $50 \mu\text{m} \times 50 \mu\text{m} \times 50 \mu\text{m}$. Streamwise velocity and fluctuation profiles

at $Re = 500$ for this microchannel are shown in Fig. 7.9. The upstream results for all three Reynolds numbers investigated agree well with the measurements upstream of the $20 \mu\text{m} \times 20 \mu\text{m} \times 20 \mu\text{m}$ and $40 \mu\text{m} \times 40 \mu\text{m} \times 40 \mu\text{m}$ microstructures, as one would expect.

Despite the fact that this is the largest microstructure investigated, there is still no evidence of a wake observed in the mean velocity along the centerline at $z = H/2$ and $l = 3a$ (Fig. 7.9(b)), $l = 5a$ (Fig. 7.9(c)), or $l = 9a$ (Fig. 7.9(d)). However, the wake is observable at $z = a$ and $z = a/2$. As with the smaller microstructure, an increase in u'/u_{max} is observed at all three l locations for $z = H/2$.

The measured velocity fluctuations for this microstructure at $Re = 500$ agree well with those observed behind the $40 \mu\text{m} \times 40 \mu\text{m} \times 40 \mu\text{m}$ microstructure. At a depth of $z = a$, u'/u_{max} is approximately 0.08 near the channel centerline at $l = 3a$, and decreases to about 0.05 at $l = 9a$. Centerline values of u'/u_{max} are lower for $z = H/2$, with $u'/u_{max} = 0.05$ at $l = 3a$ and remaining close to this value at the other downstream locations investigated. The the centerline fluctuation values for $z = a/2$ are similar to those observed for the $40 \mu\text{m} \times 40 \mu\text{m} \times 40 \mu\text{m}$ microstructure, except at $l = 3a$, where the centerline value of u'/u_{max} is only 0.02, compared to 0.06 for the $40 \mu\text{m} \times 40 \mu\text{m} \times 40 \mu\text{m}$ microstructure.

The downstream velocity fluctuations for $Re = 1500$ are again higher than those observed for $Re = 500$. At a depth of $z = a$, $u'/u_{max} = 0.13$ near the channel centerline at $l = 3a$ decreasing to 0.08 at $l = 9a$. Centerline values of u'/u_{max} for $z = H/2$, are $u'/u_{max} = 0.07$ at $l = 3a$ and remain fairly constant at the further downstream locations. The centerline fluctuation values for $z = a/2$ remain between 0.10 and 0.09 at all three downstream locations.

For $Re = 2500$, there is a sharp increase in u'/u_{max} downstream of the microstructure, with fluctuation values greater than those observed at $Re = 1500$. At a depth of $z = a$, $u'/u_{max} = 0.17$ near the channel centerline at $l = 3a$, increasing to only 0.16 at

$l = 9a$. Centerline values of u'/u_{max} for $z = H/2$ are $u'/u_{max} = 0.18$ at $l = 3a$ decreasing to $u'/u_{max} = 0.15$ at $l = 9a$. The lowest centerline values of u'/u_{max} are observed at $z = a/2$, with u'/u_{max} between 0.14 and 0.15 at all three downstream measurement locations. These results at $Re = 2500$ agree very well with those observed in the microchannel with the $40 \mu\text{m} \times 40 \mu\text{m} \times 40 \mu\text{m}$ microstructure. Note especially the agreement at $z = a/2$, lending further evidence that the abnormally high velocity fluctuations observed downstream of the smallest microstructure at this depth are an indication of an error in locating the focal plane depth.

Velocity Deficit Results

Finally, the centerline velocity deficit results downstream the microstructures are presented in Fig. 7.12. Instead of being normalized the velocities by the upstream peak velocities as Fig. 7.3 through Fig. 7.11, the data are normalized by the upstream maximum velocities at each local depth in order to observe the wake length at each depth; thus, 0 corresponds for the data at the local depth maximal velocities, while 1 corresponds velocities at 0 m/s.

For microchannel with $20 \mu\text{m} \times 20 \mu\text{m} \times 20 \mu\text{m}$, the centerline velocity deficit right behind the microstructure is 0.9 at $z = a/2$ and $Re = 500$, shown in Fig. 7.12(a). As the flow goes farther, the value decreases approaching 0.0 at the length over $8a$. The same behavior can be observed for the velocity deficit at $z = a$ and the same Reynolds number. As Reynolds number increases, the velocity deficits shows a quicker tendency approaching 0.0 and a shorter wake length, which is due to the significant turbulence. It is interesting to note that there is no similar distinguishable behavior for the data at $z = H/2$, which agrees well with the results by observing the plots at velocity profiles in Fig. 7.3 where there is no wake velocity profiles at $z = H/2$ as well.

The centerline velocity deficits in microchannel with $40 \mu\text{m} \times 40 \mu\text{m} \times 40 \mu\text{m}$, in Fig. 7.12(b), shows the similar dependence of the variation of velocity and wake

length on the downstream location and Reynolds number. Compared with Fig. 7.12(a), the wake length is even shorter which could be explained as the enhanced turbulence introduced by larger microstructure, especially for the data at $z = a$. Again, the data at $z = H/2$ do not show considerable wake effect. At far downstream location (over $6a$), the velocity deficits show fluctuation around 0.0 which is not observable in microchannel microchannel with $40 \mu\text{m} \times 40 \mu\text{m} \times 40 \mu\text{m}$. This behavior might be due to more turbulence attributed by the larger microstructure.

In the data of microchannel with $50 \mu\text{m} \times 50 \mu\text{m} \times 50 \mu\text{m}$ in Fig. 7.12(c), the centerline velocity deficits drop much more faster than the other two channels. However, there is still no persuasive evidence to show the wake at $z = H/2$. The wake length at $z = a$ and $z = a/2$ and the fluctuation of the velocity deficits at $l > 4a$ demonstrated the enhanced turbulence due to the larger microstructure.

Summary and Conclusions

Microscopic particle image velocimetry was used to measure instantaneous velocity fields in microchannels containing a single cubic microstructure attached to the bottom wall. The microchannels had cross-sectional areas of $600 \mu\text{m}$ (W) \times $400 \mu\text{m}$ (H). Three different cubic microstructure dimensions were investigated: $20 \mu\text{m} \times 20 \mu\text{m} \times 20 \mu\text{m}$, $40 \mu\text{m} \times 40 \mu\text{m} \times 40 \mu\text{m}$, and $50 \mu\text{m} \times 50 \mu\text{m} \times 50 \mu\text{m}$. Measurements were performed far upstream of the microstructure to characterize the incoming flow, and also at three different downstream locations. Moreover, data were collected for each of these positions at three different depths in the microchannel ranging from the channel centerline ($z = H/2$) to a locations halfway between the bottom wall and the top of the microstructure ($z = a/2$). The experiments were performed for Reynolds numbers equal to 500, 1500, and 2500 based on microchannel hydraulic diameter and mean velocity.

The upstream results suggested that the incoming flow was laminar for the $Re = 500$

and 1500 cases, but was turbulent for the $Re = 2500$ cases. The measured mean velocity and velocity fluctuation results upstream of the microstructures are in agreement with previous experiments in microchannel flows as well as classical macroscale results.

In general, excellent agreement was observed in the results for all three microstructure sizes. Some discrepancies were observed in the results for $z = a/2$, but these are most likely due to the difficulty of precisely locating the measurement plane close to the microchannel bottom wall. No evidence of a wake is seen in the mean velocity field measurements along the midplane of the channel. It is only at the two near wall measurement locations ($z = a$ and $z = a/2$) that evidence of the wake is clearly observed. The centerline velocity deficits shows the dependence of the wake length on the Reynolds number and downstream distance. Again, there is no evidence of a wake according to the velocity deficits at the midplane of the channel. The introduction of larger microstructure causes more significant 3D momentum transport and turbulence resulting in shorter wake length according to the velocity deficits.

For $Re = 500$, an increase in u'/u_{max} is observed downstream of the microstructure due to vortices generated at the trailing edge of the microstructure. This increase in velocity fluctuations results in greater three-dimensional momentum transport than in the laminar flow upstream of the microstructure, and thus the velocity profiles for the near wall locations downstream display higher velocity, indicating that the velocity field is “fuller”, more closely resembling velocity fields in turbulent microchannel flow. The velocity fluctuations are generally greatest at channel depth $z = a$. The velocity fluctuations decrease with increasing downstream distance from the microstructure due to viscous effects.

For $Re = 1500$, the increase in u'/u_{max} is greater than that observed at $Re = 500$. These increases also result in a fuller velocity profile than was observed upstream of the microstructure. Once again, the observed velocity fluctuations are greatest at $z = a$ and also decrease with increasing downstream distance from the microstructure due to

viscous effects.

The greatest increase in u'/u_{max} is observed at $Re = 2500$. Just as at the lower Reynolds numbers, the mean velocities at the near wall positions increase, but this increase is small compared to the increases observed at $Re = 500$ and $Re = 1500$ due to the incoming flow already being turbulent. Here, too, the velocity fluctuations are generally highest at depth $z = a$ and decrease with increasing downstream distance.

Table 7.1 Geometric parameters of test microchannels and microstructures

Channel Name	Channel Dimension $W (\mu\text{m}) \times H (\mu\text{m})$	Microstructure Dimension $a (\mu\text{m}) \times a (\mu\text{m}) \times a (\mu\text{m})$
Channel 1	600 x 400	20 × 20 × 20
Channel 2	600 x 400	40 × 40 × 40
Channel 3	600 x 400	50 × 50 × 50

Table 7.2 Summary of normalized centerline velocity fluctuations u'/u_{max}

Microstructure size	Re	$z = H/2$			$z = a$			$z = a/2$		
		$l = 3a$	$l = 5a$	$l = 9a$	$l = 3a$	$l = 5a$	$l = 9a$	$l = 3a$	$l = 5a$	$l = 9a$
$20 \mu\text{m} \times 20 \mu\text{m} \times 20 \mu\text{m}$	500	0.07	0.08	0.06	0.07	0.06	0.05	0.05	0.05	0.04
	1500	0.08	0.09	0.08	0.11	0.10	0.10	0.10	0.09	0.09
	2500	0.15	0.15	0.14	0.20	0.17	0.13	0.20	0.17	0.17
$40 \mu\text{m} \times 40 \mu\text{m} \times 40 \mu\text{m}$	500	0.06	0.05	0.05	0.10	0.09	0.08	0.06	0.06	0.05
	1500	0.13	0.09	0.10	0.15	0.13	0.12	0.09	0.09	0.10
	2500	0.17	0.15	0.13	0.21	0.17	0.16	0.12	0.12	0.14
$50 \mu\text{m} \times 50 \mu\text{m} \times 50 \mu\text{m}$	500	0.05	0.05	0.04	0.08	0.07	0.05	0.02	0.05	0.04
	1500	0.07	0.06	0.07	0.13	0.10	0.08	0.10	0.09	0.09
	2500	0.18	0.17	0.15	0.17	0.17	0.16	0.14	0.14	0.15

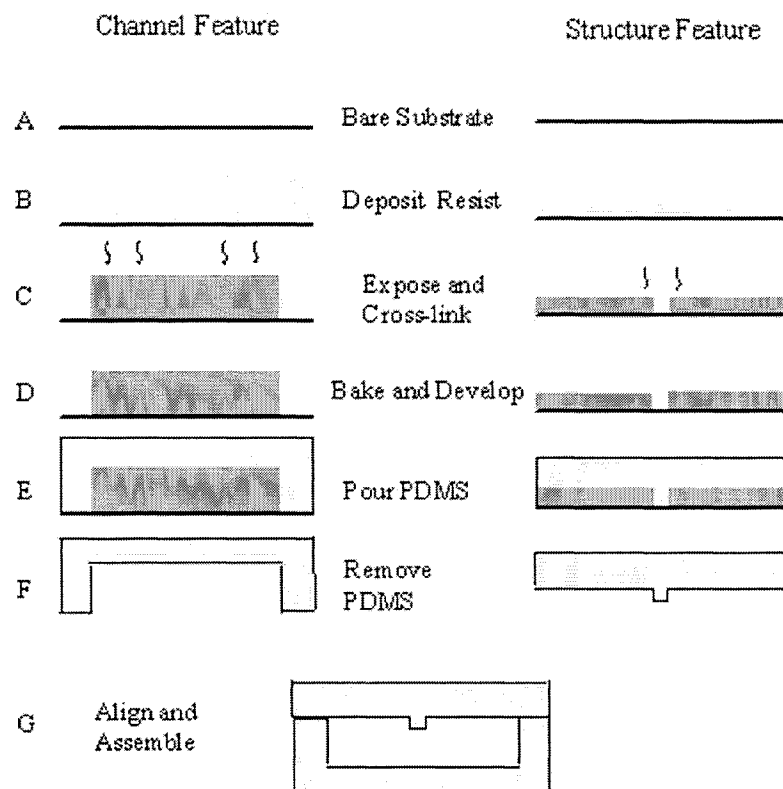


Figure 7.1 Fabrication of the microchannels with microstructure

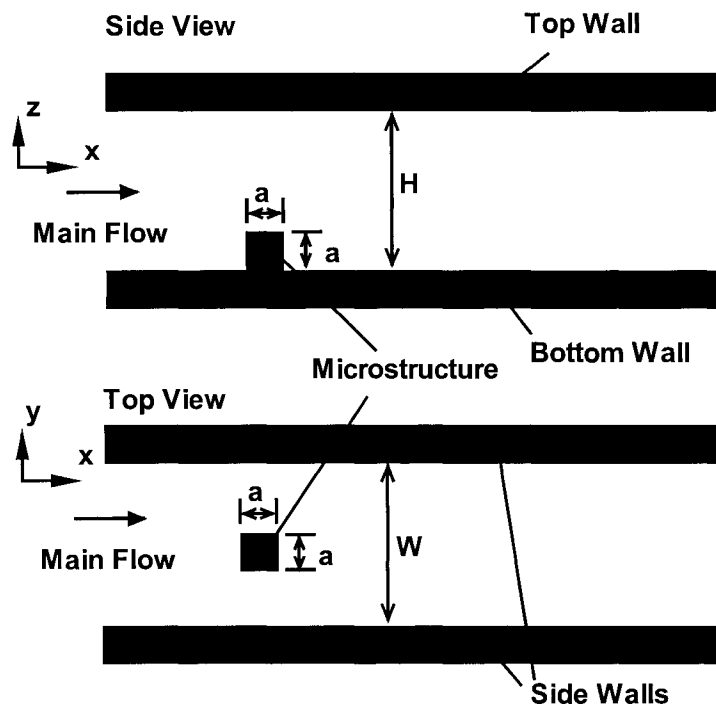


Figure 7.2 Top view and side view of the microchannel with microstructure

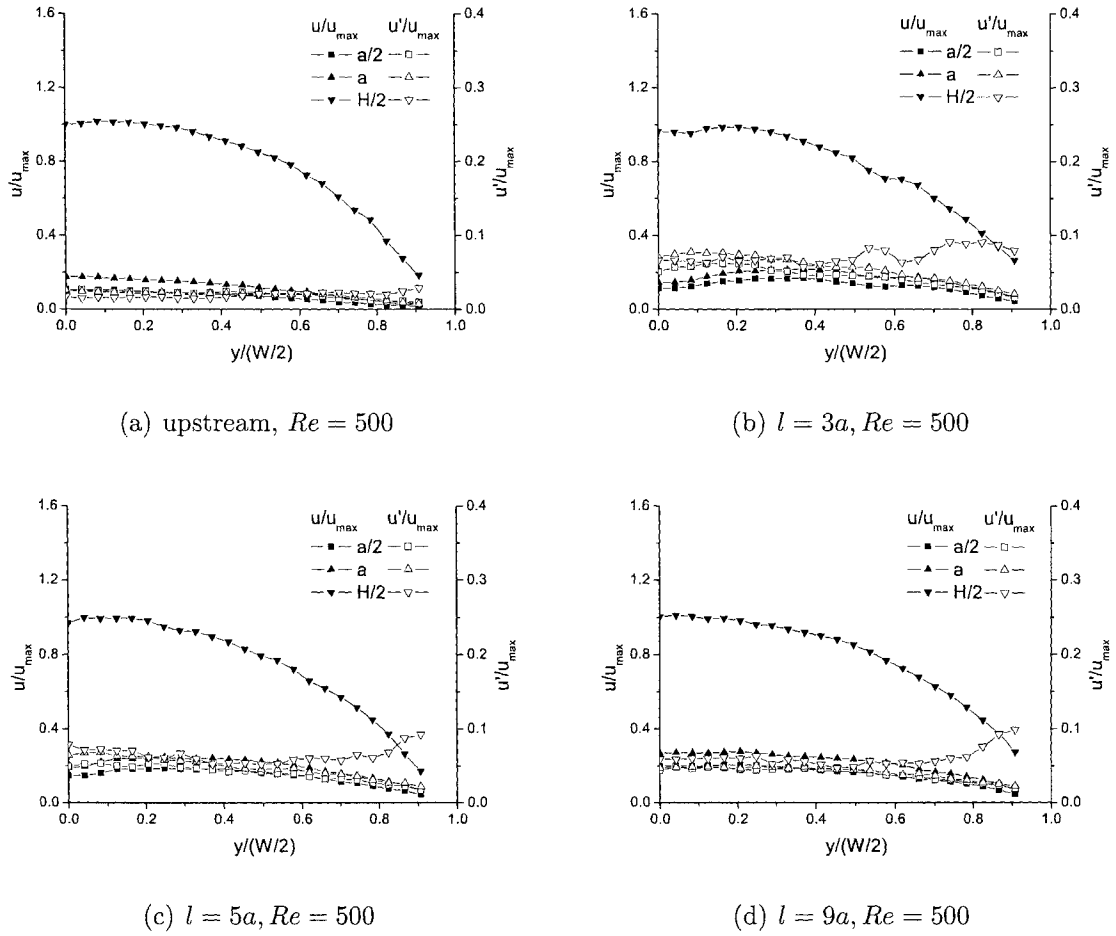


Figure 7.3 Streamwise velocity and fluctuation profiles in the microchannel containing the $20 \mu\text{m} \times 20 \mu\text{m} \times 20 \mu\text{m}$ microstructure at $Re = 500$

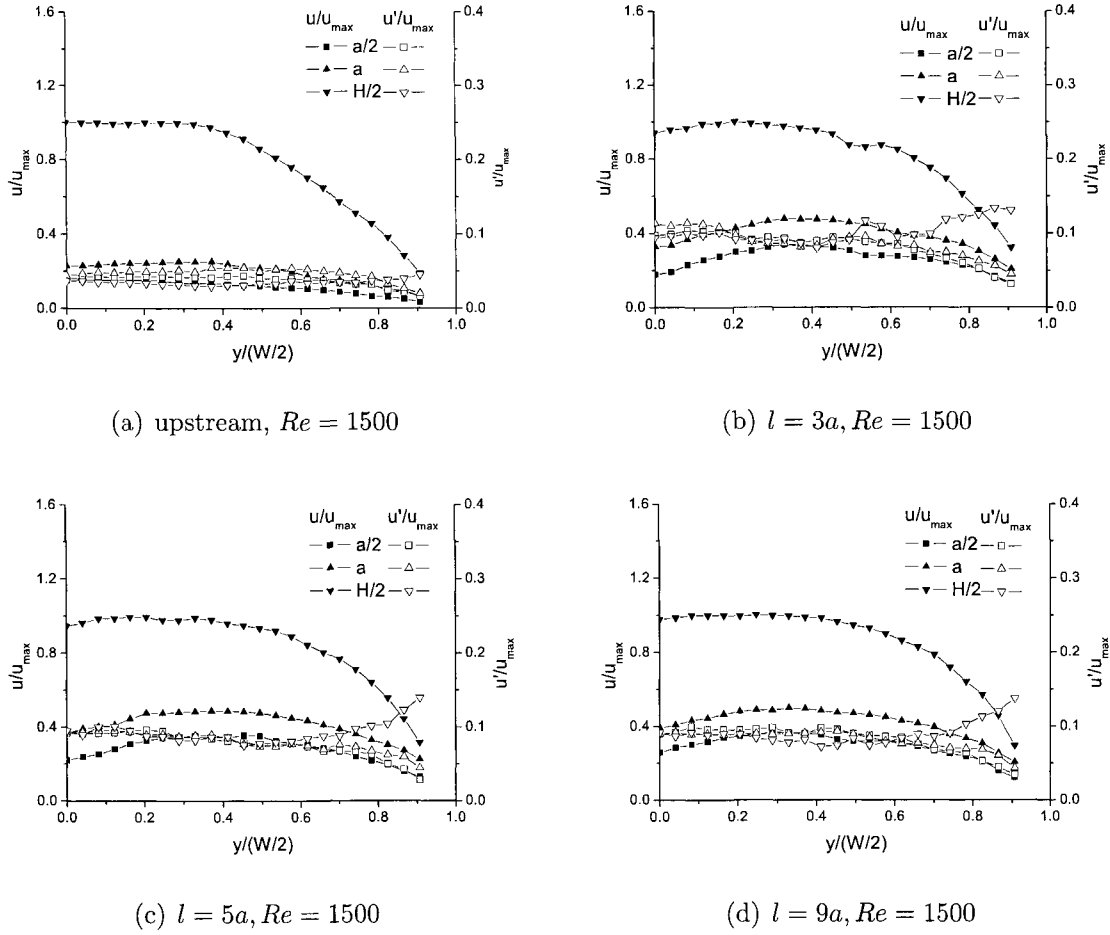


Figure 7.4 Streamwise velocity and fluctuation profiles in the microchannel containing the $20 \mu\text{m} \times 20 \mu\text{m} \times 20 \mu\text{m}$ microstructure at $Re = 1500$

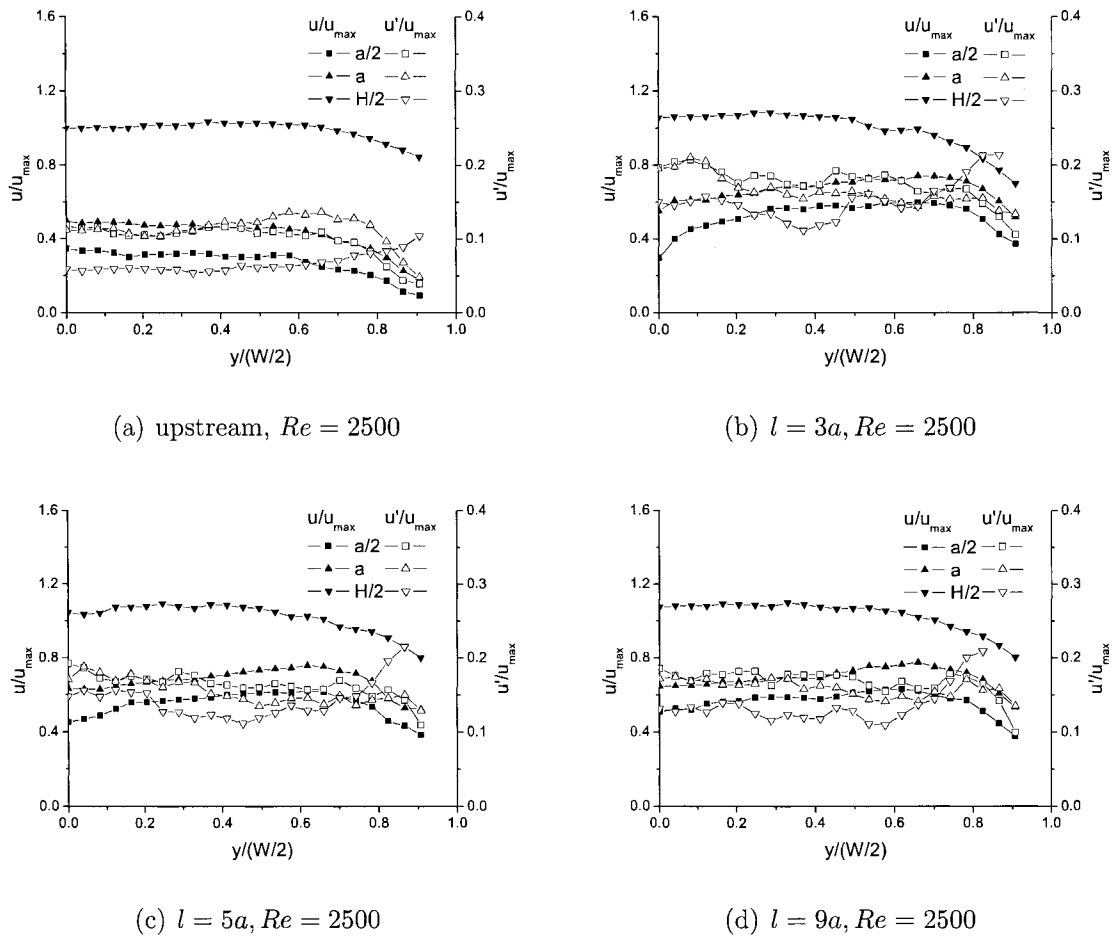


Figure 7.5 Streamwise velocity and fluctuation profiles in the microchannel containing the $20 \mu\text{m} \times 20 \mu\text{m} \times 20 \mu\text{m}$ microstructure at $Re = 2500$

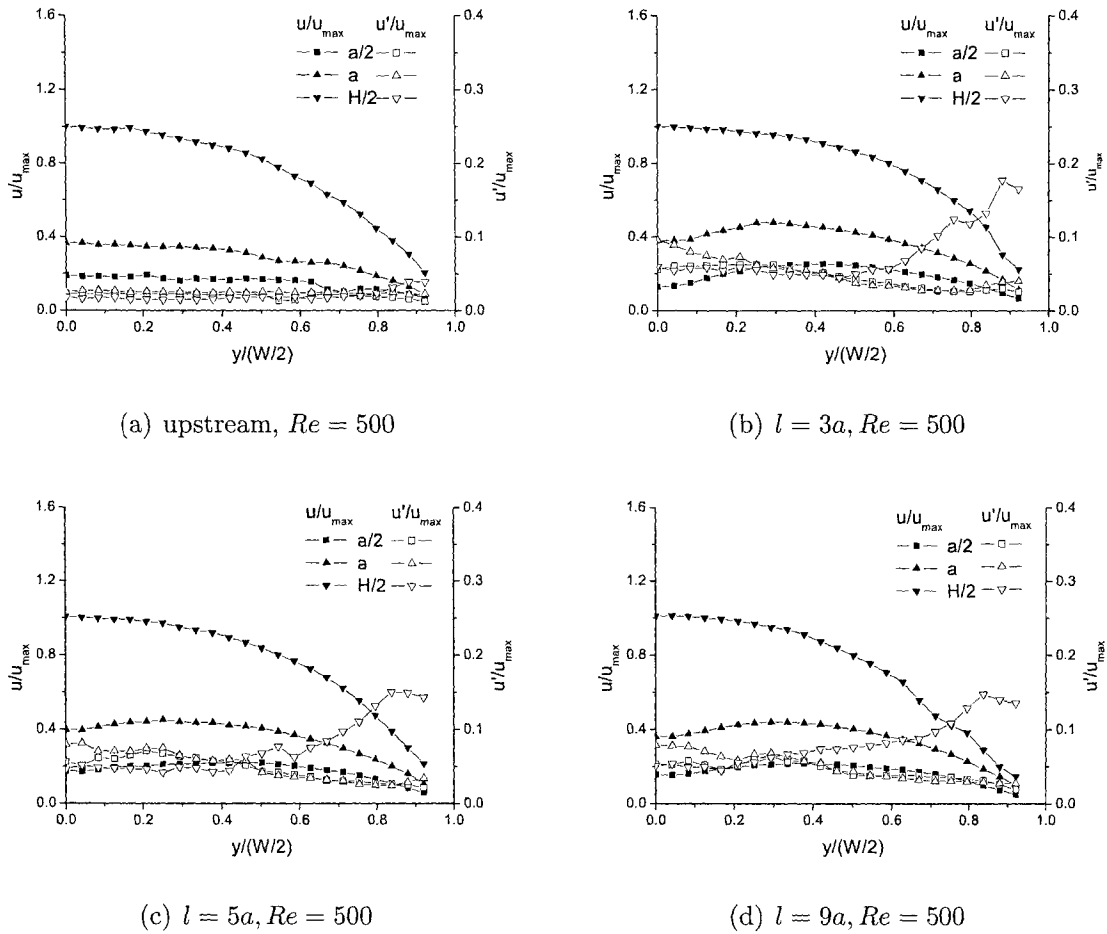


Figure 7.6 Streamwise velocity and fluctuation profiles in the microchannel containing the $40 \mu\text{m} \times 40 \mu\text{m} \times 40 \mu\text{m}$ microstructure at $Re = 500$

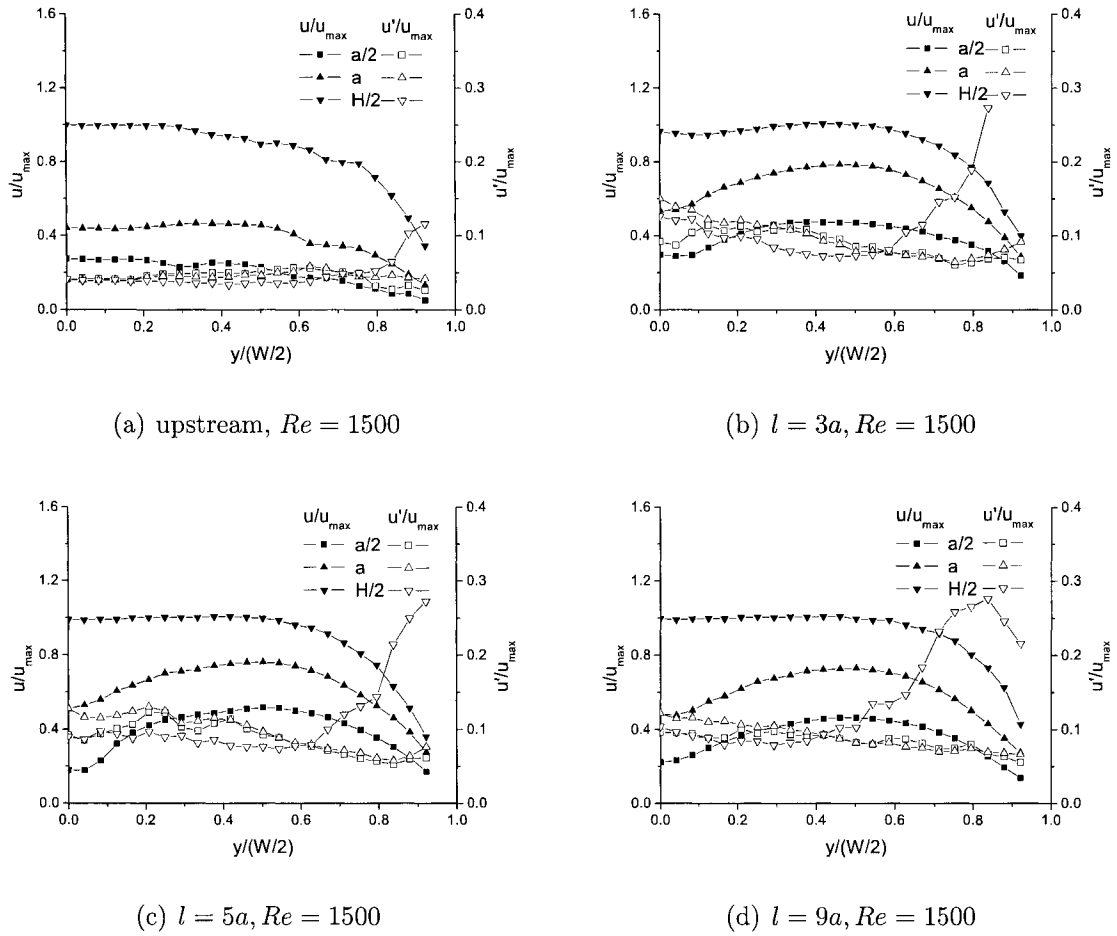


Figure 7.7 Streamwise velocity and fluctuation profiles in the microchannel containing the $40 \mu\text{m} \times 40 \mu\text{m} \times 40 \mu\text{m}$ microstructure at $Re = 1500$

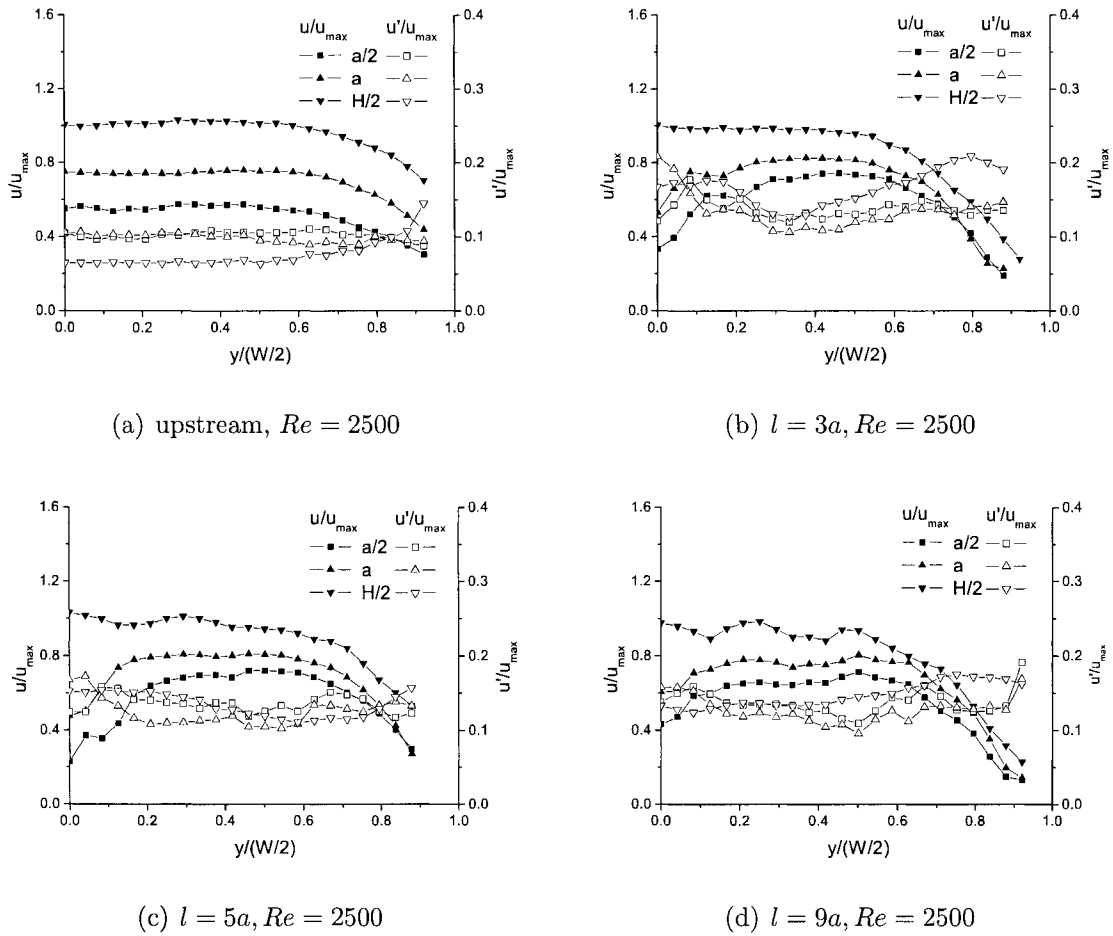


Figure 7.8 Streamwise velocity and fluctuation profiles in the microchannel containing the $40 \mu\text{m} \times 40 \mu\text{m} \times 40 \mu\text{m}$ microstructure at $Re = 2500$

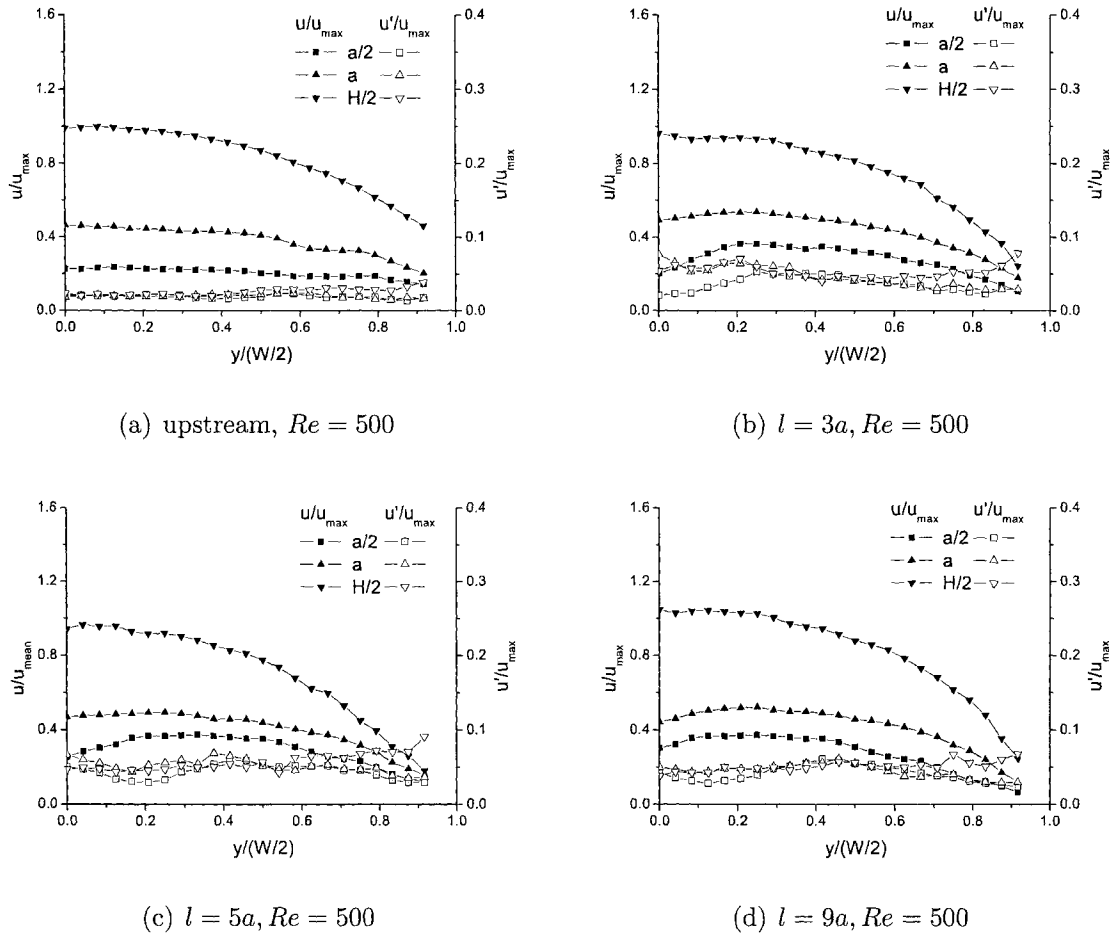


Figure 7.9 Streamwise velocity and fluctuation profiles in the microchannel containing the $50 \mu\text{m} \times 50 \mu\text{m} \times 50 \mu\text{m}$ microstructure at $Re = 500$

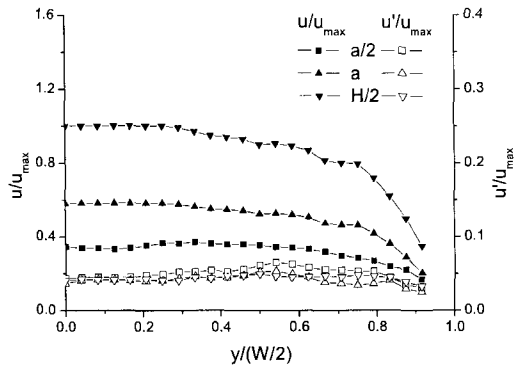
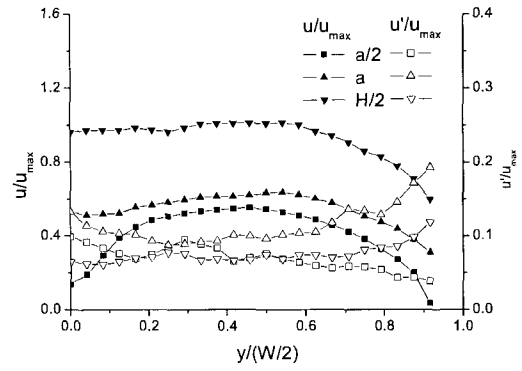
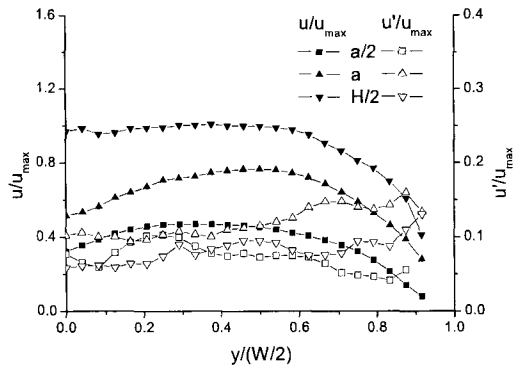
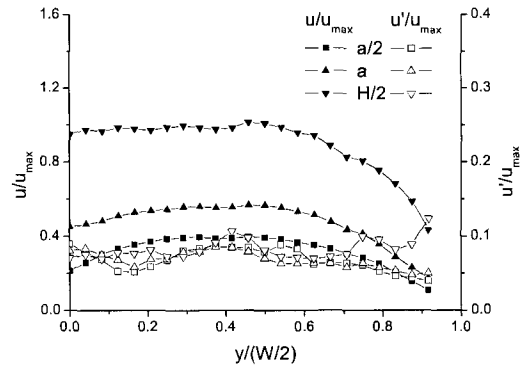
(a) upstream, $Re = 1500$ (b) $l = 3a$, $Re = 1500$ (c) $l = 5a$, $Re = 1500$ (d) $l = 9a$, $Re = 1500$

Figure 7.10 Streamwise velocity and fluctuation profiles in the microchannel containing the $50 \mu\text{m} \times 50 \mu\text{m} \times 50 \mu\text{m}$ microstructure at $Re = 1500$

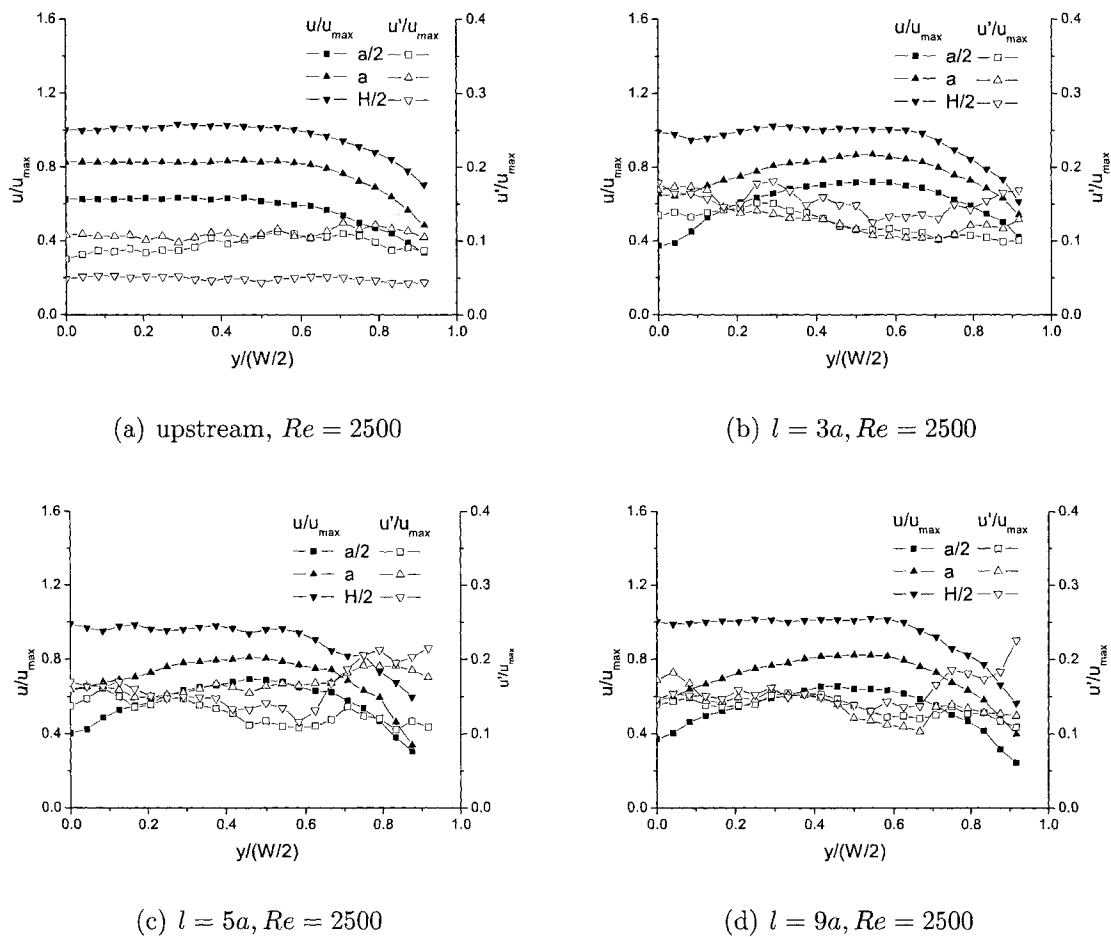


Figure 7.11 Streamwise velocity and fluctuation profiles in the microchannel containing the $50 \mu\text{m} \times 50 \mu\text{m} \times 50 \mu\text{m}$ microstructure at $Re = 2500$

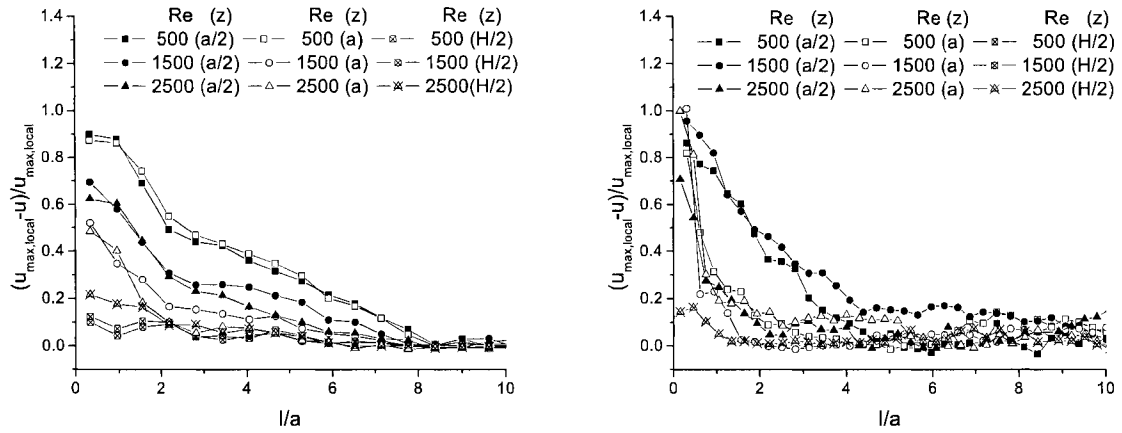
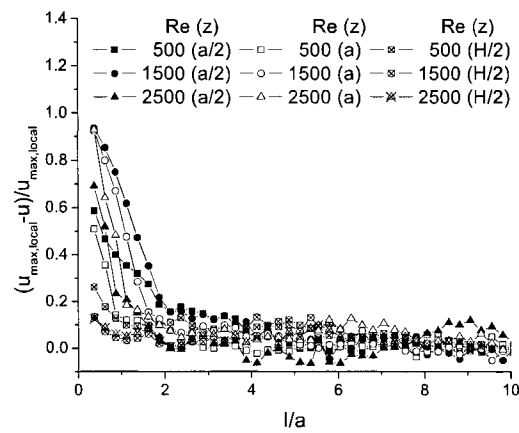
(a) 20 μm structure(b) 40 μm structure(c) 50 μm structure

Figure 7.12 Streamwise velocity deficit along the microchannel centerline for the various microstructures and Reynolds numbers

CHAPTER 8 CONCLUSIONS AND FUTURE DIRECTIONS

In this chapter, the major objectives met in this dissertation are summarized and discussed, and future directions with regard to microPIV and microfluidics are identified.

Validation of MicroPIV in the Microfluidics Research

For the *first time*, microPIV has been demonstrated to be a useful tool for investigating turbulent microscale flow with mean velocities, velocity fluctuations, Reynolds stresses, *and* large scale turbulent structures reported. MicroPIV has been applied to study the microfluidic flow in smooth and roughened microchannels. The comparison with macroscale experimental data and CFD results verified that microPIV can be used for further microfluidics research.

Hydraulic Diameter Effect in Microfluidic Flow

Microfluidic flow within square microchannels with different hydraulic diameters was studied with microPIV for Reynolds numbers ranging from 200 through 3971. The hydraulic diameter of the test microchannels ranged from 200 μm to 640 μm . The experimental data of streamwise mean velocity $\langle u \rangle$, velocity fluctuations $\langle u' \rangle$ and $\langle v' \rangle$, and Reynolds stresses $\langle u'v' \rangle$ across the microchannels widths show the onset of the fluidic flow in microchannels occurs around $Re = 1800$ when the hydraulic diameter

D_h varies from 200 μm to 640 μm , agreeing well with macroscopic results. There is no distinguishable hydraulic diameter effect in microfluidic flow within the test range of microchannels. The study on the spatial correlation coefficients R and large scale turbulent structures at high Reynolds numbers also showed microfluidic flow results to be consistent with macroscale results. The experimental data clarify the discrepancies of previous studies on the transitional Reynolds number caused by the size effect in microfluidics. Meanwhile, accompanied with the study on the aspect ratio effect, it is the *first time* to report velocity profiles, fluctuations, Reynolds shearing stresses, spatial correlations, *and* large scale turbulent structures in microfluidics.

Aspect Ratio Effect in Microfluidic Flow

Microfluidic flow within square microchannels with different aspect ratios has been studied with microPIV for Reynolds number from 200 to 3267. The aspect ratio of the tested microchannels W/H ranges from 0.97 to 5.69. The experimental data of streamwise mean velocity $\langle u \rangle$, velocity fluctuations $\langle u' \rangle$ and $\langle v' \rangle$, and Reynolds stresses $\langle u'v' \rangle$ across the microchannels widths show the onset of the fluidic flow in microchannels occurs around $Re = 1800$ when the aspect ratio varies from 0.97 μm to 5.69 μm and hydraulic diameter $D_h \approx 320 \mu\text{m}$, agreeing well with macroscale results. There is no distinguishable aspect ratio effect in microfluidic flow within the test range of microchannels. The study on the spatial correlation coefficients R and large scale turbulent structures at high Reynolds numbers also showed the consistent structure dimensions of microfluidic flow with macroscale results. These experimental data also help to clarify the discrepancies of the previous study on the transitional Reynolds number caused by the aspect ratio effect in microfluidics. Meanwhile, accompanied with the study on the hydraulic diameter effect, it is the *first time* to report velocity profiles, fluctuations, Reynolds shearing stresses, spatial correlations, *and* large scale turbulent structures in

microfluidics.

CFD Validation on Microfluidic Flow in Roughened Microchannels

Microfluidic flow within a rectangular microchannel, cross section $600\ \mu\text{m}$ (W) x $165\ \mu\text{m}$ (H) and a square microfin $120\ \mu\text{m}$ (W) x $120\ \mu\text{m}$ (L) x $43\ \mu\text{m}$ (H) at centerline of the bottom wall, has been studied with microPIV. The Reynolds number for the microfluidic flow varied from 108 to 1078. The mean velocities downstream the microfin were collected at five depths. Three-dimensional mean velocity contour slices were realized by combing the data at various depths. The comparison of the experimental data with corresponding CFD results at the wake of the microfin *primarily* showed the validation of CFD in the simulation of microfluidic flow.

Turbulence Enhancement Study on Microfluidic Flow in Roughened Microchannels

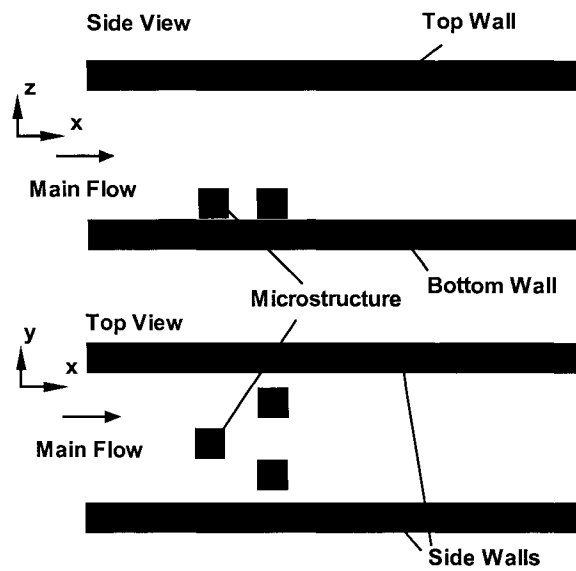
Microfluidic flow within a rectangular microchannel with cross section $600\ \mu\text{m}$ (W) x $400\ \mu\text{m}$ (H) containing single cubic microstructure of dimensions $20\ \mu\text{m}$, $40\ \mu\text{m}$, and $50\ \mu\text{m}$ was investigated. The microstructures were placed at the centerline of the bottom wall. The mean velocities were collected at three different depths with Reynolds number 500, 1500, and 2500. The turbulence enhancement effect from the microstructures were considerable by observing the variation of mean velocity profiles u and velocity fluctuations u' upstream and downstream the microstructure, and the centerline velocity deficits. The velocity fluctuations are generally greatest at depth $z = a$ and decrease with increasing downstream distance from the trailing edge of the microstructures due to viscous effects. There is no observable wake at the midplane of the test microchannels.

Larger microstructure introduces more turbulence which results in shorter wake length according to the centerline velocity deficits downstream the microstructures.

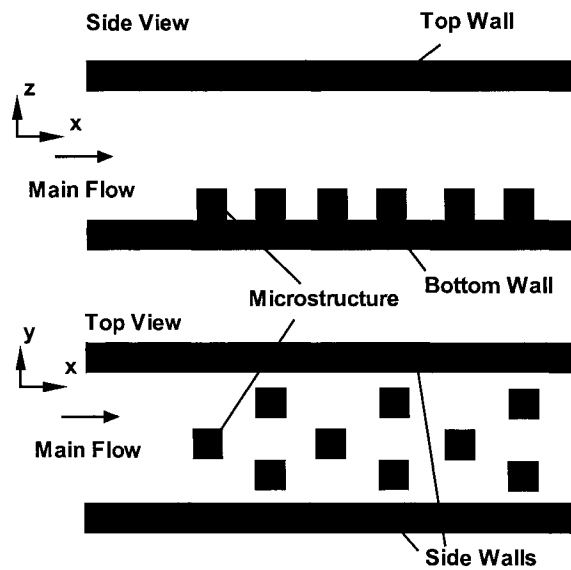
Future Directions

Since the effective optimization of geometry of microchannels with CFD requires accurate simulation of microfluidic flow fields, more comparisons between experimental data and CFD results are needed to demonstrate the accuracy in numerical models. In this dissertation, the microchannels were only roughened by one single microstructure. However, for the purposes of design and optimization of the microchannels, the man-made roughness should be distributed over the walls of microchannels periodically. Therefore, based on the current study, it is now possible to perform further studies on microchannels roughened by multiple microstructures, such as, the geometry shown in Fig. 8.1. In such a study, higher resolution is required to study the wakes downstream the microstructures. However, one must be careful in increasing particle concentration since extreme high concentration of particles mixed deionized water may become two-phase fluid which may make the pure water flow assumption in CFD models invalid.

The purposes of developing the roughened microchannels are to enhance fluid transport which, in turn, increases mixing and heat transfer coefficients. It would be interesting and challenging to perform the velocity measurement and temperature measurement simultaneously in microfluidics. Temperature measurement with fluorescent dyes in microchannels was performed and demonstrated by the author. Unfortunately, due to limited time and some practical reasons, it was not continued. It should be investigated again in the hope it can be used to measure temperature and velocity fields simultaneously within roughened microchannels.



(a) Three microstructures



(b) Multiple microstructures

Figure 8.1 Top view and side view of the roughened microchannel with multiple microstructures

BIBLIOGRAPHY

- Adams, T. M., Abdel-Khalik, S. I., Jeter, S. M., and Qureshi, Z. (1998). An experimental investigation of single-phase forced convection in microchannels. *International Journal of Heat and Mass Transfer*, 41:851–857.
- Adrian, R. J. and Yao, C. S. (1983). Pulsed laser technique application to liquid and gaseous flows and the scattering power of seed material. *Applied Optics*, 24:42–52.
- Anderson, J. R., Chiu, D. T., Jackman, R. J., Chemiavskaya, O., McDonald, J. C., Wu, H., Whitesides, S. H., and Whitesides, G. M. (2000). Fabrication of topologically complex three-dimensional microfluidic systems in pdms by rapid prototyping. *Analytical Chemistry*, 72:3158–3164.
- Aubin, J., Fletcher, D. F., and Xuereb, C. (2005). Design of micromixers using CFD modelling. *Chemical Engineering Science*, 60:2503–2516.
- Baviere, R., Ayela, F., Le Person, S., and Favre-Marinet, M. (2004). An experimental study of water flow in smooth and rough rectangular microchannels. In *Second International Conference on Microchannels and Minichannels (ICMM2004)*, pages 221–228, Rochester, New York.
- Bernard-Michel, B., Monavon, A., Abdo, D., and Simon, H. (2002). Particle velocity fluctuations and correlation lengths in dilute sedimenting suspensions. *Physics of Fluids*, 14(7):2339–2349.

- Bourdon, C. J., G., O. M., and Gorby, A. D. (2004). Validation of analytical solution of depth of correlation in microscopic particle image velocimetry. *Measurement Science and Technology*, 15:318–327.
- Celata, G. P., Cumo, M., and Zummo, G. (2004). Thermal-hydraulic characteristics of single-phase flow in capillary pipes. *Experimental Thermal and Fluid Science*, 28:87–95.
- Chen, C. S. and Kuo, W. J. (2004). Numerical study of compressible turbulent flow in microtubes. *Numerical Heat Transfer*, 45:85–99.
- Chung, P. M.-Y., Kawaji, M., and Kawahara, A. (2002). Characteristics of single-phase flow in microchannels. In *Proceedings of ASME FEDSM'02. ASME 2002 Fluids Engineering Division*, volume 257, pages 1219–1228, Montreal, Quebec, Canada.
- Clark, W. (1970). *Measurement of two-point correlations in a pipe flow using laser anemometer*. PhD dissertation, University of Virginia.
- Croce, G. and D'Agaro, P. (2005). Numerical simulation of roughness effect on microchannel heat transfer and pressure drop in laminar flow. *Journal of Physics D: Applied Physics*, 38:1518–1530.
- Devasenathipathy, S., Santiago, J. G., Wereley, S. T., Meinhart, C. D., and Takehara, K. (2003). Particle imaging techniques for microfabricated fluidic systems. *Experiments in Fluids*, 34:504–514.
- Folch, A., Ayon, A., Hurtado, O., Schmidt, M. A., and Toner, M. (1999). Molding of deep polydimethylsiloxane microstructures for microfluidics and biological applications. *Journal of Biomechanical Engineering, Transactions of the ASME*, 121(1):28–34.

- Fraser, R., Pack, C. J., and Santavicca, D. A. (1986). An ldv system for turbulence length scale measurements. *Experiments in Fluids*, 4:150–152.
- Gui, F. and Scaringe, R. P. (1995). Enhanced heat transfer in the entrance region of microchannels. In *Proceedings of the 30th Intersociety Energy Conversion Engineering Conference*, volume 2, pages 289–294.
- Guo, Z. Y. and Li, Z. X. (2003a). Size effect on microscale single-phase flow and heat transfer. *International Journal of Heat and Mass Transfer*, 46:149–159.
- Guo, Z. Y. and Li, Z. X. (2003b). Size effect on single-phase channel flow and heat transfer at microscale. *International Journal of Heat and Fluid Flow*, 24:284–298.
- Hao, P. F., He, F. H., and Zhu, K. Q. (2005). Flow characteristics in a trapezoidal silicon microchannel. *Journal of Micromechanics and Microengineering*, 15:1362–1368.
- Harms, T. M., Kazmierczak, M. J., and Gerner, F. M. (1999). Developing convective heat transfer in deep rectangular microchannels. *International Journal of Heat and Fluid Flow*, 20:149–157.
- Hegab, H. E., Bari, A., and Ameel, T. (2002). Friction and convection studies of r-134a in microchannels within the transition and turbulent flow regimes. *Experimental Heat Transfer*, 15:245–259.
- Hegab, H. E., Bari, A., and Ameel, T. A. (2001). Experimental investigation of flow and heat transfer characteristics of r-134a in microchannels. In *Microfluidics and BioMEMS. Proceedings of SPIE*, volume 4560, pages 117–125.
- Henning, A. K. (1998). Microfluidic MEMS. In *IEEE Aerospace Conference*, page 4.906, Snowmass, Colorado.
- Hetsroni, G., Mosyak, A., Pogrebnyak, E., and Yarin, L. P. (2005). Fluid flow in microchannels. *International Journal of Heat and Mass Transfer*, 48:1982–1998.

- Hopkins, R., Faghri, A., and Khrustalev, D. (1999). Flat miniature heat pipes with micro capillary grooves. *ASME Journal of Heat Transfer*, 121:102–109.
- Hu, Y., Werner, C., and Li, D. (2003). Influence of three-dimensional roughness on pressure-driven flow through microchannels. *Journal of Fluids Engineering, Transactions of the ASME*, 125(5):871–879.
- Jo, B. H., Van Lerverghe, L. M., Motsegood, K. M., and Beebe, D. J. (2000). Three-dimensional microchannel fabrication in polydimethylsiloxane (PDMS) elastomer. *Journal of Microelectromechanical Systems*, 9:76–81.
- Judy, J., Maynes, D., and Webb, B. W. (2002). Characterization of frictional pressure drop for liquid flows through microchannels. *International Journal of Heat and Mass Transfer*, 45:3477–3489.
- Keane, R. D. and Adrian, R. J. (1990). Optimization of particle image velocimeters: I. double pulsed systems. *Measurement Science and Technology*, 1:1202–1215.
- Khrustalev, D. and Faghri, A. (1999). Coupled liquid and vapor flow in miniature passages with micro grooves. *ASME Journal of Heat Transfer*, 121:729–733.
- Kim, M. J., Beskok, A., and Kihm, K. D. (2002). Electro-osmosis-driven micro-channel flows: A comparative study of microscopic particle image velocimetry measurements and numerical simulations. *Experiments in Fluids*, 33:170–180.
- Klank, H., Goranovic, G., Kutter, J. P., Gjelstrup, H., Michelsen, J., and Westergaard, C. H. (2002). PIV measurements in a microfluidic 3d-sheathing structure with three-dimensional flow behaviour. *Journal Micromechanics and Microengineering*, 12:862–869.

- Kohl, M. J., Abdel-Khalik, S., Jeter, S. M., and Sadowski, D. L. (2005). An experimental investigation of microchannel flow with internal pressure measurements. *International Journal of Heat and Mass Transfer*, 48:1518–1533.
- Koo, J. and Kleinstreuer, C. (2003). Liquid flow in microchannels: experimental observations and computational analyses of microfluidics effects. *Journal of Micromechanics and Microengineering*, 13:568–579.
- Lee, S. Y., Wereley, S. T., Gui, L., Qu, W., and Mudawar, I. (2002). Microchannel flow measurement using micro particle image velocimetry. In *American Society of Mechanical Engineers, Fluids Engineering Division (Publication) FED*, volume 258, pages 493–500.
- Li, H., Ewoldt, R., and Olsen, M. G. (2005). Turbulent and transitional velocity measurements in a rectangular microchannel using microscopic particle image velocimetry. *Experimental Thermal and Fluid Science*, 29:435–446.
- Li, H. and Olsen, M. (2005). MicroPIV measurements of turbulent flow in square microchannels with hydraulic diameters from 200 μm to 640 μm . *Internal Journal of Heat and Fluid Flow*, 26:in press.
- Li, H. and Olsen, M. (2006). Aspect ratio effects on turbulent and transitional flow in rectangular microchannels as measured by microPIV. *Journal of Fluids Engineering*, 128:in press.
- Lipman, J. (1999). Microfluidics puts big labs on small chips. *EDN Magazine*, pages 79–86.
- Mala, G. M. and Li, D. (1999). Flow characteristics of water in microtubes. *International Journal of Heat and Fluid Flow*, 20:142–148.

- Manz, A. and Becker, H. (1998). *Microsystem Technology in Chemistry and Life Sciences*. Springer, Berlin.
- Marques, C. and Kelly, K. W. (2004). Fabrication and performance of a pin fin micro heat exchanger. *Journal of Heat Transfer*, 126(3):434–444.
- McDonald, J. C., Duffy, D. C., Anderson, J. R., Chiu, D. T., H., W., Schueller, O. J. A., and Whitesides, G. M. (2000). Fabrication of microfluidic systems in poly(dimethylsiloxane). *Electrophoresis*, 21:27–40.
- Meinhart, C. D., Wereley, S. T., and Gray, M. H. B. (2000). Volume illumination for two-dimensional particle image velocimetry. *Measurement Science and Technology*, 11(6):809–814.
- Meinhart, C. D., Wereley, S. T., and Santiago, J. G. (1999). PIV measurements of a microchannel flow. *Experiments in Fluids*, 27:414–419.
- Mo, H. L., Zhou, Y. X., Zhu, T. Y., and Guo, T. W. (2004). Forced convection of low temperature nitrogen gas in rectangular channels with small aspect ratio. *Cryogenics*, 44:301–307.
- Morton, J. B. and Clark, W. H. (1971). Measurements of two-points velocity correlations in a pipe flow using laser anemometers. *Journal of Physics E: Scientific Instruments*, 4:809–814.
- Mullis, K. B., Ferre, F., and Gibbs, R. A. (1994). *The Polymerase Chain Reaction*. Birkhauser, Boston.
- Olsen, M. G. and Adrian, R. J. (2000a). Brownian motion and correlation in particle image velocimetry. *Optics & Laser Technology*, 32:621–627.

- Olsen, M. G. and Adrian, R. J. (2000b). Out-of-focus effects on particle image visibility and correlation in microscopic particle image velocimetry. *Experiments in Fluids*, 29:S166–S174.
- Papautsky, I., Gale, B. K., Mohanty, S., Ameel, T. A., and Frazier, A. B. (1999). Effects of rectangular microchannel aspect ratio on laminar friction constant. In *Proceedings of the SPIE Conference on Microfluidic Devices and Systems II*, pages 147–158, Santa Clara, CA.
- Peles, Y., Kosar, A., Mishra, C., Kuo, C. J., and Schneider, B. (2005). Forced convective heat transfer across a pin fin micro heat sink. *International Journal of Heat and Mass Transfer*, 48(17):3615–3627.
- Peng, X. F. and Peterson, G. P. (1995). The effect of thermofluid and geometrical parameters on convection of liquids through rectangular microchannels. *International Journal of Heat and Mass Transfer*, 38:755–758.
- Peng, X. F. and Peterson, G. P. (1996a). Convective heat transfer and fluid flow friction for water flow in microchannel structures. *International Journal of Heat and Mass Transfer*, 39:2599–2608.
- Peng, X. F. and Peterson, G. P. (1996b). Forced convection heat transfer of single-phase binary mixtures through microchannels. *Experimental Thermal and Fluid Science*, 12:98–104.
- Peng, X. F., Peterson, G. P., and Wang, B. X. (1994a). Frictional flow characteristics of water flowing through rectangular microchannels. *Experimental Heat Transfer*, pages 249–264.
- Peng, X. F., Peterson, G. P., and Wang, B. X. (1994b). Heat transfer characteristics of water flowing through microchannels. *Experimental Heat Transfer*, 7:265–283.

- Peng, X. F. and Wang, B. X. (1993). Forced convection and flow boiling heat transfer for liquid flowing through microchannels. *International Journal of Heat and Mass Transfer*, 37:3421–3427.
- Peng, X. F., Wang, B. X., Peterson, G. P., and Ma, H. B. (1994c). Experimental investigation of heat transfer in flat plates with rectangular microchannels. *International Journal of Heat and Mass Transfer*, 38:127–137.
- Pfund, D., Rector, D., Shekarriz, A., Popescu, A., and Welty, J. (2000). Pressure drop measurements in a microchannel. *Fluid Mechanics and Transport Phenomena*, 46(8):1496–1507.
- Prasad, A. K., Adrian, R. J., Landreth, C. C., and Offutt, P. W. (1992). Effect of resolution on the speed and accuracy of particle image velocimetry interrogation. *Experiments in Fluids*, 13:105–116.
- Qu, W., Mala, G. M., and Li, D. (2000). Pressure-driven water flows in trapezoidal silicon microchannels. *International journal of Heat and Mass Transfer*, 43:353–364.
- Qu, W. and Mudawar, I. (2002). Experimental and numerical study of pressure drop and heat transfer in a single-phase micro-channel heat sink. *International Journal of Heat and Mass Transfer*, 45:2549–2565.
- Rahman, M. M. and Gui, F. (1993). Experimental measurements of fluid flow and heat transfer in microchannel cooling passages in a chip substrate. *Advances in Electronic Packaging*, 4:685–692.
- Sabry, M. N. (2000). Scale effects on fluid flow and heat transfer in microchannels. *IEEE Transactions on Components and Packaging Technologies*, 23(3):562–567.

- Santiago, J. G., Wereley, S. T., Meinhart, C. D., Beebe, D. J., and Adrian, R. J. (1998). A particle image velocimetry system for microfluidics. *Experiments in Fluids*, 25:316–319.
- Schlichting, H. (1987). *Boundary-Layer Theory (7th edition)*. McGraw-Hill, New York.
- Shafiqul Islam, M., Haga, K., Kaminaga, M., Hino, R., and Monde, M. (2002). Experimental analysis of turbulent flow structure in a fully developed rib-roughened rectangular channel with PIV. *Experiments in Fluids*, 33:296–306.
- Sharp, K. V. and Adrian, R. J. (2004). Transition from laminar to turbulent flow in liquid filled microtubes. *Experiments in Fluids*, 36:741–747.
- Son, S. Y., Kihm, K. D., and Han, J. C. (2002). PIV flow measurements for heat transfer characterization in two-pass square channels with smooth and 90° ribbed walls. *International Journal of Heat and Mass Transfer*, 45:4809–4822.
- Stone, S. W., Meinhart, C. D., and Wereley, S. T. (2002). A microfluidic-based nanoscope. *Experiments in Fluids*, 33:613–619.
- Taylor, G. I. (1936). Correlation measurements in turbulent flow through a pipe. In *Proceedings of the Royal Society A*, volume 157, pages 537–546.
- Toh, K. C., Chen, X. Y., and Chai, J. C. (2002). Numerical computation of fluid flow and heat transfer in microchannels. *International Journal of Heat and Mass Transfer*, 45:5133–5141.
- Tracy, H. J. (1965). Turbulent flow in a three-dimensional channel. In *Journal of Hydraulics division, Proceedings of the American Society Civil Engineerings*, volume 91, pages 9–35.
- Tuckerman, D. and Pease, R. (1982). Optimized convective cooling using micromachined structure. *Journal of the Electrochemical Society*, 129:c98.

- Tuckerman, D. B. and Pease, R. F. (1981). High-performance heat sinking for VLSI. *IEEE Electron Device Letters*, 2:126–129.
- Tunc, G. and Bayazitoglu, Y. (2002). Heat transfer in rectangular microchannels. *International Journal of Heat and Mass Transfer*, 45:765–773.
- Wang, Q., Squires, K. D., and Wu, X. (1995). Lagrangian statistics in turbulent channel flow. *Atmospheric Environment*, 29:2417–2427.
- White, F. M. (1991). *Viscous Fluid Flow (2nd edition)*. McGraw-Hill, New York.
- Wu, H. Y. and Cheng, P. (2003). Friction factors in smooth trapezoidal silicon microchannels with different aspect ratios. *International Journal of Heat and Mass Transfer*, 46:2519–2525.
- Wu, P. Y. and Little, W. A. (1983). Measurement of friction factor for flow of gases in very fine channels used for micro-miniature joule-thompson refrigerators. *Cryogenics*, 23:273–277.
- Wu, P. Y. and Little, W. A. (1984). Measurement of the heat transfer characteristics of gas flow in fine channel heat exchangers used for microminiature refrigerators. *Cryogenics*, 24:415–420.
- Wyganski, I. J. and Champagne, F. H. (1973). On transition in a pipe. part 1. the origin of puffs and slugs and the flow in a turbulent slug. *Journal of Fluid Mechanics*, 59:281–335.
- Zeighami, R., Laser, D., Zhou, P., Asheghi, M., Devasenathipathy, S., Kenny, T., Santiago, J., and Goodson, K. (2000). Experimental investigation of flow transition in microchannels using micron-resolution particle image velocimetry. In *Thermomechanical Phenomena in Electronic Systems - Proceedings of the Intersociety Conference*, volume 2, pages 148–153.

ACKNOWLEDGEMENTS

I would like to take this opportunity to express my thanks to those who helped me with various aspects of conducting research and the writing of this thesis.

First and foremost, Dr. Michael G. Olsen for his guidance, patience, and support throughout this research and the writing of this thesis. His insights and words of encouragement have often inspired me and renewed my hopes for completing my graduate education.

I would also like to thank my committee members for their efforts and contributions to this work: Dr. Palaniappa Molian, Dr. Francine Battaglia, Dr. Michael Pate, and Dr. Hui Hu.

I would like to thank Nikola Pekas, Hajime Takano, David Schmidt, and other members in Dr. Marc Porter's group and Keck Lab for the help on photolithography and microfabrication.

I would like to thank Andrew Tworek, Farshid Bondar, Ian Thiele, and Dr. Francine Battaglia's CFD group for simulated fluid flow results.

I would like to thank all my labmates who build friendly environment and presented help for the completion of this work, including Kevin James, Randy Ewoldt, Janice Gustafson, John Laage, Paul Melzer, Saurabh Pande, Hua Feng, and Vishwanath Somashekar.